1-1-2015

Synthesis and Characterization of Transition Metal Based Metal Oxide and Metallic Nanocrystals for Ac Magnetic Devices and Catalysis

Hongseok Yun
University of Pennsylvania, mujinck@gmail.com

Synthesis and Characterization of Transition Metal Based Metal Oxide and Metallic Nanocrystals for Ac Magnetic Devices and Catalysis

Abstract
The d-block elements are very important in magnetics, electronics, catalysis, and biological systems. The synthesis and characterization of nearly monodisperse d-block element based nanocrystals with a precise control over the size, composition, and shape are important to utilize the nanocrystals in such applications. The goals of my thesis are to synthesize d-block transition metal based nanocrystals and understand their magnetic and catalytic properties. I present the size- and composition-dependent AC magnetic permeability of superparamagnetic iron oxide nanocrystals for radio frequency applications. The nanocrystals are synthesized through high-temperature solvothermal decomposition, and their stoichiometry is determined by Mossbauer spectroscopy. Size-dependent magnetic permeability is observed in maghemite nanocrystals, while as-synthesized, magnetite-rich, iron oxide nanocrystals do not show size dependence due to the inhomogeneous crystal structure of the as-synthesized nanocrystals. The saturation magnetization of iron oxide nanocrystals is increased by doping of non-magnetic Zn2+ into A site of ferrite, resulting the enhancement of the real part of the magnetic permeability of Zn0.25Fe2.75O4 nanocrystals by twofold compared to that of similarly sized ferrite nanocrystals. The integration of 12.3 nm Zn0.25Fe2.75O4 nanocrystals into a microfabricated toroidal inductor and a solenoid inductor yield higher quality factors than air core inductors with the same geometries. The ligand exchange with dendrimers reduces the blocking temperature of Mn0.08Zn0.33Fe2.59O4 nanocrystal, indicating the decrease of dipolar coupling between nanocrystals. The study on MnxFe3-xO4 and CoxFe3-xO4 nanocrystals shows a clear difference in DC and AC magnetic behaviors of soft and hard magnetic nanocrystals. The inductor with zinc ferrite nanocrystal core is embedded into a power converter and its temperature dependent energy efficiency is measured. The energy efficiency of a power converter with the nanocrystal core inductor rises as the temperature increases while that of the power converters with an air core inductor or commercial core inductor decreases. Finally, I describe the hydrodeoxygenation reaction of 5-hydroxymethylfurfural into 2,5-dimethylfuran by metallic nanocrystals such as Pt, PtMn, PtFe, PtCo, and PtNi. Both conversion ratio and selectivity for 2,5-dimethylfuran show clear composition dependent catalytic properties and, in particular, 3.7 nm Pt3Co2 nanocrystals achieve 98 % of selectivity for 2,5-dimethylfuran.

Degree Type
Dissertation

Degree Name
Doctor of Philosophy (PhD)

Graduate Group
Chemistry

First Advisor
Christopher B. Murray

Keywords
bimetallic nanocrystals, ferrite, hydrodeoxygenation, magnetic permeability, nanocrystals, radio frequency

Subject Categories
Chemistry | Mechanics of Materials

SYNTHESIS AND CHARACTERIZATION OF TRANSITION METAL BASED METAL OXIDE AND METALLIC NANOCRYSTALS FOR AC MAGNETIC DEVICES AND CATALYSIS

Hongseok Yun

A DISSERTATION

in

Chemistry

Presented to the Faculties of the University of Pennsylvania

in

Partial Fulfillment of the Requirements for the

Degree of Doctor of Philosophy

2015

Supervisor of Dissertation

_____

Dr. Christopher B. Murray

Richard Perry Professor of Chemistry and Materials Science and Engineering

Graduate Group Chairperson

_____

Dr. Gary A. Molander

Hirschmann-Makineni Professor of Chemistry

Dissertation Committee

Dr. Eric J. Schelter, Professor of Chemistry

Dr. Zahra Fakhraai, Professor of Chemistry

Dr. James M. Kikkawa, Professor of Physics and Astronomy

SYNTHESIS AND CHARACTERIZATION OF TRANSITION METAL BASED METAL OXIDE AND METALLIC NANOCRYSTALS FOR AC MAGNETIC DEVICES AND CATALYSIS

To my family

ACKNOWLEDGMENT

This work would never be completed without the great support from many people I have interacted with inside and outside the lab. First of all, I'd like to thank Prof. Christopher B. Murray, my research advisor. Chris gave so many advices and feedback on my research. Chris guided me toward a direction in which my research can develop into more interesting and valuable scientific results. Chris taught me how to solve problems through scientific approaches with various experimental tools. Under five years of his guidance, now I have developed my own way to think and understand scientific questions. Also, Chris is a great leader who motivates students so well by giving the big picture of their research, which makes clear how our work will contribute to the world outside the lab. In addition, I really appreciate that Chris has been trying to build our group having a family like atmosphere where people feel comfortable to work and discuss with others, resulting more collaborative lab environment. During my Ph.D. study, I have been always amazed by his creative thinking and ideas in research and really appreciate the opportunity that I could work with Chris. Secondly, I'd want to thank Prof. James M. Kikkawa, who gave me many advices on my research, especially on the magnetic property measurement technique and analysis. Without his comments, my work in AC magnetic property measurements of nanocrystals would not be accomplished in depth. Finally, I appreciate all the help from my committee members, Prof. Eric J. Schelter and Prof. Zahra Fakhraai. Their comments on my research progress in every committee meeting were so valuable and made me to move forward to complete this thesis. I also want to thank Prof. Georgia C. Papaefthymiou at Villanova University. She helped me to understand the composition change of iron oxide nanocrystals over time and her Mössbauer measurements and analysis improved the quality of my study a lot.

I am really grateful to all my labmates in the Murray group. I enjoyed my Ph.D. study because of my great labmates who are so motivated and full with creative ideas. Also, I learned a lot from the diligence of all the group members. I want to give my special thanks to Taejong Paik, who

guided me in every aspect of research. He taught me all the basics about nanocrystals as a senior Ph.D. student when I just joined the lab and I really appreciate it. He is also a great collaborator and helped my project with x-ray characterization of nanocrystals. Secondly, I want to thank Jungkwun Kim, who I have collaborated with for AC magnetic applications. I believe his help on the inductor fabrication with magnetic nanocrystals upgraded our lab capability in AC magnetics. Thirdly, I would like to thank Prof. Raymond J. Gorte and Jing Luo, who contributed the measurements of the catalytic activity of bimetallic nanocrystals for hydrodeoxygenation. The work in catalysis would not be possible without their help. Finally, I want to thank Jennifer D. Lee, who contributed to the synthesis of some of bimetallic nanocrystals. Even though we have not worked together for a long time, her work in the synthesis helped me a lot in terms of understanding the HDO activity of platinum based bimetallic nanocrystals with various compositions. I will look forward to see her work in the future.

Personally, I want to thank Jinsoo Han, who was my roommate for two years. Since he came to Penn about three years ago, we have spent much time enjoying conversations covering so many topics including science, economics, politics, sports, and etc. It was really lucky to have such a great friend like him and I wish him the best of luck in his Ph.D. study. I also want to thank all the people in UPenn Hanwoori, whom I played tennis with. I could relieve my stress by playing sports and meeting many great friends in the group. I'll miss all of them so much. Last but not least, I want to give my deepest gratitude to my parents and my brother. For the last five years, their support for me was incredible in all aspects. I inherited and learned from my parents how to maintain a positive attitude even when I'm facing difficult situations and it drove me here to complete my Ph.D. study. I want to say that what they've taught me through my whole life are the most valuable lessons that I've got. I cannot imagine how I would finish my study without the support from my family and I want to say that I love them so much.

Thank you

ABSTRACT

SYNTHESIS AND CHARACTERIZATION OF TRANSITION METAL BASED METAL OXIDE AND METALLIC NANOCRYSTALS FOR AC MAGNETIC DEVICES AND CATALYSIS

Hongseok Yun

Dr. Christopher B. Murray

The d-block elements are very important in magnetics, electronics, catalysis, and biological systems. The synthesis and characterization of nearly monodisperse d-block element based nanocrystals with a precise control over the size, composition, and shape are important to utilize the nanocrystals in such applications. The goals of my thesis are to synthesize d-block transition metal based nanocrystals and understand their magnetic and catalytic properties. I present the size- and composition-dependent AC magnetic permeability of superparamagnetic iron oxide nanocrystals for radio frequency applications. The nanocrystals are synthesized through high-temperature solvothermal decomposition, and their stoichiometry is determined by Mössbauer spectroscopy. Size-dependent magnetic permeability is observed in maghemite nanocrystals, while as-synthesized, magnetite-rich, iron oxide nanocrystals do not show size dependence due to the inhomogeneous crystal structure of the as-synthesized nanocrystals. The saturation magnetization of iron oxide nanocrystals is increased by doping of non-magnetic Zn^{2+} into A site of ferrite, resulting the enhancement of the real part of the magnetic permeability of $Zn_{0.25}Fe_{2.75}O_4$ nanocrystals by twofold compared to that of similarly sized ferrite nanocrystals. The integration of 12.3 nm $Zn_{0.25}Fe_{2.75}O_4$ nanocrystals into a microfabricated toroidal inductor and a solenoid inductor yield higher quality factors than air core inductors with the same geometries. The ligand exchange with dendrimers reduces the blocking temperature of $Mn_{0.08}Zn_{0.33}Fe_{2.59}O_4$ nanocrystal, indicating the decrease of dipolar coupling between nanocrystals. The study on $Mn_xFe_{3-x}O_4$ and

$Co_xFe_{3-x}O_4$ nanocrystals shows a clear difference in DC and AC magnetic behaviors of soft and hard magnetic nanocrystals. The inductor with zinc ferrite nanocrystal core is embedded into a power converter and its temperature dependent energy efficiency is measured. The energy efficiency of a power converter with the nanocrystal core inductor rises as the temperature increases while that of the power converters with an air core inductor or commercial core inductor decreases. Finally, I describe the hydrodeoxygenation reaction of 5-hydroxymethylfurfural into 2,5-dimethylfuran by metallic nanocrystals such as Pt, PtMn, PtFe, PtCo, and PtNi. Both conversion ratio and selectivity for 2,5-dimethylfuran show clear composition dependent catalytic properties and, in particular, 3.7 nm Pt_3Co_2 nanocrystals achieve 98 % of selectivity for 2,5-dimethylfuran.

TABLE OF CONTENTS

LIST OF TABLES

LIST OF ILLUSTRATIONS

CHAPTER 1. Introduction

1.1 Transition Metal Based Nanocrystals

The d-block elements are very important in magnetics, electronics, catalysis, and biological systems. The d-block elements have partially filled d orbitals, except copper and zinc, which is responsible for their magnetic and catalytic properties. For example, depending on the number of electrons in d orbitals and surrounding environments (e.g. ligands), some of the transition metal cations possess unpaired electrons. The unpaired electrons lead to unquenched magnetic dipole moments from the cations. As a result, these transition metal cations possess net magnetic moments and the number of unpaired electrons determines the magnetic moments of the cations.

In terms of the catalytic activity, the number of electrons in the d orbitals and the surrounding environments determine the electronic structure of d-block elements. Different electronic structures change the binding energy between a metal atom and a reactant, leading to the various catalytic behaviors of different metals. For example, iron is a well-known heterogeneous catalyst for the synthesis of ammonia from nitrogen and hydrogen, which is known as the “Haber Process”, and nickel has been used to catalyze the hydrogenation of carbon double/triple bonds. Choosing the appropriate d-block elements is crucial to optimizing the catalytic activity for a given reaction.

The transition metal based nanocrystals (NCs) are promising materials for many applications including as magnetics,[1–3] catalysts,[4–7] electronics,[8–10] and biological applications.[11–14] Among these applications, magnetic technology and catalysis are the focus of this thesis. In this work, metal oxide NCs, specifically; iron oxide, zinc ferrite, and manganese zinc ferrite, and metallic NCs including Pt, PtMn, PtFe, PtCo, and PtNi are synthesized for these two purposes.

1.2 Synthesis of Metal Oxide NCs

Electrical, optical, and catalytic properties of NCs are also strongly correlated with their composition, size, and shape. For example, ferromagnetic/ferrimagnetic NCs start showing a peculiar property called "superparamagnetism"[15] when the size becomes less than a certain value depending on the type of materials (e.g. 30 nm for Fe_2O_3 and 25 nm for Fe_3O_4).[16] These correlations emphasize the importance of the synthesis of nearly monodisperse colloidal NCs with precisely controlled size, shape, composition, and crystallographic structures. In order to synthesize colloidal metal oxide NCs, many synthetic techniques, including solvothermal reactions,[3] sol-gel reactions,[17] and inverse micelle methods[18] have been developed. Among the methods, the solvothermal synthesis offers the best control over the size, shape, and crystallinity of the NCs. For example, Hyeon *et al.* developed the synthesis of metal oxide NCs with a "heat-up method."[3,19] The heat-up method mixes metal

precursors such as metal-oleate, metal-acetate, and metal-acetylacetonate with surfactants and high boiling point solvents before elevating the temperature of the reaction mixture. The nucleation and growth processes can be controlled by manipulating the kinetics of the metal precursor decomposition. At a certain temperature during the elevation of temperature (e.g. 186°C for iron acetylacetonate)[20], the metal precursors start decomposing and forming nuclei. This lowers the metal precursor concentration and leads to the growth on the nuclei formed initially. Therefore, controlling the heating rate or reaction temperature can engineer the size and monodispersity of NCs. By increasing the metal precursor concentration, the size of iron oxide NCs can be increased smoothly from 10 nm to 20 nm (Figure 1.1). The small angle x-ray scattering (SAXS) data (Figure 1.1g) support the great monodispersity of these iron oxide NCs. The heat-up method has been widely used in the synthesis of transition metal oxides,[3,19,21,22]metallic NCs,[5,23,24]and rare earth based NCs.[25]

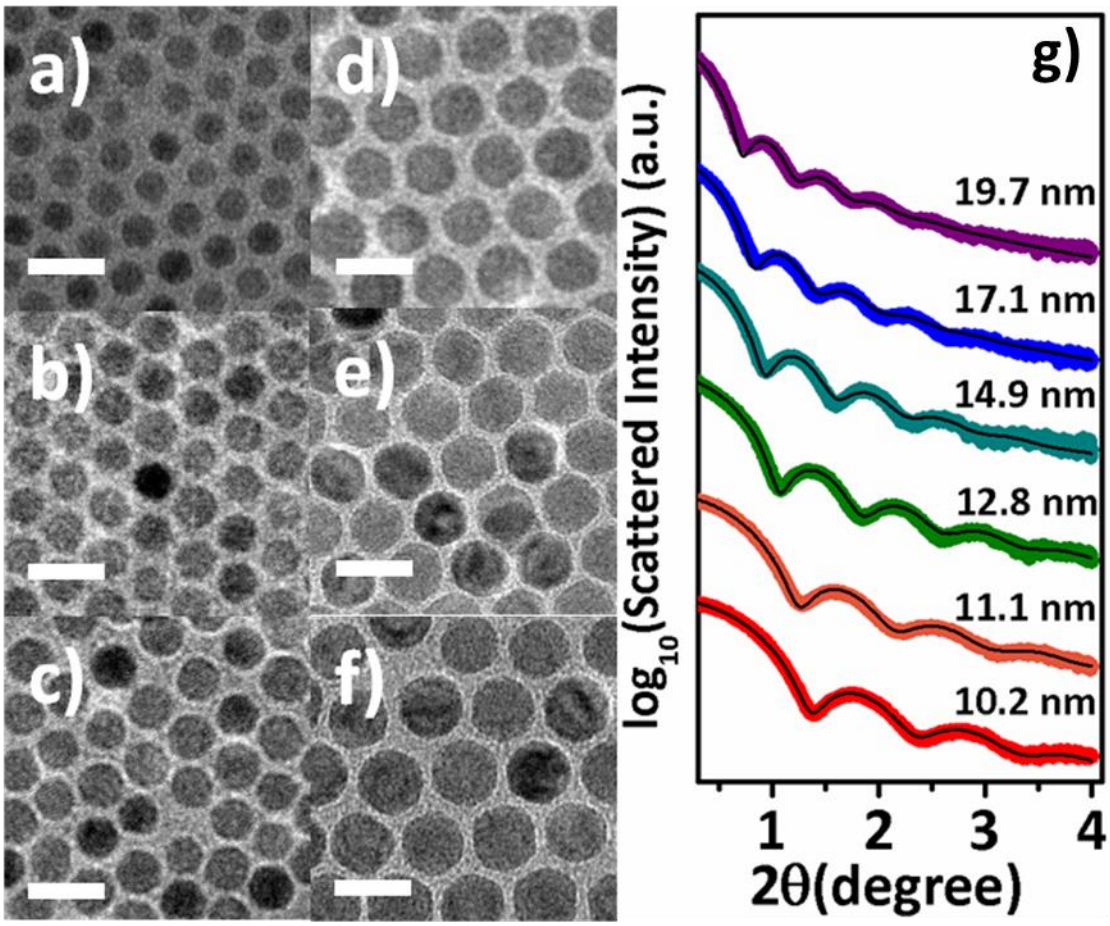

Figure 1.1. TEM images of a) 10.2 nm, b) 11.1 nm, c) 12.8 nm, d) 14.9 nm, e) 17.1 nm, and f) 19.7 nm iron oxide NCs. g) SAXS data of iron oxide NCs.(Adopted from the reference 26)

The metal oxide NCs studied in this work possess spinel crystal structures (space group $Fd\bar{3}m$, No. 227, Figure 1.2[27]). Spinel NCs including magnetite (Fe_3O_4), maghemite (γ-Fe_2O_3), zinc ferrite ($Zn_xFe_{3-x}O_4$), cobalt ferrite ($Co_xFe_{3-x}O_4$), and manganese ferrite ($Mn_xFe_{3-x}O_4$) belong to this class of structures. In the spinel structure, oxygen anions (O^{2-}) are arranged in a cubic close-packed

structure. Between the anions, there are tetrahedral (T_d) interstitial sites and octahedral (O_h) interstitial sites which are called A sites and B sites, respectively. As there is one A site and two B sites per four O^{2-}, the materials in the spinel group can be written as AB_2O_4. Cations have different preferences to either site. For example, Fe^{2+} only occupies B sites in the structure, whereas Fe^{3+} is distributed equally over A and B sites. When cations in +2 oxidation states take over B sites the material is called “inverse spinel” structure.[27] This is the case for materials like magnetite. In the case of $ZnFe_2O_4$, Zn^{2+} prefers to position itself in an A site; this is called “normal spinel” structure.

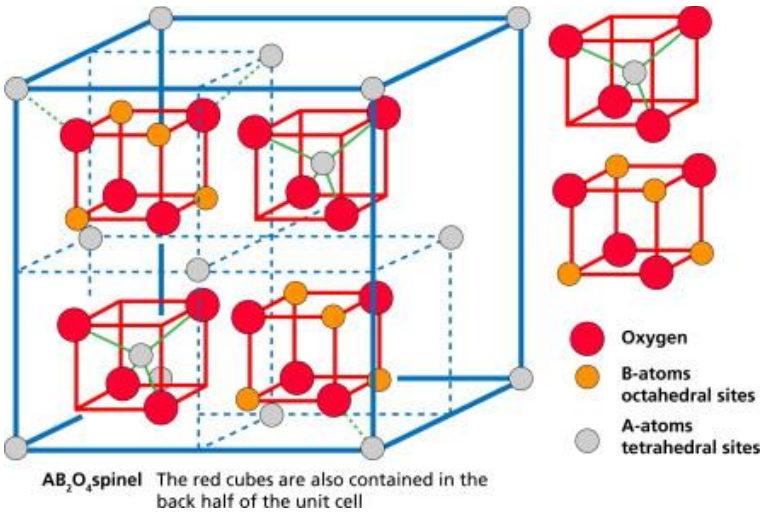

Figure 1.2. A cartoon depicting the AB_2O_4 spinel crystal structure (Adapted from reference 27)

The spinel ferrite materials have magnetic moments. Since the spins located on A sites and B sites align antiparallel to each other due to the superexchange

coupling with adjacent O^{2-}, the magnetic moment of spinel ferrites originates from the moment difference between A sites and B sites.[28] Therefore, the total magnetic moment, M_{tot}, should be equal to $2M_B$-M_A as there are two B sites per one A site. It can be inferred that the magnitude of total magnetization can be controlled by changing the cations in A sites and B sites.

1.3 Synthesis of Metallic NCs

To prepare single component metallic NCs, the “heat-up” method is often employed. For example, to prepare d^8 transition metal NCs such as Ni, Pd, and Pt, metal acetylacetonate dissolved in benzyl ether is decomposed at high temperature in the presence of oleylamine and trioctylphosphine.[29] By increasing the amount of organometallic precursors, the size is readily controlled. (Figure 1.3) The control NC size is important in the applications of magnetics and catalysis. It has been reported that the saturation magnetization (M_s) increases as the size of zinc ferrite NCs increases.[30] In addition, the control of NC size eventually affects the number of metal-support interfacial sites and changes their CO oxidation rates.[29] These observations indicate the capabilities of solvothermal reaction methods in controlling/optimizing material properties.

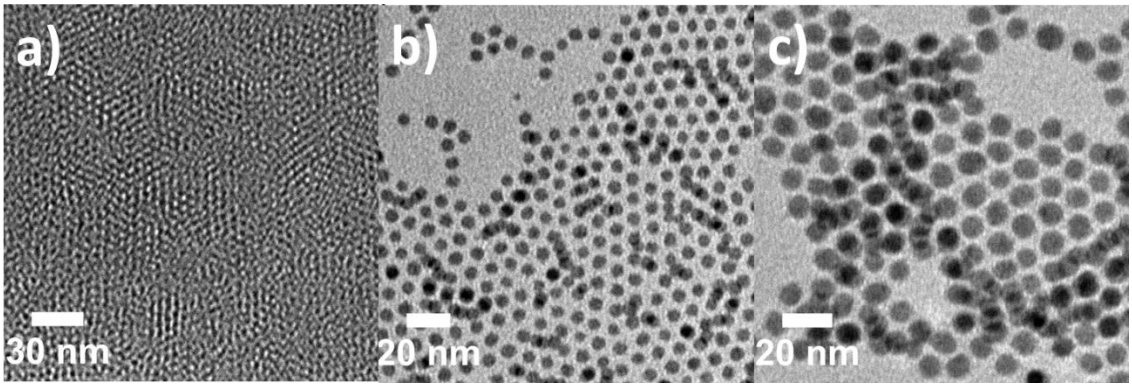

Figure 1.3. The TEM images of a) 3.2 nm (±10.2 %), b) 6.0 nm (±9.3 %), and c) 9.4 nm (±7.8 %) Ni NCs.

For the synthesis of bimetallic NCs, a “hot-injection method” is often used.[1,2,31] In this method, the oversaturated organometallic precursor solution is injected into a high boiling point solvent at an elevated temperature. Upon injection, homogenous nanocrystalline nuclei are formed in the solution resulting reduced the metal precursor concentration in the reaction mixture. Once the metal monomer concentration becomes less than the nucleation threshold, the growth process dominates the reaction and prevents further nucleation processes. The key to the formation of NCs with uniform size and shape is to efficiently separate the nucleation and growth processes. Further growth can lead to Oswald ripening. This process is well summarized in the Figure 1.4.[32]

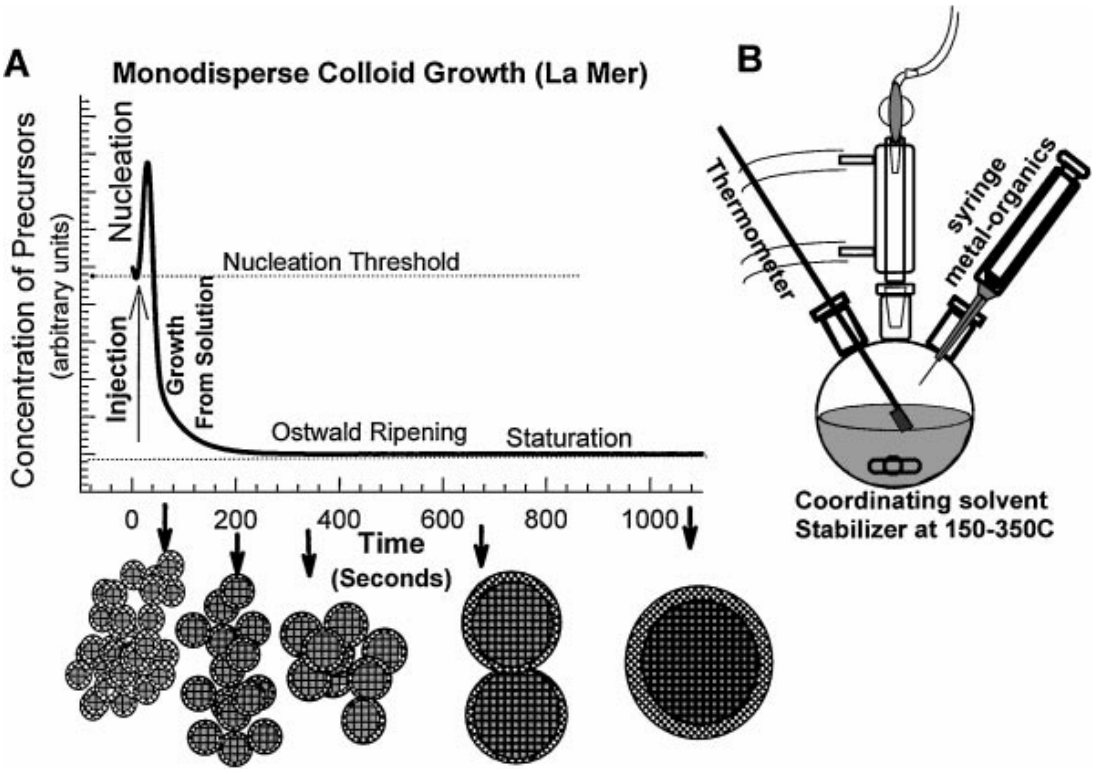

Figure 1.4. (A) Diagram explaining the mechanism of nucleation and growth process of NCs by hot-injection method. (B) A diagram showing the general setup for the hot-injection method. (Adapted from reference 32)

With this method, bimetallic NCs such as PtFe and PtCo can be prepared. (Figure 1.5) In the synthesis for these NCs, metal carbonyl precursors are injected into a reaction mixture consisting of platinum precursor, surfactants, and a solvent. The reactions can result in spheres (Figure 1.5a, c) or cubes (Figure 1.5b) by controlling the nucleation and growth processes. The ratio between Pt and other transition metals can be varied by controlling the precursor ratios.[1,5] These bimetallic NCs are promising replacements for commercial Pt catalyst.[33–35]

Since platinum is one of the most expensive metals, many efforts have focused on reducing the amount of Pt used[36] or even to improve the catalytic efficiencies.[30] For example, Schüth *et al.* reported that the use of Pt_3Co nanoparticles in hollow carbon nanospheres can yield 98% of the selectivity for 2,5-dimethylfuran (DMF) from 5-hydroxymethylfurfural (HMF) whereas that of Pt nanoparticles in the same geometry gives only 1% of selectivity for DMF.

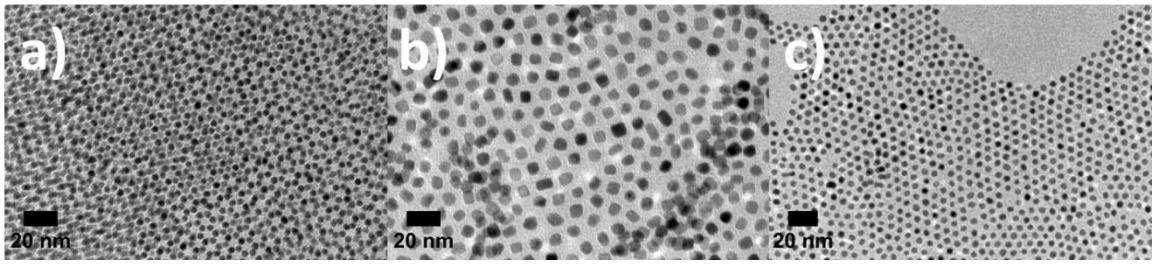

Figure 1.5. TEM images of a) spherical FePt NCs, b) cubic FePt NCs, and c) spherical $CoPt_3$ NCs.

The development of the chemical synthesis of colloidal NCs has brought new opportunities in the research of magnetic materials and catalysts. In order to understand the magnetic and catalytic properties of NCs, it is essential to prepare nearly monodisperse NCs with uniform shape as their properties are strongly correlated to their size,[19,26,29,31,37] shapes,[30,38] and crystallographic structure.[39,40] This work will discuss the synthesis, morphology, and crystal structure analyses of NCs and further characterization of magnetic or catalytic properties.

1.4. Magnetism

When an external magnetic field (*H*) is applied to a material, the field induces the material to have an internal magnetic moment (*B*). In SI unit, the relationship between *H* and *B* is defined by equation (1.1).

$$B = \mu_0(H + M) = \mu H \tag{1.1}$$

Where *B* is the induced magnetic flux (Φ) per unit area (*A*) inside of a material, μ_0 is the magnetic permeability of free space, *H* is the strength of the external magnetic field, *M* is the magnetization of the material, and μ is the magnetic permeability of the material.[41] The magnetic permeability represents how much the external magnetic flux can be concentrated inside of a material. And the equation (1.1) can be rewritten as equation (1.2).

$$H + M = \frac{\mu}{\mu_0} H = \mu_r H \tag{1.2}$$

Where μ_r is the relative magnetic permeability. Therefore, equation (1.3) can be written by combining the equation (1.1) and (1.2) as follows.

$$B = \mu_0(H + M) = \mu_0 \mu_r H \tag{1.3}$$

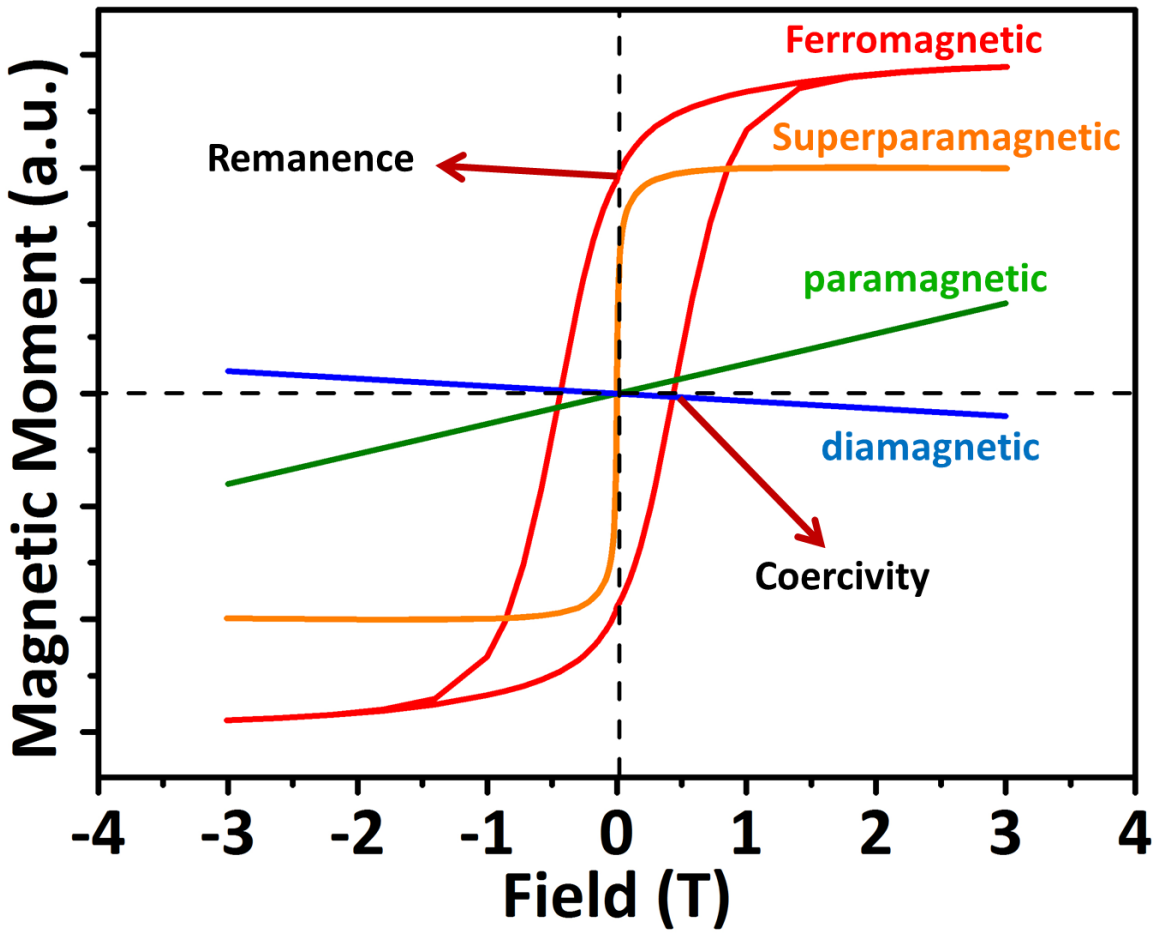

Figure 1.6. The B-H curves of ferromagnetic (red), superparamagnetic (orange), paramagnetic (green), and diamagnetic (blue) materials.

The B-H curves of various types of magnetic materials are summarized in Figure 1.6. μ_r varies significantly depending on which type of magnetism the material possesses. In a free space or vacuum space, μ_r is equal to 1, which makes $B = \mu_0 H$. Diamagnetic materials possess less magnetic flux internally than externally, which means induced magnetic field, B, is less than the field outside,

H.[41] In turn, according to equation (1.3), the relative magnetic permeability of diamagnetic materials is less than 1. Paramagnetic or antiferromagnetic materials have small magnetic permeabilities (higher than vacuum permeability but close to 1). As the magnetic spins in a paramagnetic material is disordered, the magnetization is zero without an external magnetic field. In the case of antiferromagnetic materials, the magnetic spins are ordered, but they are anti-parallel to each other, resulting in no net moment. Therefore, both types of materials show low magnetic permeability. Ferromagnetic materials and ferrimagnetic materials have high magnetic permeabilities which vary from 10 to 10000. The spins in ferromagnetic materials are aligned toward each other. Even though the spins in ferrimagnetic materials are ordered in an anti-parallel direction, the number of spins in one direction is more than the ones in the opposite direction, so that there is a net magnetic moment in the materials. These two types of magnetic materials often possess a net magnetic moment even without an external magnetic field. The magnetic moment in the absence of an external magnetic field is called remanent magnetization (M_r) and the field required to make M_r to zero is called coercivity (H_c). If the H_c or magnetic anisotropy energy of a material is high, the material is called a “hard” magnet. If the opposite is true, the material is called a “soft” magnet. The general spin orientation behaviors of each type of magnetic materials are presented in Figure 1.7.

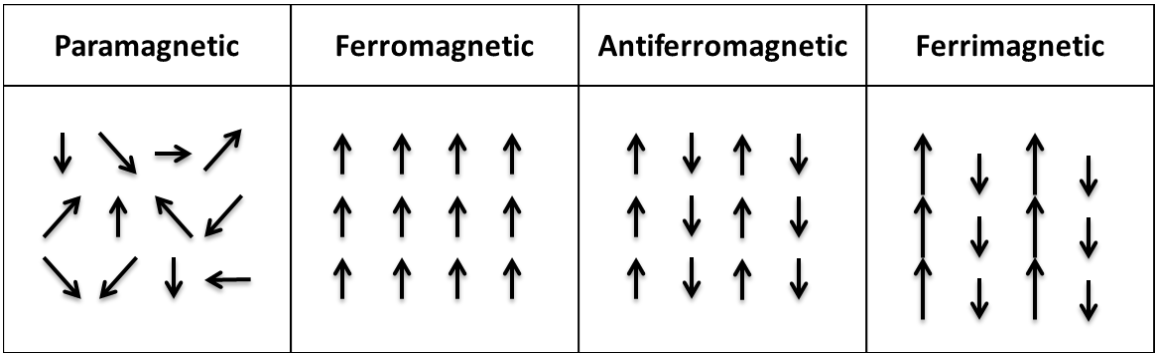

Figure 1.7. A diagram demonstrating the spin orientations of paramagnetic, ferromagnetic, antiferromagnetic, and ferrimagnetic materials.(Adapted from 41)

1.5. Superparamagnetic NCs

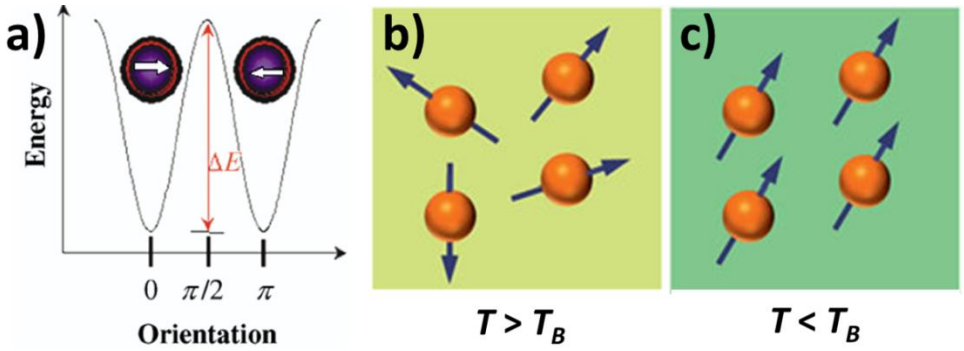

Figure 1.8. a) A diagram of the energy dependent NC magnetization. DE indicates the energy barrier to the rotation of the magnetization. The magnetization directions of NCs b) at under T_B and c) at above T_B. (Adapted from reference 16 and 37)

If the domain size of a magnetic material becomes as small as 1 – 20 nm, a new phenomenon emerges, which is called superparamagnetism.[15] Superparamagnetic behavior is expressed in single domain magnetic NCs due to thermally induced magnetic reorientation above the blocking temperature (T_B). The NCs have thermally induced magnetic relaxation comparable to the magnetization reversal energy barrier (ΔE in Figure 1.8a). The Néel relaxation time of superparamagnetic NCs is expressed in the Néel-Arrhenius equation, $\tau_N = \tau_0 \exp(E_a/k_B T)$, where the physical parameters of NCs are defined as follows: $1/\tau_0$ is attempt frequency for magnetization reversal, E_a is the anisotropy barrier for the particle which, in the absence of interparticle interactions, is taken to be KV where K is the magnetic anisotropy energy density and V is the volume of the NC.[15] Thermally assisted magnetization reversals can take place and the NCs exhibit superparamagnetic behavior above a characteristic T_B with zero H_c and zero M_r (Figure 1.18b).[42] If the temperature is lower than T_B, the NCs show ferromagnetic/ferrimagnetic behavior again (Figure 1.18c). This peculiar property of NCs has been exploited in various applications. For example, colloidal NCs can dissipate heat under AC magnetic fields.[43] Due to the rapid thermally induced magnetization reversal, magnetic NCs with a high magnetocrystalline anisotropy energy can increase their local temperature, which can damage targeted cancer cells.[11,43,44] Riedinger *et al.* reported that iron oxide NCs can elevate their local temperature up to 45 °C in water by using the thermal

decomposition of a thermo-sensitive azobis[N-(2-carboxyethyl)-2-methylpropionamidine].[45] This type of cancer treatment is called thermal ablation or hyperthermal cancer treatment.[11,30,43,46–48]

The rapid, thermally induced reversal of the magnetic moments of NCs is an attractive feature for high frequency devices. Increasing the power density of systems and the operating frequencies of devices is essential for the miniaturization of power converters. To enhance the power density of devices such as inductors and transformers in a power converter, magnetic materials are often inserted as cores. As has been discussed in the Chapter 1.4, magnetic materials raise the magnetic field density inside a given material. This increases the power density of an inductor and thus the loss of inductance caused by the reduction of size can be compensated by utilizing higher permeability magnetic core materials. Increasing operating frequencies is another way to reduce the size of a power converter by decreasing the required energy storage per switching period for the same amount of power level.[49] Therefore, it is the essential to develop a magnetic material operable at high AC magnetic frequencies for a miniaturized power converter. In this study, we would like to utilize the superparamagnetic character of magnetic NCs for miniaturized devices operable at high frequencies.

1.6 Biomass Conversion via Bimetallic NCs

Platinum-based heterogeneous catalysts have been studied for renewable biofuel energy. The hydrodeoxygenation (HDO) of 5-hydroxymethylfurfural (HMF) into 2,5-dimethylfuran (DMF) is one of the most interesting biomass conversion processes. HMF is readily converted from abundant renewable carbohydrates such as glucose and fructose at high yield through dehydration,[50–52] but its high reactivity and boiling point preclude its use as an automotive fuel. DMF is a promising molecule as a biofuel material due to its high energy density (30 kJ/cm^3) and low boiling point.[53] The key to utilize DMF as a biofuel is to increase the conversion of HMF and selectivity for DMF. Thus far, various metals including Pt,[6] Pd,[54,55] Ru,[56] CuRu,[53] and PdAu[57] have been adopted as heterogeneous catalysts for this reaction. The most promising material that has been reported so far is PtCo bimetallic nanoparticles by Schüth *et al*.[7] They reported that Pt_3Co nanoparticles in a hollow carbon sphere could catalyze the HDO of HMF into DMF with 100 % conversion of HMF and 98 % selectivity for DMF.

This work motivated the interests in the HDO activity of colloidal NCs. Even though colloidal NCs have been utilized as heterogeneous catalysts in many reactions such as CO oxidation,[58,59] CH_4 combustion,[60,61] and water splitting,[38,62] there has been no report in regard to the HDO of HMF into DMF catalyzed by colloidal NCs. Colloidal NC synthesis *via* solvothermal techniques is very useful tool to analyze and optimize catalytic materials' properties. The synthetic

technique can easily control the size[29] and shape,[63] which are reported to be critical in catalysis. Furthermore, since bimetallic NCs can add another degree of freedom in manipulating materials' properties by tuning the ratio between one element and the other, it is possible to optimize the composition of NCs to increase the selectivity for DMF.

1.7 Thesis Overview

The goals of this thesis are to synthesize d-block transition metal based NCs and understand their magnetic and catalytic properties. The theme is divided in two parts: magnetics (chapter 2, 3, and 4) and catalysis (chapter 5). In the first part of this thesis, the synthesis, structural analysis, and direct current (DC) & alternating current (AC) magnetic properties of spinel ferrite NCs are discussed for low energy loss magnetic devices. In the later part of the thesis, Pt based bimetallic NCs are synthesized and their catalytic properties are discussed.

In Chapter 2, the size and chemical composition controlled synthesis of iron oxide NCs is presented. Two sets of oxides are studied, (a) as synthesized, magnetite-rich and (b) aged, maghemite NCs. With these sets of NCs, we investigated the size and composition dependent AC magnetic permeability of superparamagnetic iron oxide NCs for radio frequency (RF) applications. In Chapter 3, I discuss the synthesis of $M_xFe_{3-x}O_4$ (M=Mn, Co, Zn) NCs with varied sizes. I observed that doping 3d metals into iron oxide NCs affect their DC and

AC magnetic behaviors significantly. $Zn_{0.25}Fe_{2.75}O_4$ NCs are embedded into microfabricated inductors and their AC properties and temperature dependent efficiencies are studied. Then, I further demonstrate the DC and AC magnetic property control *via* ligand exchange with dendrimers. In Chapter 4, I discuss the temperature dependent energy efficiencies of a power converter with an NC core inductor. In Chapter 5, the synthesis and catalytic behaviors of PtM (M=Co, Mn, Fe, Ni, and Cu) are described. The bimetallic NCs are prepared with controlled size and compositions and PtCo NCs show clear composition dependence in the HDO of HMF into DMF. Especially, the HDO reaction of HMF over a Pt_3Co_2 NC catalyst yielded 98 % selectivity for DMF with 100 % HMF conversion. We analyzed the reactions by interpreting the side-products from the reaction using a continuous flow reactor. The DFT calculation studies reveal why PtCo bimetallic NCs can be more selective for DMF than Pt NCs.

CHAPTER 2. Size and Composition Dependent Magnetic Permeability of Iron Oxide NCs at Radio Frequencies (Chapter 2.3 collaborated with Dr. Georgia Papaefthymiou)

2.1 Introduction

Magnetic NCs have been widely used for applications such as DC[64–66] and AC[67–69] electromagnetic devices, medical diagnostics,[12,13,70] clinical therapy,[11,71,72] and stealth technology.[73–75] Among the various ac applications, the use of nanocrystalline magnetic materials in the design of inductors[76–78] and transformers[79–81] is of particular interest due to the desire to reduce the volume of magnetic components for the miniaturization of electromagnetic devices. Incorporating the magnetic colloidal NCs offers the potential for low-cost and rapid fabrication of the miniaturized devices via simple solution-based deposition and infiltration.[82–85] In addition, the properties of magnetic NCs are tunable with precisely controlled size, shape, and composition,[22,30,86] which provides a new scope to improving the performance of electromagnetic devices.

In order to utilize magnetic NCs in miniaturized magnetic components, achieving high operating frequencies while benefiting from the high permeability of magnetic core material is critical.[87–91] However, magnetic materials under high

frequency field often suffer from low ferromagnetic resonance frequency, hysteresis loss, and eddy current loss. Ferromagnetic resonance occurs when the frequency of an external AC magnetic field coincides with the precession frequency of the magnetization vector around the anisotropy field in the ferromagnetic material.[28] At the resonance frequency, magnetic energy is absorbed and subsequently dissipated as heat. Simultaneously, the magnetization relaxes back to its original magnetization direction and precession mode. Hysteresis loss is energy wasted in repeatedly reversing the magnetization direction of ferromagnetic materials under an AC field.[28] Microscopically, this loss comes from the energy required for field activation over domain wall pinning sites, and the subsequent loss of this energy to the lattice after field activation completes.[41,92] Eddy current loss is the resistive power dissipation from the induced current inside a conductive material.[28] These effects limit the operation of RF electromagnetic devices with conventional magnetic cores such as Permalloy, Supermalloy, nickel zinc ferrite, and manganese zinc ferrite.[28,93,94]

Superparamagnetic NCs are good candidates for low loss RF magnetic materials. Superparamagnetic behavior is expressed in single domain magnetic nanoparticles due to thermally induced magnetic reorientation above T_B. The Néel relaxation time, τ_N, of superparamagnetic NCs is expressed in the Néel-Arrhenius equation, $\tau_N = \tau_0 \, exp(\frac{E_a}{k_B T})$, where the physical parameters of NCs are

defined as follows: $1/\tau_0$ is attempt frequency for magnetization reversal, E_a is the anisotropy barrier for the particle which, in the absence of interparticle interactions, is taken to be KV where K is the magnetic anisotropy energy density and V is the volume of the NC, and K_B is the Boltzmann constant. Thermally assisted magnetization reversals can take place and the nanoparticles exhibit superparamagnetic behavior above a characteristic T_B with zero coervicity.[37,41,42] Therefore, the superparamagnetic behavior of NCs can effectively suppress hysteresis loss at high frequencies. Since the NCs are surrounded by an insulating organic ligand shell, rendering the NC ensemble non-conductive, eddy current loss is also suppressed/eliminated. Recently, Kura *et al*. reported size dependent high frequency dynamics of Fe NCs[69] and Song *et al*. reported an increased cutoff frequency for Fe_3O_4 NCs after coating the iron oxide cores with SiO_2 shells.[68] These results show that the ferromagnetic resonance frequency of superparamagnetic NCs can be pushed to more than 1 GHz, which strongly motivates the use of magnetic NCs to RF devices. Further investigation is still necessary to understand how the size, shape, crystalline structure, and chemical composition of NCs affect their magnetic permeability at RFs in order to design the NC-based ac devices with optimized RF magnetic properties. In addition, understanding RF properties of magnetic NCs is important for their use not only in low energy loss applications, but also where high energy loss is desired

applications like hyperthermia cancer treatment which needs to maximize losses to enhance the thermal energy release from NCs.[11,30,43,44]

So far, numerous studies have investigated the DC magnetic properties of nearly monodisperse NCs such as iron oxide,[3] ferrites,[22,30] cobalt,[86,95] nickel,[24,96] and FePt.[66,97] Although there has been increasing interest in utilizing magnetic nanocomposites in ac applications such as inductor cores[68,69,76] and hyperthermia cancer treatment,[11,30,43,44] the RF frequency magnetic properties of magnetic NCs as a function of size, shape, and composition are not well understood. In the case of iron oxide NCs, which are the most widely used magnetic NCs, it has been reported that the stoichiometry of as-synthesized iron oxide NCs changes from magnetite (Fe_3O_4) rich to maghemite (γ-Fe_2O_3) rich structure upon oxidation.[98] It is well known that this oxidation severely affects the DC magnetic properties,[99] but concomitant changes in ac magnetic properties under RF field have not been studied in depth.

In this chapter, superparamagnetic iron oxide NCs are systematically examined to understand the particle size and composition dependence of magnetic permeability. As-synthesized and naturally oxidized iron oxide NCs (oxidized under ambient condition) are compared to clarify the composition or stoichiometry dependence of magnetic permeability and the environmental stability of iron oxide NCs. For both sets of NCs, structure stoichiometry, electronic and magnetic characteristics are analyzed using Mössbauer

spectroscopy, DC magnetization measurements via superconducting quantum interference device (SQUID) magnetometry, and ac magnetic characterization by using a one-turn inductor model with Agilent 4395A impedance analyzer and a 16454A magnetic material test fixture. Finally, the ac characterization of inductors with iron oxide NC cores is conducted.

2.2 Synthesis of Iron Oxide NCs

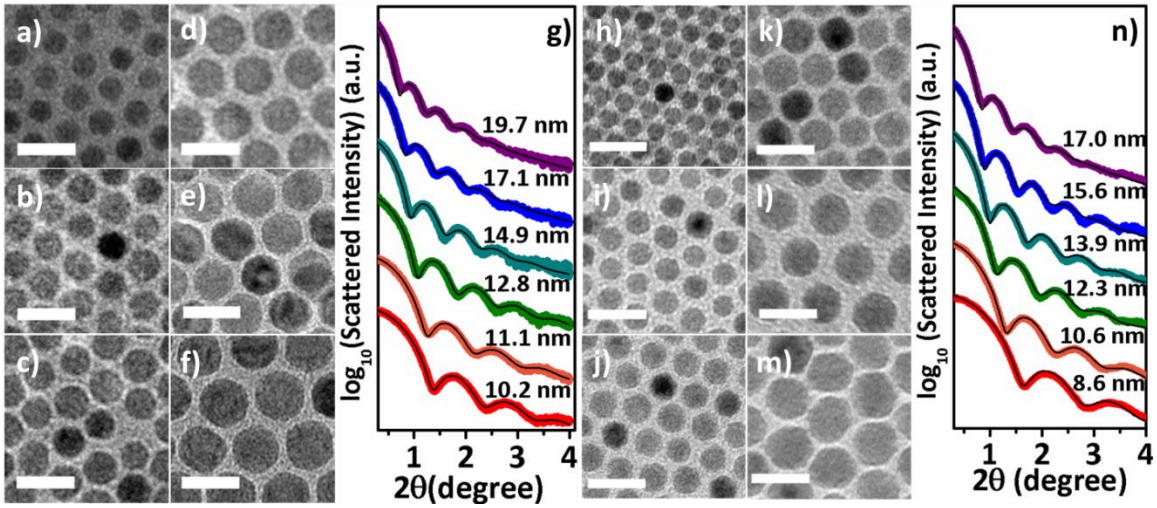

Figure 2.1. The set of images on the left half represent the TEM images of a) 10.2 nm, b) 11.1 nm, c) 12.8 nm, d) 14.9 nm, e) 17.1 nm, f) 19.7 nm as-synthesized iron oxide NCs and g) their SAXS data. The set of images represent on the right half the TEM images of h) 8.6 nm, i) 10.6 nm, j) 12.3 nm, k) 13.9 nm, l) 15.6 nm, m) 17.0 nm aged iron oxide NCs and n) their SAXS data. All the scale bars represent 20 nm. The black lines in the SAXS data represent the simulated fits for each size of the NCs.

Monodisperse iron oxide NCs are synthesized by modifying the method reported by Hyeon *et al*.[3] and Chen *et al*.[100] First, iron oleate precursors are prepared using the following procedure. 10.8 g of iron (III) chloride, 36.5 g of sodium oleate, 40 mL of DI water, 40 mL of ethanol, and 80 mL of hexane are mixed into a 500 mL three-neck flask. The mixture is refluxed at 60 °C for 4 hours. The red-black colored iron oleate precursors are washed with DI water for 3 times. The main difference from the reported method is that the iron oleate precursors are centrifuged to get rid of leftover amount of sodium oleate, which significantly improves the reproducibility of the iron oxide NC synthesis. Then, the solution is dried by using rotary evaporator. Then, the precursors are kept under vacuum overnight. Second, 10.2 nm iron oxide NCs are synthesized by adding 7.2 g of iron oleate precursors, 1 mL of oleic acid, and 20 mL of 1-octadecene into a three-neck flask. The reaction mixture is heated to 100 °C and kept under vacuum for 1 hour. Then, the mixture is heated to 315 °C at a rate of 3 °C/min. After 30 minutes, the reaction mixture is cooled down to room temperature and precipitated by adding ethanol. The precipitate is re-dispersed in hexane and washed with ethanol twice more. Finally, the iron oxide NCs are re-dispersed in hexane and kept in a glove box. By increasing the amount of oleic acid added into the mixture, the size of iron oxide NCs is increased. Aged iron oxide NCs are kept in ambient conditions over a year. In Figure 2.1, the TEM images of as-synthesized iron oxide NCs (Figure 2.1a-f) and aged iron oxide NCs (Figure

2.1h-m). In order to precisely analyze the size dependent properties, it is essential to determine the size and size distribution of NCs by bulk-based measurements, collecting ensemble average structural information, which are presented in Figure 2.1g (as-synthesized samples) and 2.1n (aged samples). The NCs exhibit good monodispersity with the size deviation from 7 % to 9 % based on SAXS fitting and from 5 % to 8 % based on the TEM images (Figure 2.2 and 2.3). All the NC sizes referred in this report are the values calculated by SAXS fitting.[101] The average size of NCs is determined by SAXS measurement with the experimental data fitted to the standard spherical model weighted by log-normal distribution, which are presented as black curves in the SAXS data. The size ranges are from 10.2 nm to 19.7 nm of as-synthesized iron oxide NCs and from 8.6 nm to 17.0 nm of aged iron oxide NCs. Iron oxide NCs in this size range are selected for study because (a) NCs in this range show superparamagnetic behavior and (b) can be easily dispersed in volatile solvents such as hexane and toluene, which have potential to be used in solution-based deposition processes.

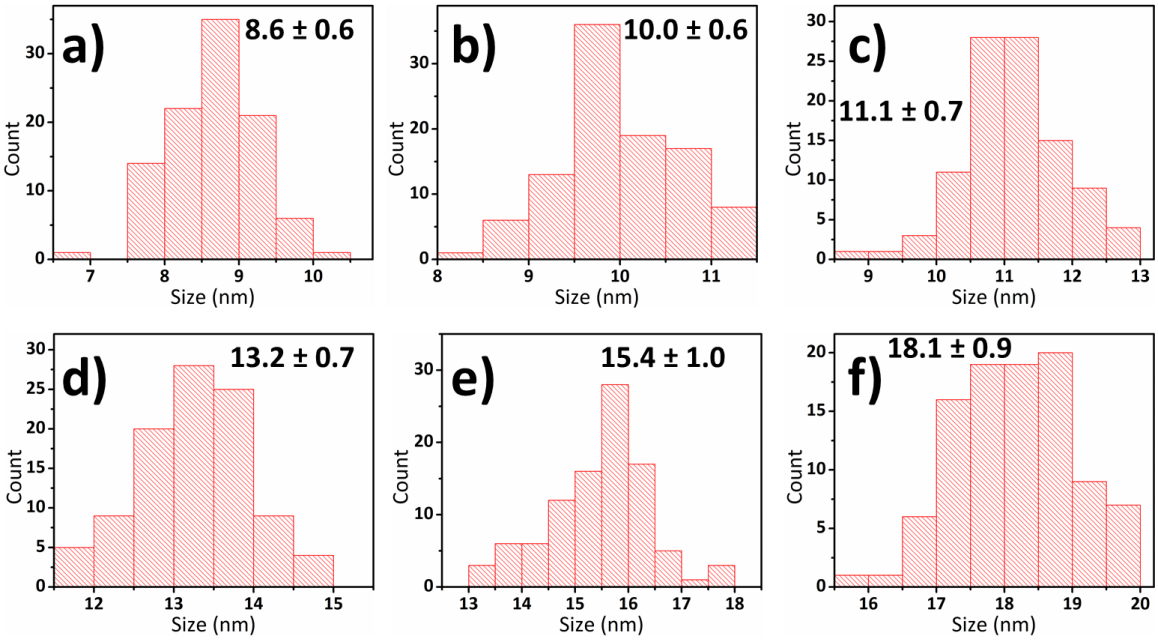

Figure 2.2. The count of size of a) 10.2 nm, b) 11.1 nm, c) 12.8 nm, d) 14.9 nm, e) 17.1 nm, and f) 19.7 nm as-synthesized iron oxide NCs from TEM images. The numbers in the figures are the average size and standard deviation based on the TEM images.

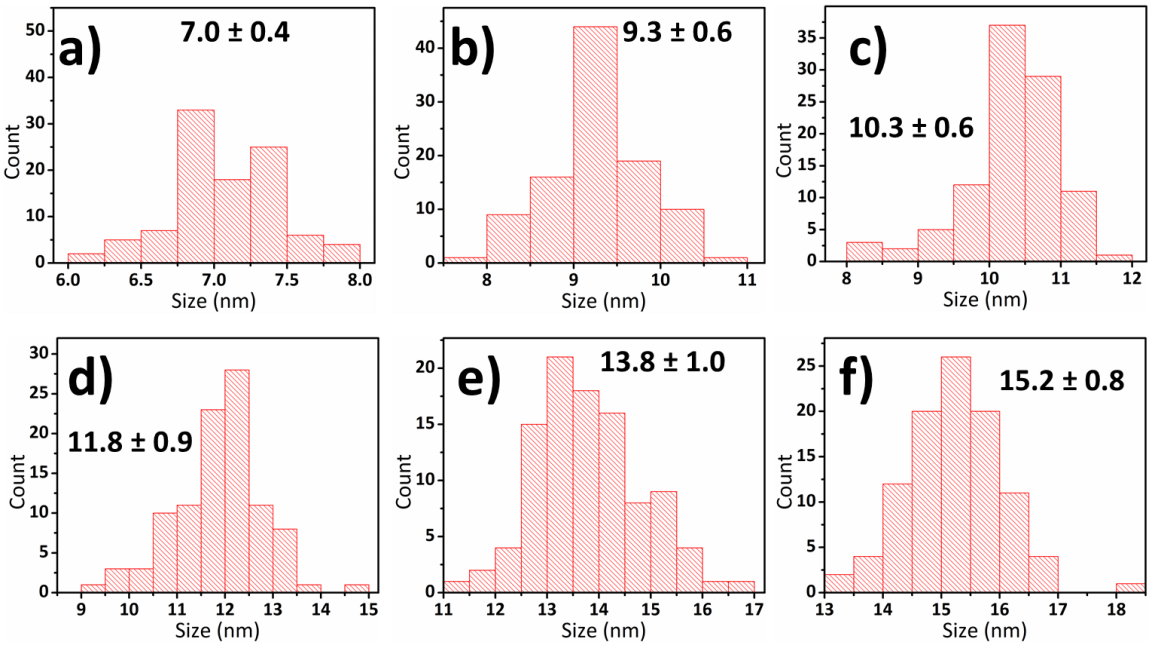

Figure 2.3. The count of size of a) 8.6 nm, b) 10.6 nm, c) 12.3 nm, d) 13.9 nm, e) 15.6 nm, and f) 17.0 nm as-synthesized iron oxide NCs from TEM images. The numbers in the figures are the averaged size and standard deviation based on the TEM images.

2.3 Composition Analysis on Iron Oxide NCs with Mössbauer Spectroscopy

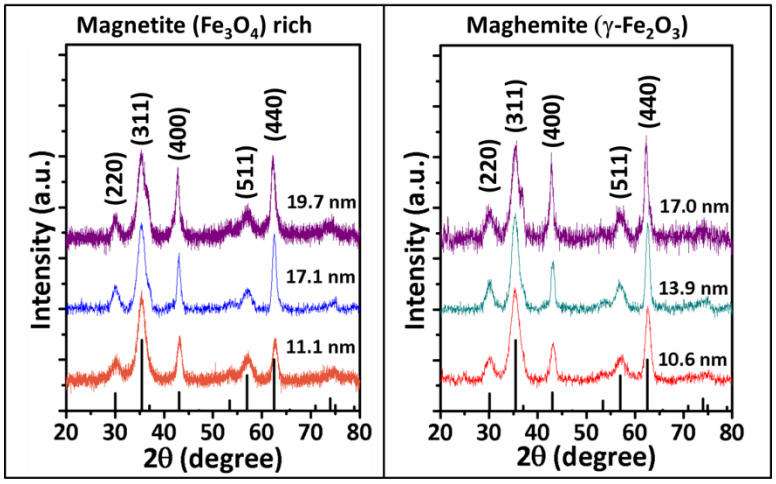

Figure 2.4. Wide angle x-ray scattering (WAXS) data of selected samples of magnetite-rich (left) and maghemite iron oxide NCs (right).

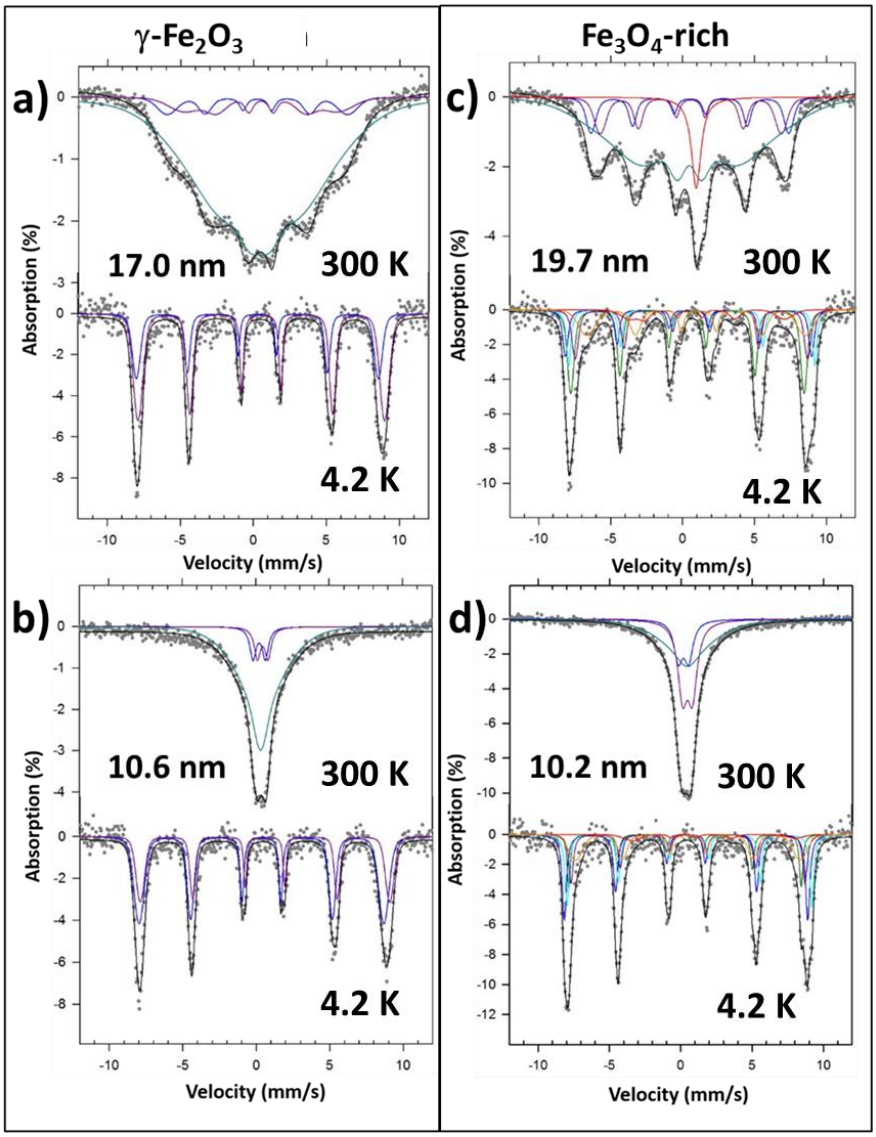

Figure 2.5. Mössbauer spectra of selected NC samples. Left side: maghemite NCs at 300 K and 4.2 K (a) 17.0 nm, (b) 10.6 nm. Right side: magnetite-rich NCs at 300 K and 4.2 K (c) 19.7 nm, (d) 10.2 nm. The experimental points are least square fitted (black line) to a superposition of theoretical spectra of tetrahedral (A) (blue) and octahedral [B] (purple) sites, intermediate relaxation (IR) components (cyan) and interfacial $Fe_{1-x}O/Fe_3O_4$ phases (red) (see text and Table 2.1)

Polymorphs of iron oxide crystal structures include magnetite (Fe_3O_4), maghemite (γ-Fe_2O_3), hematite (α-Fe_2O_3) and wüstite ($Fe_{1-x}O$). Although the composition of iron oxide synthesized from iron-oleate precursors is known to be primarily a mixture of magnetite and maghemite,[3] magnetite can be further oxidized under air to form maghemite structures.[98] In the magnetite structure, all of the Fe^{2+} ions and half of the Fe^{3+} ions are found in octahedral [B] sites. The other half of Fe^{3+} ions is found in tetrahedral (A) sites. This is known as the inverse spinel structure. As oxidation proceeds, Fe^{2+} ions diffuse outwardly from the interior of the iron oxide NCs towards the surface of the particle, while the particle keeps its morphology and crystal structure.[98] The oxidation of Fe^{2+} ions reduces both the M_S and magnetic anisotropy of the iron oxide NCs, which in turn can alter their ac magnetic behavior.[39,99] Therefore, it is important to determine the degree of ferrous iron oxidation in the magnetite structure of our iron oxide NCs.

As it is difficult to distinguish magnetite NCs from maghemite NCs with x-ray diffraction due to their similar crystal structures (Figure 2.4), we use Mössbauer spectroscopy to probe the electronic structure of the iron ions in order to determine their oxidation state and thus derive the stoichiometry of our as-synthesized (magnetite-rich) and aged (maghemite) NCs. Depending on the oxidation state and local environment around the iron ions, the gamma ray absorption energy varies and thus it is possible to determine the local sites that

the iron ions occupy. Representative data are shown in Figure 2.5. The black solid line through the experimental points is a least square fit to a superposition of theoretical spectra shown in colored solid lines corresponding to different iron subsites in the structure. The left half of Figure 2.5 shows the Mössbauer spectra of (a) 17.0 nm and (b) 10.6 nm maghemite NCs at 300 K and 4.2 K, while the right half shows the corresponding spectra for (c) 19.7 nm and (d) 10.2 nm magnetite-rich NCs. The selected sizes presented correspond to relatively large and small particles studied. All the interpretations and descriptions about the Mössbauer data are completed by my collaborator, Prof. Georgia Papaefthymiou. At 4.2 K, sharp magnetically split spectra are observed in all cases indicating blocked particle magnetic moments with a relaxation time, $\tau_N > \tau_L$, where $\tau_L \approx 10$ ns is the Larmor precession time of the iron excited state nuclear spin in the internal magnetic field of the particle.[102] As described below, spectral analysis of these blocked (slow relaxation) magnetic spectra permits the estimation of the degree of iron oxidation in the spinel crystallographic structure, (i.e., stoichiometry) of the samples. At 300 K the spectra of the larger NCs (17.0 nm maghemite and 19.7 nm magnetite-rich) sit on a broad, absorption envelope due to the presence of intermediate relaxation (IR) effects ($\tau_N \approx \tau_L$). In contrast, the spectra of the smaller NCs (10.6 nm maghemite and 10.2 nm magnetite-rich) exhibit motional narrowing due to fast relaxation effects ($\tau_N < \tau_L$) at 300 K.

At 4.2 K spectra of maghemite samples are fit to superpositions of iron subsites corresponding to tetrahedral (A) (spectral component in blue) and octahedral [B] (spectral component in purple) iron sites.[103] Parameters derived from spectral fitting are tabulated in Table 2.1. These spectral signatures are consistent with the presence of γ-Fe_2O_3 NCs. At 300 K an additional broadened absorption envelope (spectral component in cyan) is superimposed, which arises from a complex interplay between thermally driven collective magnetic excitations[104] of the magnetization about the anisotropy axes of the particles and interparticle interactions.[105] The latter are stronger in samples containing larger particles, due to their larger net moments, whereas the former are enhanced in smaller sized particles. Magnetic dipole-dipole interactions between particles prevent the NC assemblies from fully entering the superparamagnetic regime within the characteristic measuring time of the Mössbauer technique of τ_{Moss} = 10 ns, which is 8 to 9 orders of magnitude shorter than that of SQUID magnetometry, where τ_{SQUID} = 1 to 100 s. This results in the broad absorption envelopes observed that are characteristic of IR effects (simulated by the broadened spectral components in cyan) at room temperature. For the smaller maghemite particles in Figure 2.5, interparticle interactions are weakened due to their smaller net moments, leading to motional narrowing and collapse of the magnetic spectral signature at room temperature as the particles increasingly enter the superparamagnetic regime. That is, at room temperature the spectra of the 17.0

nm maghemite NCs are dominated by IR effects due to stronger interparticle interactions, while those of the 10.6 nm NCs are dominated by fast relaxation effects producing largely collapsed, paramagnetic doublets indicating mostly superparamagnetic (non-interacting) particles at the Mössbauer time scale.

Table 2.1. Mössbauer hyperfine parameters derived from spectral fits. δ, Isomer shift relative to metallic iron at 300 K, ΔE_Q, Quadrupole splitting, H_{hf}, Hyperfine magnetic field, (A), tetrahedral sites, [B], octahedral sites, IR, Intermediate Relaxation, Interfacial, $Fe_{1-x}O/Fe_3O_4$

Sample	T (K)	Site Identification	δ (mm/s)	ΔE_Q (mm/s)	H_{hf}(T)	Area (%)
γ-Fe_2O_3						
17.0 nm	300	Fe^{3+} (A)	0.25	-	38.2	7
		Fe^{3+} [B]	0.50	-	32.4	9
		IR	0.41	-	-	84
	4.2	Fe^{3+} (A)	0.32	-	51.3	50
		Fe^{3+} [B]	0.57	-	52.3	50
10.6 nm	300	Fe^{3+} (A)	0.25	0.85	-	10
		Fe^{3+} [B]	0.49	0.73	-	9
		IR	0.38	-	-	91
	4.2	Fe^{3+} (A)	0.35	-	51.5	62
		Fe^{3+} [B]	0.60	-	52.5	38
Fe_3O_4-rich						
19.7 nm	300	Fe^{3+}(A)	0.32	-	42.5	11
		$Fe^{2.5+}$[B]	0.58	-	38.9	13
		IR	0.48	-	-	68
		Interfacial*	0.95	-	-	8
	4.2	Fe^{3+}(A)	0.33	-	50.2	29
		Fe^{3+}[B]	0.41	-	53.0	13.4
		Fe^{3+}[B]	0.63	-	52.9	14.2
		Fe^{2+}[B]	1.02	-0.18	47.0	19
		Fe^{2+}[B]	1.10	1.19	33.4	7
		IR*	0.61	-	49.9	18
10.2 nm	300	Fe^{3+}(A)	0.19	0.72	-	18
		$Fe^{2.5+}$[B]	0.46	0.70	-	37
		IR	0.46	-	-	45
	4.2	Fe^{3+}(A)	0.32	-	50.2	25
		Fe^{3+}[B]	0.34	-	52.7	30
		Fe^{3+}[B]	0.61	-	53.0	22
		Fe^{2+}[B]	1.20	1.95	36.3	5
		Fe^{2+}[B]	1.19	-	48.1	17
		IR	0.58	-	50.2	16

In the case of magnetite-rich NCs, the situation is further complicated by the well-known Verwey transition,[106] which is a first-order metal-insulator transition, originating from a slight distortion in the crystal structure from inverse cubic spinel to monoclinic, occurring at T_V = 120 K in the bulk. The low temperature monoclinic form has discrete iron valence states producing sharp absorption spectra. Above T_V fast electron hoping takes place between the Fe^{2+} and Fe^{3+} ions in octahedral [B] sites resulting in pair-wise electronic delocalization. This drastically changes the Mössbauer spectral features to the superposition of two magnetic components corresponding to $Fe^{2.5+}$ in [B] sites (simulated in purple) and Fe^{3+} in (A) sites (simulated in blue) at room temperature.[107,108] Again in order to properly simulate these 300 K spectra, an additional severely broadened absorption envelope had to be superimposed (simulated in cyan) corresponding to (IR) spectra. Additionally, the larger NCs of 19.7 nm diameter contain a small amount (~8%) of a paramagnetic iron component identified as wüstite ($Fe_{1-x}O$), indicated by the relatively sharp spectral feature in red in Figure 2.5c.[109] Wüstite contains only Fe^{2+}, is paramagnetic at room temperature and undergoes a paramagnetic-to-antiferromagnetic phase transition at 200 K. It has been previously reported to coexist in large particles of magnetite as an interfacial $Fe_{1-x}O/Fe_3O_4$ phase.[110]

The degree of iron oxidation can be determined from the relative spectral areas of the different iron subcomponents, under the assumption that the recoil-

free fraction[3] is similar for all iron sites. This assumption is more valid at low temperatures. Therefore, we have made use of the 4.2 K spectra to determine the stoichiometry of the magnetic component ascribed to Fe_3O_4 within the spectral decomposition of our NCs. For stoichiometric magnetite one expects an intensity ratio of Fe^{2+} to Fe^{3+} iron of 1:2. Deviations from this value in our measured spectra are used to get an estimate of the degree of oxidation of our magnetite-rich NCs.[111] However, our NCs contain additional Fe^{2+} assigned to $Fe_{1-x}O$ or interfacial $Fe_{1-x}O$-Fe_3O_4 phases, which however remain largely unresolved at 4.2 K but contribute to the broad IR spectral absorption envelopes (Table 2.1). For the 19.7 nm magnetite-rich NCs we obtain Fe^{2+}/Fe^{3+} = 0.464 indicating a level of 7.2 % oxidation. For the 10.2 nm NCs this ratio has dramatically decreased to Fe^{2+}/Fe^{3+} = 0.285 indicating an oxidation level of 43%, which is similar to the degree of oxidation reported by Hyeon *et al*.: Fe^{2+}/Fe^{3+} = 0.285 in the case of 9 nm and Fe^{2+}/Fe^{3+} = 0.43 in the case of 16 nm particles.[3]

2.4. DC Magnetic Characterization of Iron Oxide NCs

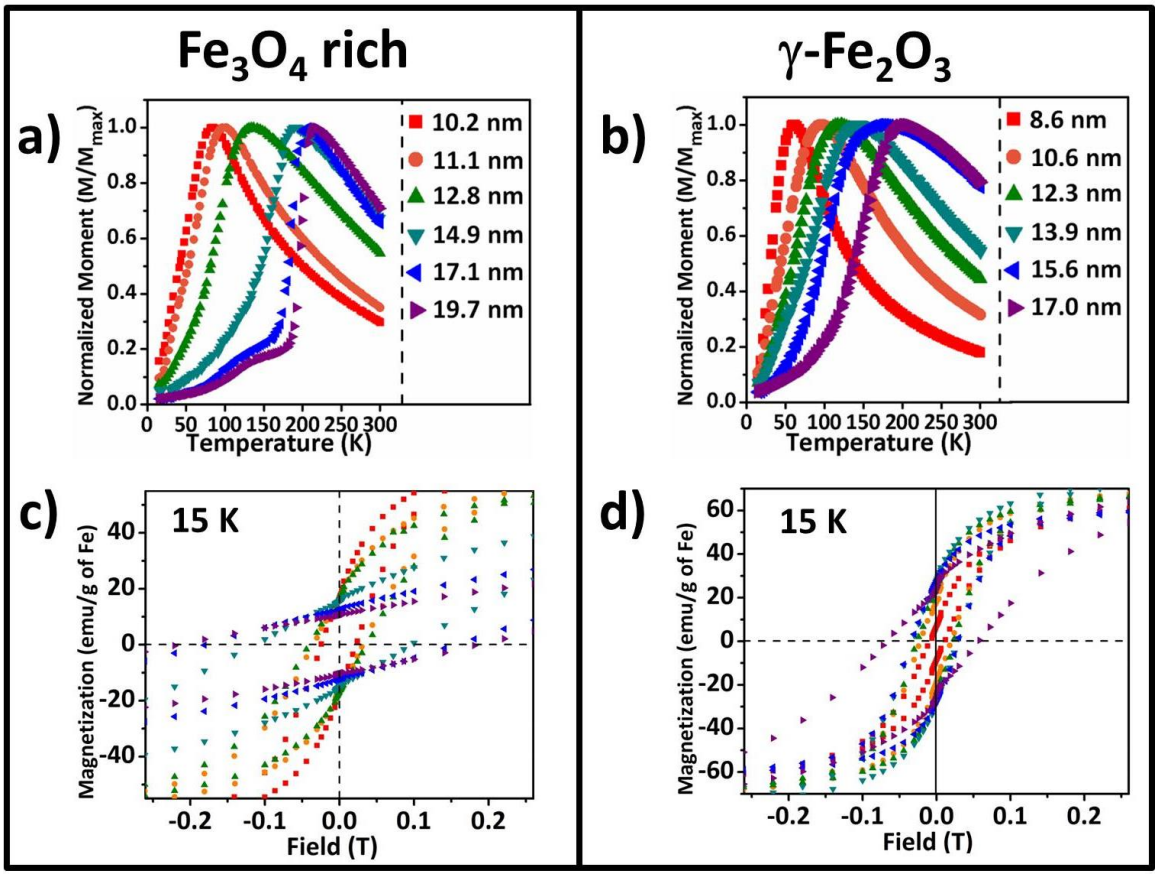

Figure 2.6. Zero-field cooling curves of a) magnetite-rich iron oxide and b) maghemite iron oxide samples in different sizes. Enlarged hysteresis curves of c) magnetite-rich iron oxide NCs and d) maghemite iron oxide NCs at 15 K.

Figure 2.6 displays the DC magnetic characterization of iron oxide NCs. T_B, H_c, and the ratio between M_r and M_s at 15 K are summarized in Table 2.2. For zero field cooled (ZFC) measurements, the NCs are cooled from 300 K to 15 K without an external magnetic field. Then, a 0.01 T static magnetic field is applied

and the magnetic moment of the sample is measured as the temperature returns to 300 K. T_B is determined at the maximum value of the normalized magnetic moment, M/M_{max}. This observed T_B is dependent on the time scale of observation[15,112] and results from the combined effect of the magnetic anisotropy barrier, KV, of the isolated particle and the interparticle interactions, both of which become stronger with increasing particle size. For the larger NCs, we expect interparticle interactions to be sizable producing a maximum in the magnetization of the ZFC curves at 200 K, which is best described as a spin-freezing temperature due to strong dipole-dipole interactions between particles resulting in a spin-glass-like system within the granular assembly. The presence of strong interparticle interactions is evinced by (a) the shape of the ZFC/FC curves and (b) the values of M_r/M_s at 15 K, as well as (c) the presence of the IR spectral features in the room temperature Mössbauer spectra, as we have discussed above.

Table 2.2. H_c values at 15 K, T_B, and the ratio between M_r and M_s of iron oxide NCs.

Fe_3O_4-rich				γ-Fe_2O_3			
Size (nm)	**H_c at 15 K (mT)**	**T_B (K)**	**M_r/M_s**	**Size (nm)**	**H_c at 15 K (mT)**	**T_B(K)**	**M_r/M_s**
10.2 ± 0.8	32	85.2	0.17	8.6 ± 0.7	12	62.1	0.09
11.1 ± 0.9	35	100.7	0.21	10.6 ± 0.8	20	98.3	0.22
12.8 ± 0.9	40	134.1	0.23	12.3 ± 1.0	24	120.8	0.31
14.9 ± 1.2	115	191.62	0.22	13.9 ± 1.0	33	142.4	0.29
17.1 ± 1.5	181	208.9	0.21	15.6 ± 1.2	33	174.4	0.37
19.7 ± 1.7	215	217.5	0.19	17.0 ± 1.5	58	203.1	0.24

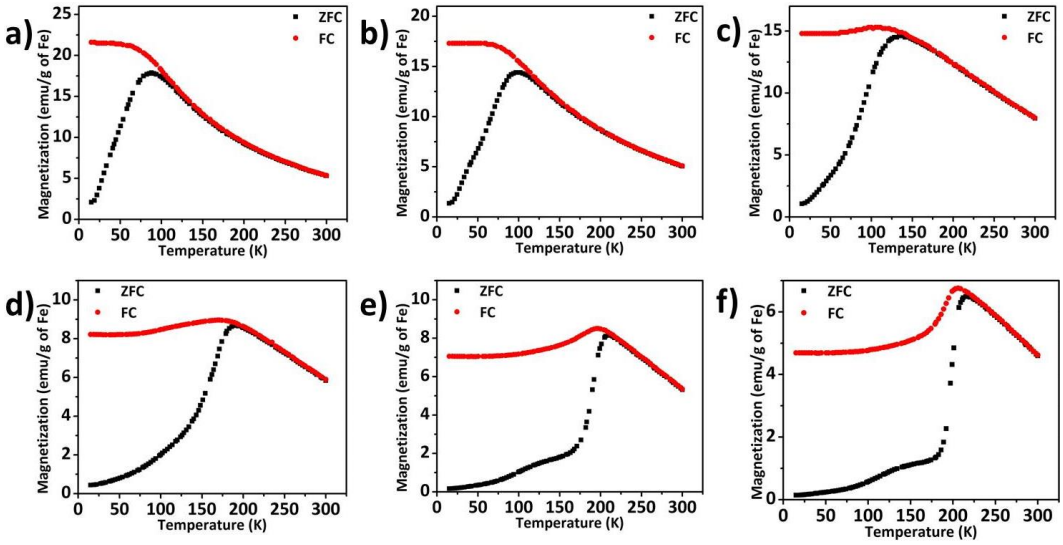

Figure 2.7. FC (red circles) and ZFC (black squares) curves of a) 10.2 nm, b) 11.1 nm, c) 12.8 nm, d) 14.9 nm, e) 17.1 nm, and f) 19.7 nm magnetite-rich iron oxide NCs.

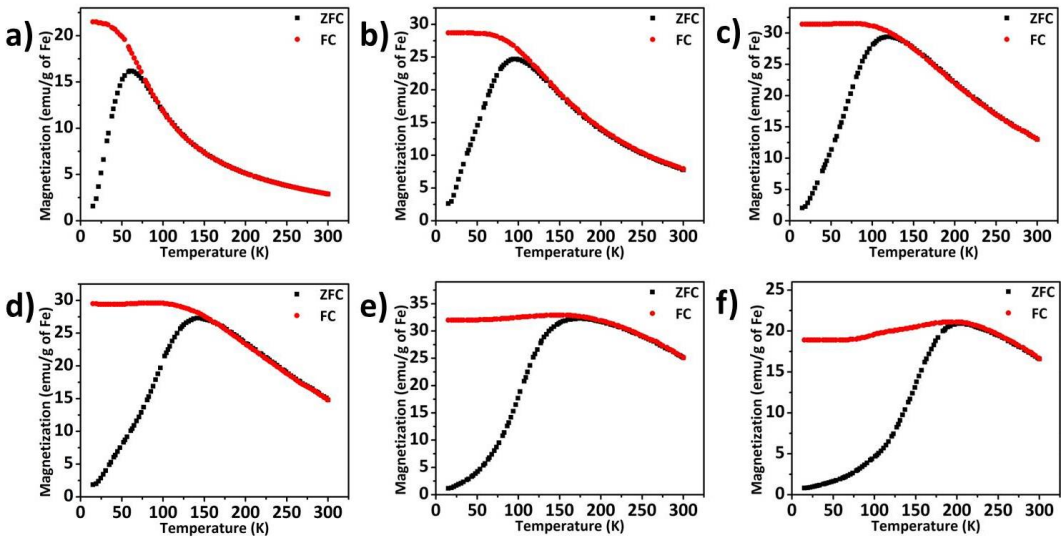

Figure 2.8. FC (red circles) and ZFC (black squares) curves of a) 8.6 nm, b) 10.6 nm, c) 12.3 nm, d) 13.9 nm, e) 15.6 nm, and f) 17.0 nm maghemite iron oxide NCs.

The severe flattening of the field cooled (FC) curves at $T<T_B$ shown in Figures 2.7 and 2.8 is often interpreted as evidence for strong interparticle interactions.[113–115] However, since the spin blocking temperature values of all the samples are below 300 K (Figure 2.6a and 2.6b, Table 2.2), they are confirmed to be in the superparamagnetic state at room or higher temperatures. Also, the hysteresis curves at 15 K (Figure 2.6c, 2.6d, 2.9 and 2.10) and 300 K (Figure 2.11) support the observation of the superparamagnetic state of NCs at room temperature. The hysteresis curves at 300 K show zero H_c for all the samples, with size dependent H_c observed at 15 K for both sets of NCs. At 15 K, the as-synthesized magnetite-rich samples exhibit larger coercivities and slanted

hysteresis loops compared to the maghemite samples. This is attributed to the presence of Fe^{2+} in the former and absence in the latter. In maghemite, the local ionic magnetic moment is due only to spin angular-momentum, since the orbital angular-momentum of the half-filled $3d^5$ electronic shell is usually quenched. In contrast, the sixth electron of Fe^{2+} in the magnetite-rich $3d^6$ structures can have unquenched orbital angular momentum,[116] which couples the magnetic moment of the particle to the lattice through the spin-orbit interaction, thus increasing the first magnetocrystalline anisotropy constant in magnetite (K_1 ~-1.1 x 10^4 J/m^3)[93] compared to maghemite (K_1 ~ 10^3 J/m^3)[117]. In turn, this reduces the H_c and produces steeper hysteresis loops in maghemite samples. However, in NCs, surface and strain effects add to the overall effective anisotropy that governs the observed coercivities.[118,119] In addition, differences in the strength of interparticle interactions also contribute.

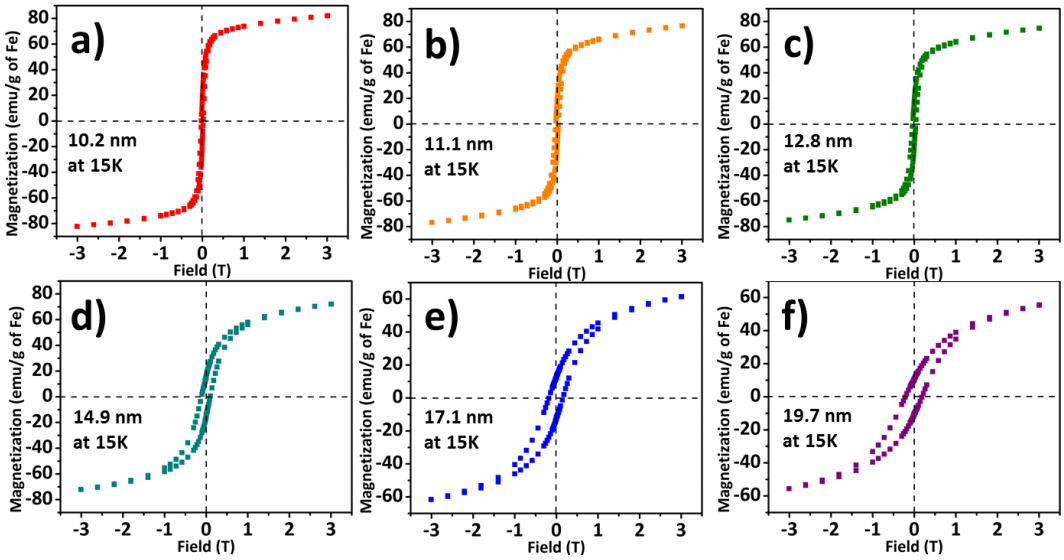

Figure 2.9. Hysteresis curves of a) 10.2 nm, b) 11.1 nm, c) 12.8 nm, d) 14.9 nm, e) 17.1 nm, and f) 19.7 nm magnetite-rich iron oxide NCs at 15 K.

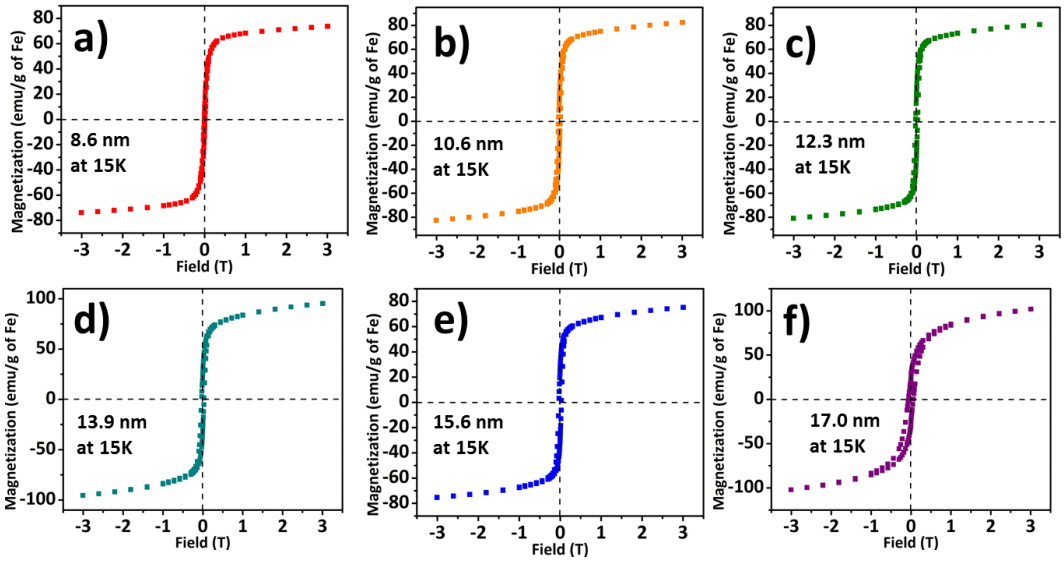

Figure 2.10. Hysteresis curves of a) 8.6 nm, b) 10.6 nm, c) 12.3 nm, d) 13.9 nm, e) 15.6 nm, and f) 17.0 nm maghemite iron oxide NCs at 15 K.

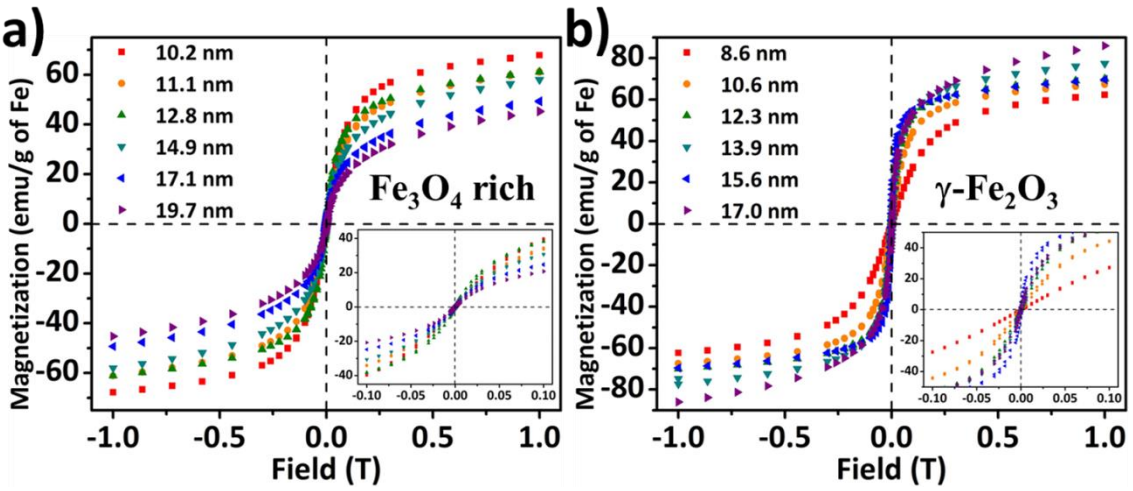

Figure 2.11. Hysteresis curves of a) magnetite-rich iron oxide NCs and b) maghemite iron oxide NCs at 300 K. Insets are the enlarged images of each at low field.

For the magnetite-rich NCs, the overall shape of the ZFC magnetization curves of the larger NCs is qualitatively different than those of the smaller NCs. Specifically, the 17.1 nm and 19.7 nm magnetite-rich NCs have small initial slopes and exhibit a broad hump between 100 K and 150 K, which is absent in the smaller magnetite-rich and in all maghemite NCs. This hump may be partially attributed to the Verwey transition of magnetite, which is known to occur at 120 K in the bulk.[120] However, both small NC size and non-stoichiometry suppress T_V to lower temperatures[121,122] compared to that of the bulk. Anomalies in the magnetization of magnetite NCs have been previously reported to occur above the Verwey transition temperature[123] and have been associated with the complex temperature dependence of the first magnetocrystalline anisotropy constant K_1 of

magnetite.[124] Thus, the observed hump may be associated with the combined effect of this process and the Verwey transition. However, it may also reflect some spin reorientation transition within the particle ensemble. The steep rise of the magnetization at around 200 K for the 19.7 nm and 17.1 nm magnetite-rich NCs in Figure 2.6a is partially due to the presence of wüstite, $Fe_{1-x}O$, which is known to undergo a paramagnetic-to-antiferromagnetic phase transition at 200 K.[109]

The dynamic magnetic properties of NCs are usually examined through the real and imaginary components of the AC susceptibility and their dependence on the frequency of the applied alternating magnetic field. In the dense nanoparticulate samples used in this study to form a toroidal sample, the NCs are not free to rotate. Below T_B, the reversal of the magnetization of the single-domain particle over the anisotropy energy barrier must take place through the Néel spin relaxation process. In a simple phenomenological model, interparticle interactions can be considered as a perturbation to the anisotropy barrier,[105] $E_a = (KV + E_{int})$, where E_{int} gives a measure of the strength of interparticle magnetic interactions.

The presence of interparticle interactions in our NC assemblies is witnessed by the low values of remanence-to-saturation ratio, M_r/M_s, observed in the hysteresis loops at 15 K in Figure 2.6c and d. The magnetite-rich samples have M_r/M_s ~ 0.2 irrespective of NC size, while the maghemite samples exhibit some

variation with values ranging between 0.09 and 0.37 (Table 2.2). It is well known that an assembly of non-interacting, randomly oriented, uniaxial magnetic particles have M_r/M_S = 0.5.[93] Thus, strong interparticle interactions appear to exist in our samples, which are also evinced in the Mössbauer spectra, which show strong IR envelopes persisting to room temperature. Moreover, these low values of remanence-to-saturation ratio reveal the existence of interactions that are overall antiferromagnetic in nature.[125]

2.5. AC Magnetic Characterization of Iron Oxide NCs

The dynamic magnetic properties of nanoparticles are usually studied through ac magnetic susceptibility, χ, measurements. For blocked nanoparticles the relaxation time enters the expressions for the frequency dependence of the real (χ') and imaginary (χ'') parts of the magnetic susceptibility[126] according to equations 2.1 and equation 2.2.

$$\chi' = \chi_\infty + \frac{\chi_0 - \chi_\infty}{1 + (\omega \cdot \tau)^2} \qquad 2.1$$

$$\chi'' = \frac{(\chi_0 - \chi_\infty) \cdot \omega \cdot \tau}{1 + (\omega \cdot \tau)^2} \qquad 2.2$$

Here χ_0 is the initial static susceptibility at zero frequency (initial slopes in Figure 2.11 insets), χ_∞ is the susceptibility at the highest frequency, $\omega = 2\pi f$ and

τ is the relaxation time. At temperatures above T_B the particles become superparamagnetic and the relaxation time $\tau -> \tau_0$ with increasing temperature; the frequency dependence of the complex susceptibility then becomes characteristic of the corresponding bulk material. Thus, according to Equation 2.1 the χ' is expected to exhibit an initial maximum plateau at low frequencies, corresponding to τ_0, when the magnetization has time to respond and follow the applied ac field; it will then start to decrease as the frequency increases, while the χ'' will exhibit a characteristic maximum at a certain frequency. This behavior is reflected in our experimental data of the permeability, μ, where $\mu = \mu_0(1+\chi)$, and μ_0 is the vacuum permeability.

In order to determine the dynamic magnetic properties of our NCs at RFs, we performed relative magnetic permeability measurements, $\mu_r = \mu/\mu_0 = 1+\chi$, as they are more readily related to investigations of their use as inductors. These measurements were conducted using the one-turn inductor model.[127] In this method, a coaxial cable is considered as a one-turn inductor. The reactance and resistance of the one-turn inductor can be measured and converted into the real (μ_r')and imaginary (μ_r'') parts of permeability. The relative permeability (μ_r) is written as Equation 2.3.[127]

$$\mu_r = \frac{(Z_m - Z_{sm})}{jf\mu_0 h \ln\frac{c}{b}} + 1 \qquad 2.3$$

Here Z_m is the impedance measured in the presence of the sample, Z_{sm} is the impedance without the sample, *f* is the frequency of the ac field, *h* is the height of the toroidal sample, *c* is its outer and *b* is its inner diameter of the toroidal sample. Z_{sm} can be calibrated to zero, while Z_m is equal to $R_m + jX_m$, where R_m is the resistance and X_m is the reactance of the sample. This identity is used to rewrite Equation 2.3 as Equations 2.4 and 2.5 with Z_{sm} set to zero.

$$\mu_r = (1 + \frac{X_m}{f\mu_0 h \ln \frac{c}{b}}) - j \frac{R_m}{f\mu_0 h \ln \frac{c}{b}} \qquad 2.4$$

$$= \mu_r' - j\mu_r'' \qquad 2.5$$

Therefore, the relative permeability can be derived from the reactance and the resistance of a one-turn inductor system. The reliability of this method was confirmed by measuring the permeability of commercially available toroidal ferrite cores such as F-23-61, F-23-67, and F-50-68. We observed that our measured values of the μ_r' of all the commercial toroids were consistent with the product information provided by the manufacturer, which confirms the reliability of our measurements for ac magnetic properties. (Figure 2.12)

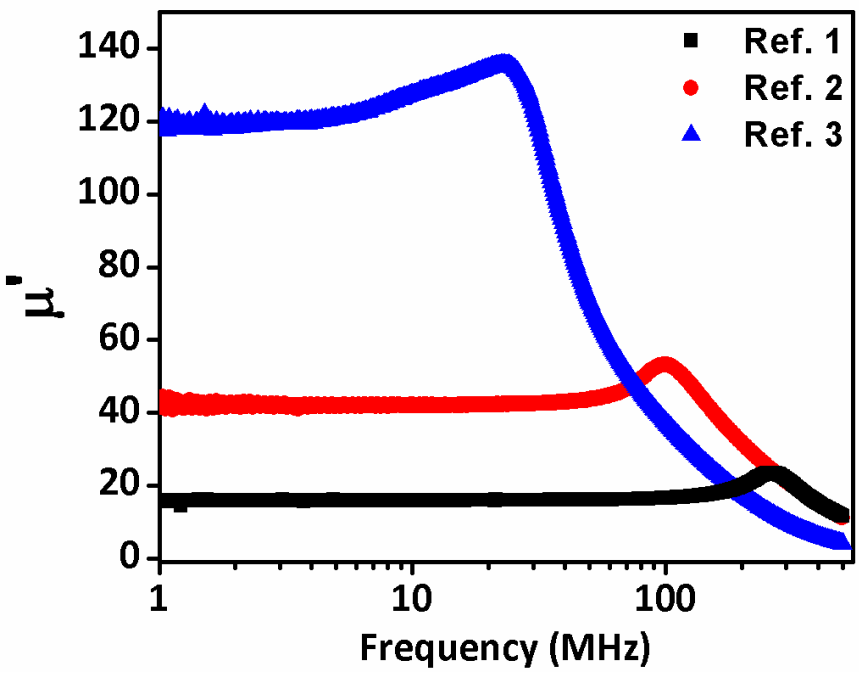

Figure 2.12. The real part of permeability of commercially available ferrite toroid.

With this method, the relative permeability of NCs is measured as presented in Figure 2.13. The μ_r' is the in-phase component of the permeability,[28,41] which is defined as $\mu_r' = (B/H\mu_0)\cos\delta$ where *B* is the magnetic flux in the material, *H* is the external field intensity, and *δ* is the phase delay of *B* relative to *H*. The magnetic flux density of a system is enhanced in proportion to the μ_r'. In Figure 2.13b, the μ_r' of the maghemite NCs in six different sizes shows clear size dependence. In contrast, the size dependence of μ_r' of the as-synthesized magnetite-rich NCs (Figure 2.13a) is not as pronounced as the maghemite NCs reflecting the different sensitivities of the initial susceptibilities to particle size for

the two sets of nanoparticle systems, as observed in the insets of Figures 2.11a and 2.11b. The μ_r' value of the maghemite samples increases as the NC size increases over the whole range of frequencies measured. This can be attributed to the fact that the magnetic flux density in the toroid is enhanced as the NC magnetic moment increases with increasing size of these mono domain NCs. According to the core-shell model of magnetic NCs,[118] the surface-to-volume ratio decreases as the particle size increases. Assuming a shell of disordered surface spins of constant thickness,[30,128] the magnetic moment of single-domain NCs should increase with NC size[129–131] as can be observed from the size dependent M_S of maghemite NCs in Figure 2.14. Still, it is notable that the μ_r' value as a function of frequency starts to drop earlier in the larger NCs. This observation is suspected to arise from the size dependence of the ferromagnetic resonance frequency.[132]

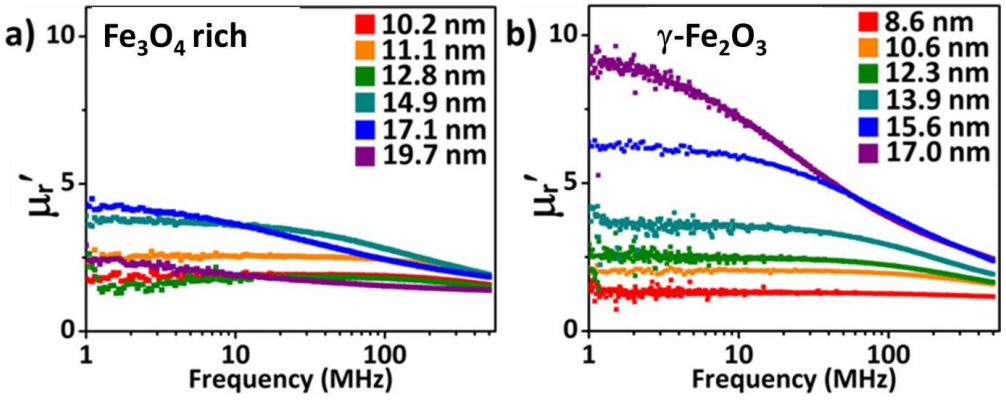

Figure 2.13. The μ_r' of a) magnetite-rich iron oxide NCs and b) maghemite iron oxide NCs.

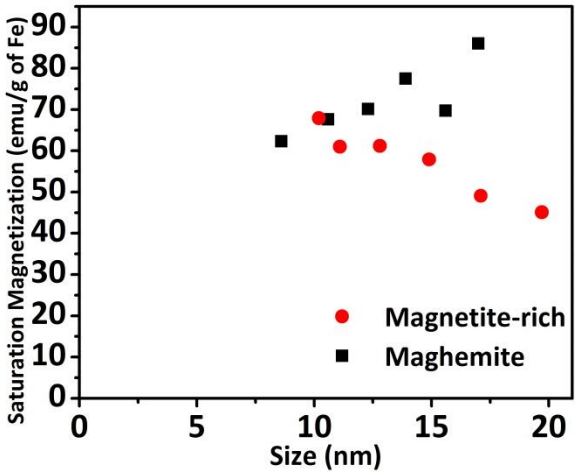

Figure 2.14. The M_s value of magnetite-rich (red circle) and maghemite (black square) iron oxide NCs at 300 K.

Surprisingly, the μ_r' values of the magnetite-rich NCs are smaller than those of oxidized maghemite NCs. Even though in the bulk magnetite is known for having a higher M_s than maghemite,[39,93] the M_s value of the magnetite-rich NC samples is similar to or smaller than that of maghemite NCs with similar size. In addition, the M_s decreases as the particle size increases.(Figure 2.14) These observations may arise from the presence of paramagnetic wüstite and/or interfacial wüstite/magnetite phases in as-synthesized NCs, which would lower their saturation magnetization. For example, up to 14.9 nm magnetite-rich iron oxide NCs, μ_r' values of magnetite-rich NCs are at the similar level compared to that of maghemite NCs. However, the 17.1 nm and 19.7 nm magnetite-rich

samples do not show the μ_r' as high as that of 15.6 nm and 17.0 nm. Considering the advent of the stiff slopes at around 200 K in the ZFC curves of 17.1 nm and 19.7 nm NCs, paramagnetic wüstite phase might start affecting the crystal structure of magnetite-rich iron oxide NCs and lower the permeability. Alternatively, the presence of a thicker spin-disordered-shell on the surface of magnetite-rich particles, often referred to as magnetic "dead layer",[133] compared to maghemite NCs will also have a similar effect of lowering the magnetization, possibly below that for the maghemite NCs, as previously observed.[134] In addition, stronger interparticle interactions of an antiferromagnetic nature could also reduce M_S. All these effects may contribute to the experimental observation that the size effect is not clearly expressed in as-synthesized iron oxide NCs (Figure 2.13a).

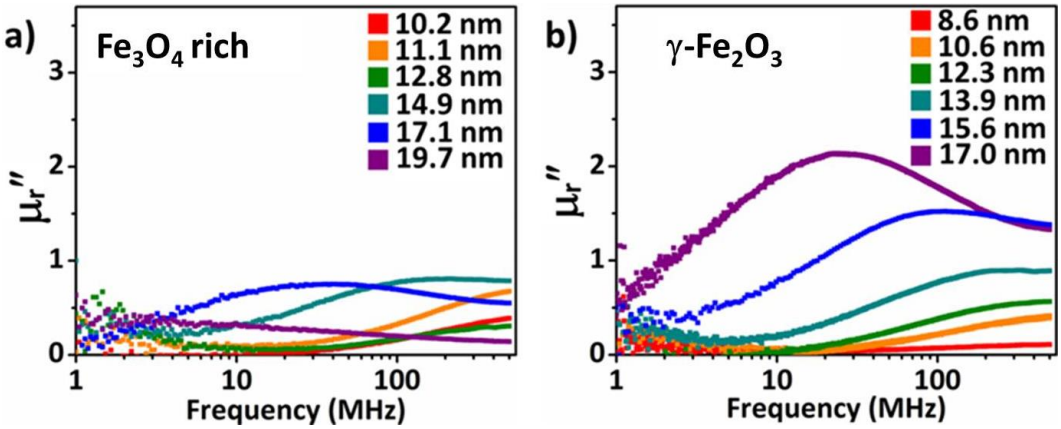

Figure 2.15. The μ_r" of a) magnetite-rich iron oxide NCs and b) maghemite iron oxide NCs.

We consider now the measurement of the μ_r". The μ_r" is the out-of-phase component of relative permeability, which is defined as $\mu_r'' = (B / H\mu_0)\sin\delta$.[93] This value is critical for low energy loss applications because energy loss is proportional to μ_r". The μ_r" of magnetite-rich (Figure 2.15a) and maghemite (Figure 2.15b) iron oxide NCs is presented in figure 2.15. As expected, the results show a maximum that is size dependent, with the size sensitivity being much more pronounced for the maghemite samples. In Figure 2.15 we observe the largest size maghemite NCs to have the most pronounced maximum at a frequency of about 30 MHz, with lower maxima monotonically decreasing in magnitude and displaced to higher frequencies as particle size decreases. In contrast, magnetite-rich NCs exhibit depressed maxima, not monotonically decreasing with size. These differences may be traced to the single particle magnetic anisotropies and the collective behavior of the NC assemblies and the way they affect their complex AC permeability. It should be noted that μ_r" of maghemite NCs is larger than that of magnetite-rich NCs. This is because μ_r" is proportional to μ_r' as can be seen from the following equation, $\mu_r'' = (B / H\mu_0)\sin\delta = \mu_r' \tan\delta$. Therefore, with the similar value of the phase delay, the μ_r" is higher in the case with the higher value of the μ_r'.

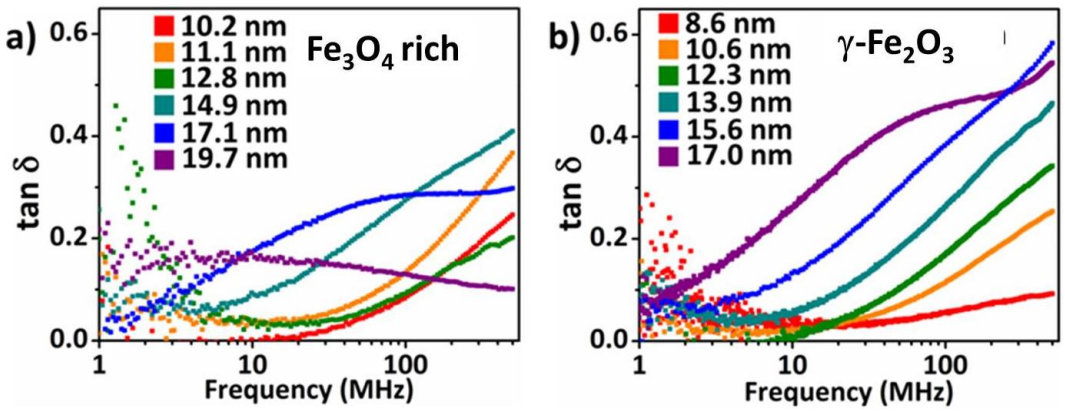

Figure 2.16. The loss tangent of a) magnetite-rich iron oxide NCs and b) maghemite iron oxide NCs.

Energy efficiency is expressed in terms of the loss tangent, *tanδ*, which is the ratio between the μ_r" and the μ_r' .[28] Materials characterized with low loss tangent are more energy efficient; they display a small phase delay between B and H. Here again, size dependence is not observed in the set of the magnetite-rich iron oxide NCs (Figure 2.16a), while it is clear in the case of the maghemite iron oxide NCs (Figure 2.16b). In the case of maghemite NCs, it is quite intriguing that the points where the loss tangent starts increasing significantly vary with the size of the NCs. This suggests that optimized magnetic materials for various kinds of electronic device applications, at different operating frequencies can be designed by tuning the size, shape, and chemical composition of magnetic NCs. For example, even though the 13.9 nm maghemite iron oxide NCs have a higher μ_r' than the 12.3 nm NCs over the whole range of the measured frequencies, it might be more energetically efficient to use 12.3 nm NCs as the inductor core for

devices operating at above 10 MHz, as the loss tangent of the 13.9 nm particles is much higher than that of the 12.3 nm particles at 10 MHz. Therefore, the systems with magnetic materials working in different frequency ranges can perform in an optimized condition by selecting NCs with the best performance at a particular operating frequency or over a specific range of frequencies. These results support the notion that magnetic NCs are promising candidates for low energy loss applications through precise control in the size, shape, and chemical compositions of NCs.

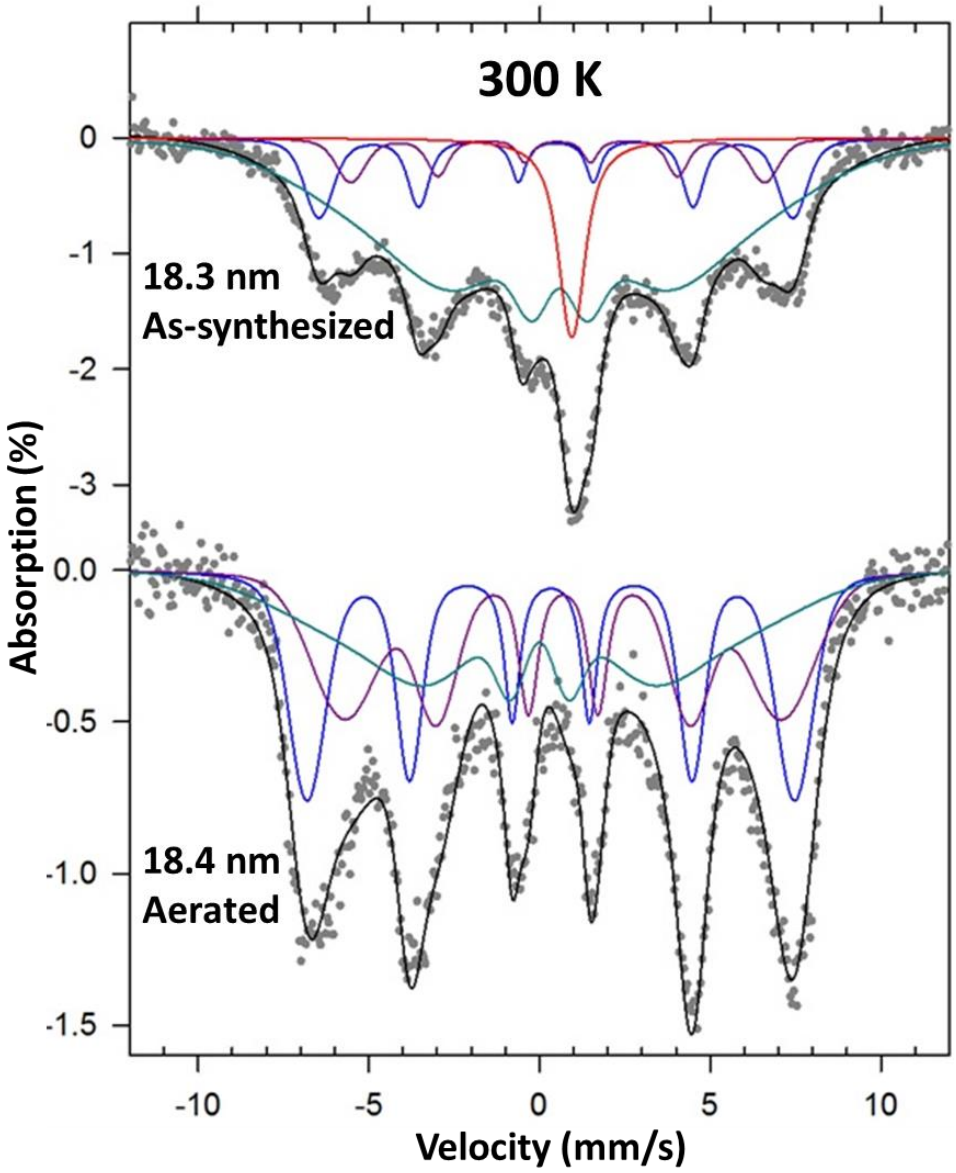

Figure 2.17. Mössbauer spectra of as-synthesized and aerated NC samples at 300 K as indicated. The experimental points are least square fitted (black line) to a superposition of theoretical spectra of tetrahedral Fe^{3+} (blue), octahedral $Fe^{2.5+}$ (purple) sites, interfacial $Fe_{1-x}O/Fe_3O_4$ (red) and IR (pale green) sites (Table 2.3).

Table 2.3. Mössbauer hyperfine parameters derived from spectral fits shown in Figure 2.17. δ, Isomer shift relative to metallic iron at room temperature, ΔE_Q, Quadrupole splitting, H_{hf}, Hyperfine magnetic field.

Sample	Size (by SAXS)	T (K)	Site	δ (mm/s)	ΔE_Q (mm/s)	H_{hf} (T)	Area (%)
As-synthesized Iron Oxide NCs	18.3 nm	300	Interfacial*	0.94	-	-	9.1
			Fe^{3+} (A)	0.47	-	42.9	13.7
			$Fe^{2.5+}$ [B]	0.53	-	27.5	7.6
			IR	0.58	-	-	69.6
After heating at 250 °C for 2 hours	18.4 nm	300	Fe^{3+} (A)	0.33	-	44.2	32.3
			$Fe^{2.5+}$ [B]	0.69	-	39.6	34.4
			IR	0	-	-	33.3

*$Fe_{1-x}O/Fe_3O_4$

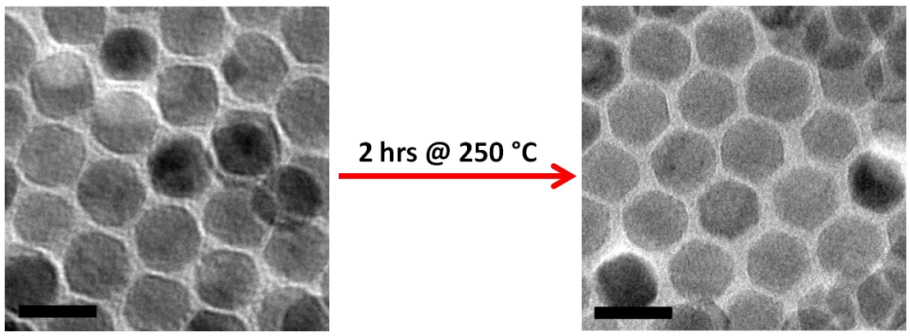

Figure 2.18. TEM images of 18.3 nm iron oxide NCs before (left) and after (right) oxidation process. These TEM images show that there is almost no change neither in morphology nor in size of NCs after oxidation process at 250 °C. The scale bar is 20 nm.

The composition dependence of the magnetic permeability of our NCs is further supported by the direct comparison of as-synthesized iron oxide NCs before and after the oxidation process at high temperature, as a comparison of the permeability properties of the sample before and after aeration indicates. As-synthesized iron oxide NCs 18.3 nm diameter are aerated at 250 °C for 2 hours following the literature.[135] The Mössbauer data of the aerated samples indicate that wüstite is oxidized, that is, the $Fe_{1-x}O$ or interfacial $Fe_{1-x}O/Fe_3O_4$ portion of the as-synthesized NCs is removed from the original NC structure (Figure 2.17 and Table 2.3). TEM images (Figure 2.18) show that there is no significant change in either the morphology or the size of NCs after the oxidation process. The superimposed SAXS curves of two samples also support that there is no change in size before and after the heating process. (Figure 2.19) Direct comparison reveals that after aeration the H_c at 15 K is reduced from ~216 mT to ~27 mT, which is a dramatic change (Figure 2.20b and 2.20c). At 300 K, the hysteresis curves show that iron oxide NCs are saturated much faster after oxidation (Figure 2.20a). Before the aeration process, as-synthesized iron oxide NCs reach to its 50 % of its maximum magnetization at around 275 mT, while the aerated iron oxide NC are excited 50 % at around 18 mT. In consequence, as shown in Figure 2.21, μ_r' of iron oxide NCs becomes more than 5 times larger at 1 MHz after oxidation even though the value spontaneously reduces from 11 at 1 MHz to 4 at 500 MHz. As the Mössbauer data indicate that the stoichiometry of

the NCs after aeration is more related to magnetite rather than maghemite without a wüstite phase, it supports our previous discussion that the inhomogeneous crystal structure of larger as-synthesized NCs due to paramagnetic wüstite phase leads to the lower magnetic permeability of as-synthesized iron oxide NCs than aged, maghemite iron oxide NCs as discussed earlier. However, why the aerated sample shows less H_c than aged, maghemite iron oxide NCs is an observation not fully understood and still under investigation.

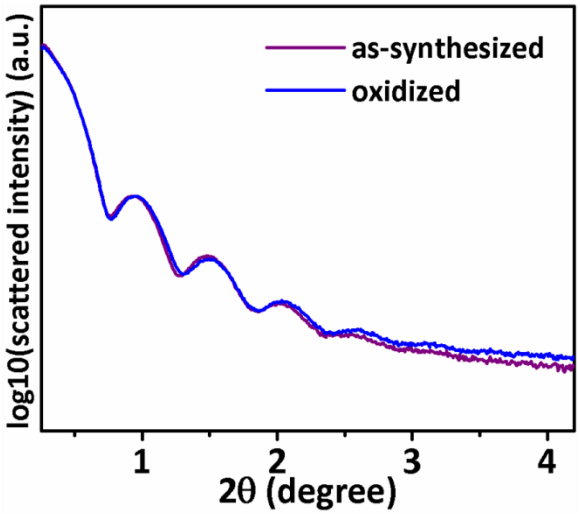

Figure 2.19. SAXS curves of as-synthesized iron oxide NCs (purple) and iron oxide NCs (blue) which are aged at 250 °C for 2 hours.

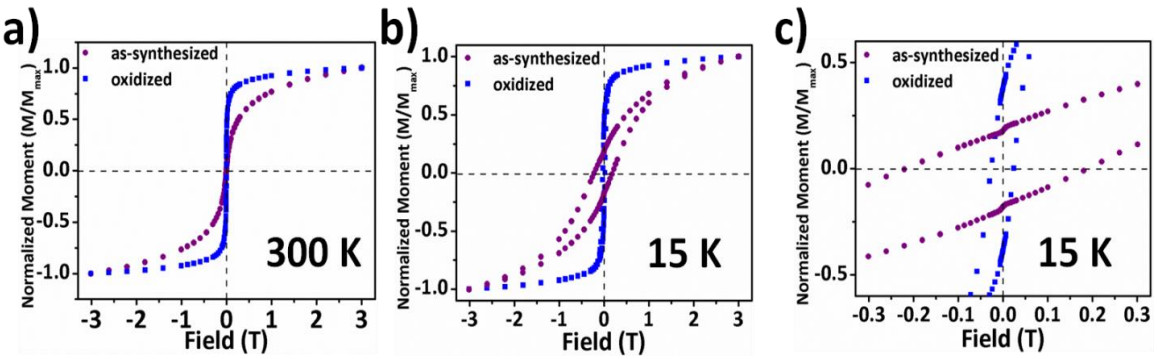

Figure 2.20. Magnetic hysteresis curves of 18.3 nm iron oxide NCs before and after aeration process. a) 300 K hysteresis curves, b) 15 K hysteresis curves, and c) zoomed up 15 K hysteresis curves from 0.3 T to -0.3 T of as-synthesized 18.3 nm iron oxide NCs (purple) and oxidized iron oxide NCs (blue).

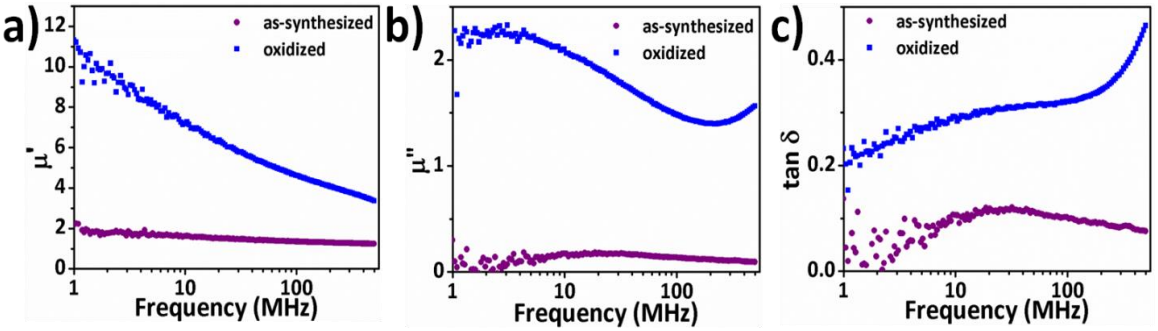

Figure 2.21. a) The μ_r', b) The μ_r", and c) Tangent loss of as-synthesized 18.3 nm iron oxide NCs (purple) and oxidized iron oxide NCs (blue).

In order to examine the potential of using iron oxide NCs as the magnetic core of a toroidal inductor, the maghemite NCs are further processed to form a

toroidal shape as shown in Figure 2.22. In previous reports, various kinds of polymers are used to prevent the oxidation of nanoparticles, to fix nanoparticles in a membrane, and to increase the resistance of the core.[136–139] However, the addition of polymer composites in the matrix can lower the μ_r' and filling factor of nanoparticles, which is not desirable for an inductor core. In our study, ligand exchange is adopted to make magnetic NC inductor cores. Ligand exchange with nitrosonium tetrafluoroborate ($NOBF_4$) is conducted to remove organic ligand layer and replace with inorganic BF^{4-} anions.[140] After ligand exchange, the NCs in dimethylformamide are precipitated by adding acetone and then dried under vacuum. After several hours, dry NC powder is obtained and this powder is ground by mortar and pestle to get a fine powder.

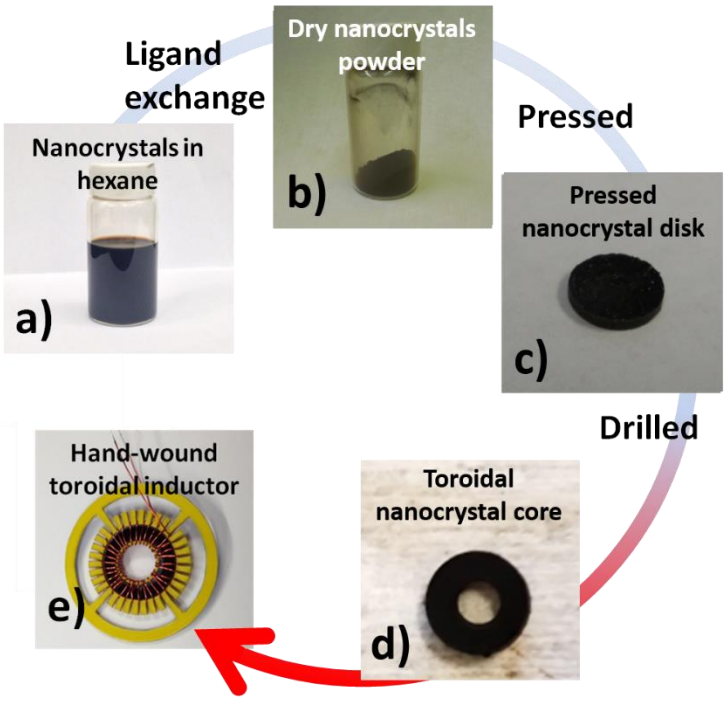

Figure 2.22. The steps to make hand-wound toroidal inductors with iron oxide NC cores. a) NCs are dispersed in hexane. b) NCs are ligand exchanged with $NOBF^{4-}$ and dried under vacuum overnight to achieve a NC powder. c) Nanoparticle powder is pressed into a disk. d) The center of the disk is drilled to make a toroidal core. e) The toroidal NC core is wound with a copper wire overcoated with polyurethane coated nylon.

Table 2.4. The dimensions of iron oxide NC cores.

	13.9 nm γ-Fe_2O_3 nanocrystal core	17.0 nm γ-Fe_2O_3 nanocrystal core
Outer diameter	6.5 mm	6.5 mm
Inner diameter	3.5 mm	2 mm
Thickness	680 mm	1200 mm
Calculated inductance of air-core indcutor	91.7 nH	113.2 nH

The fine powder is transferred into a cylindrical mold (a cylinder diameter of 6.3 mm) and pressed into a thin disk (Bench top hydraulic press, Carver, Inc.) with a pressure of 70 MPa. The disk is then dip-coated with SU-8 polymer to enhance physical stability and followed by drilling the center hole of approximately 3 mm. Note that the SU-8 does not include any solvent or photoinitiator and is initially in the form of a pellet which is subsequently melted on a hotplate at 100 °C for the dip-coating process. The dip-coated SU-8 layer is then removed with acetone so a magnetic NC toroidal core is obtained. The winding process for toroid inductor is then processed. The toroidal core is first integrated with a laser cut plastic bobbin to guide the winding path and a magnet wire is uniformly hand-wound. Two different NC sizes of maghemite powders (a particle size of 13.9 nm and 17.0 nm) have been fabricated as toroidal inductors using the described process. The dimensions of each NC core inductor are summarized in Table 2.4. The toroidal inductors are electrically characterized in terms of inductance, resistance, and quality factor as a function of frequency as shown in Figure 2.23.

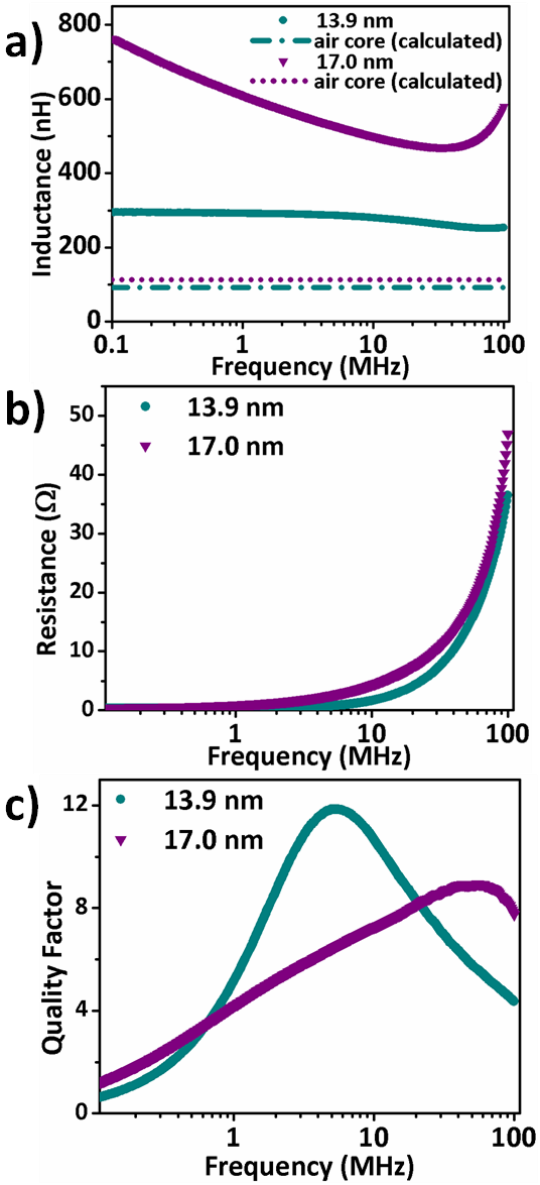

Figure 2.23. a) Inductance, b) resistance, and c) quality factor of 13.9 nm (cyan) and 17.0 nm (purple) maghemite iron oxide NC core. The frequency range is from 100 kHz to 100 MHz. The dotted lines in a) indicate the calculated inductance of air-core inductor.

A stable inductance of approximately 300 nH for 13.9 nm powder inductor is observed over the frequency range of 0.1 to 100 MHz whereas the inductance of 17.0 nm powder inductor decreased from approximately 750 nH at 0.1 MHz to 500 nH at 40 MHz. as shown in Figure 2.23a. The AC resistances and quality factors over the same frequency range are also shown in Figure 2.23b and c. The 13.9 nm inductor and the 17.0 nm inductor show resistances at 10 MHz of approximately 1.5 Ω and 4 Ω, and quality factor of 12 at 4.5 MHz and 9 at 40 MHz respectively. As can be expected from the trend in the relative permeability data, the inductor with the 17.0 nm iron oxide NC core enhances inductance more than the inductor with 13.9 nm iron oxide NC core because the inductance is proportional to the μ_r' of the magnetic core. Even though the inductance of the 17.0 nm sample decreases from 100 kHz to 35 MHz, the inductance of the 13.9 nm sample is stable over the whole range of frequencies (100 kHz to 100 MHz). The counterpart, the resistance of the inductor, increases in both cases, with a significant increase at 10 MHz for the 13.9 nm iron oxide NC core. In the case of the quality factor, the inductors hit their peak at 5.2 MHz for 13.9 nm iron oxide with 11.9 and 54.6 MHz for 17.0 nm with 8.95. It is notable that they do not show exactly the same pattern as the quality factor measured through the one-turn inductor model. This inconsistency in the quality factor trend from the data taken by one-turn inductor model can be attributed to the effect of ligand exchange and the resonance of the inductor itself. Ligand exchange shrinks inter-particle

distances.[103] Reduced inter-particle distance increases magnetic coupling between NCs and can produce different AC magnetic behavior from NCs with organic ligand shells. Also, the inductance and resistance were taken from the whole system, not just the core, so that the trend of the curve can deviate from the curve calculated by the one-turn inductor model. Since the data are already corrected for the impedance of the inductor without a core (Z_{sm}) (Equation 2.2), the data curve might not exactly match with the data from the hand-wound inductor. The data presented in Figure 2.23 show that magnetic NCs can be used as inductor cores successfully without any help from other matrix to hold the NCs together. These inductor trials indicate that there is a high potential to develop low energy loss materials by controlling the size and composition of NCs.

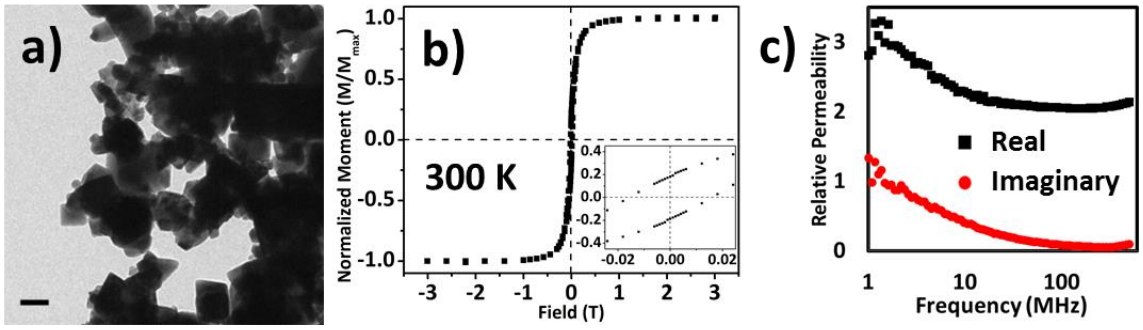

Figure 2.24. a) The TEM image, b) hysteresis curve at 300 K, and c) the relative magnetic permeability of commercially available iron oxide powder. The scale bar in the TEM image is 100 nm. The inset in b) is zoomed-up image of the hysteresis curve.

For comparison, commercially available ferromagnetic iron oxide powder was tested as well. As can be seen in Figure 2.24, this ferromagnetic iron oxide powder has a high μ_r'' even at relatively low frequency (1< *f* < 10 MHz) and low μ_r' at relatively high frequency (*f* > 10 MHz) range. In addition, our NCs are superior to the ferromagnetic iron oxide powder in that iron oxide NCs are dispersible in volatile solvent, which makes them readily available for solution based deposition processes.

2.6 Conclusion

In summary, we have characterized the AC magnetic properties of iron oxide NCs at radio frequencies from 1 MHz to 500 MHz. The compositions of as-synthesized and naturally oxidized iron oxide NCs are investigated by Mössbauer spectroscopy. The composition analysis confirms that as-synthesized iron oxide NCs are magnetite-rich and aged NCs are maghemite. In addition, a wüstite phase is also observed in the large, as-synthesized, iron oxide NCs. At room temperature ZFC curves and hysteresis curves show superparamagnetic behavior for both sets of iron oxide NCs. From the ZFC curves, the presence of magnetite and wüstite phase in the as-synthesized NCs is observed again. The measurements for the magnetic permeability show a clear size dependence in the maghemite NCs, but not in the magnetite-rich NCs. In maghemite iron oxide NCs, the μ_r' increases proportionally to the size of the NCs because the

magnetic moment of single domain NC is in proportion to the size. On the other hand, as-synthesized iron oxide NCs did not show size dependent magnetic permeability. This can be attributed to the inhomogeneous crystal structure of the as-synthesized NCs, which is observed from Mössbauer spectroscopy and SQUID measurements, making their magnetization smaller than what would be expected from a homogeneous magnetite phase. The aeration of the as-synthesized iron oxide NCs supports this argument. As-synthesized iron oxide NCs show no change in their morphology and size after heating at 250 °C for 2 hours. However, the paramagnetic wüstite phase disappears after the heating process according to the Mössbauer data analysis and their DC and AC magnetic properties are changed significantly. In particular, the μ_r' is increased dramatically to similar value of maghemite iron oxide NCs after heating, which supports our hypothesis. Finally, inductors with maghemite iron oxide NC cores are prepared to evaluate the feasibility of inductors with magnetic NC cores. 13.9 nm and 17.0 nm maghemite iron oxide NCs are prepared in powder form and toroidal core were prepared to be integrated into hand-wound inductors. The measurements on the inductors show clear NC-size dependence as presented in the permeability measurements. Even though the value of μ_r' is not at the same level as other traditional ferromagnetic materials such as Permalloy and Supermalloy, further investigation on low energy loss magnetic NCs should

continue to improve energy efficiency of magnetic components at radio frequencies in power electronic devices.

2.7 Experimental Section

2.7.1. Materials. All chemicals are used as purchased without any further purification. Iron (III) Chloride hexahydrate (97%), Oleic Acid (technical grade, 70 %), 1-Octadecene (technical grade, 90%), and iron oxide powder (< 5 m, 98 %) are purchased from Sigma Aldrich. Sodium Oleate (>97.0 %) is purchased from TCI America. Commercial ferrite toroidal cores are purchased from Amidon. Magnet wire (part No. 8055) is purchased from Belden.

2.7.2. The synthesis of iron oxide NCs and purification. Monodisperse iron oxide NCs are synthesized by modifying the method reported by Hyeon *et al.*[46] and Chen *et al*.[51] First, iron oleate precursors are prepared as following procedure. 10.8 g of iron (III) chloride, 36.5 g of sodium oleate, 40 mL of DI water, 40 mL of ethanol, and 80 mL of hexane are mixed into a 500 mL three-neck flask. The mixture is refluxed at 60 °C for 4 hours. The red-black colored iron oleate precursors are washed with DI water for 3 times and dried by using rotary evaporator. Then, the precursors are kept under vacuum for overnight. Second, the 10.2 nm iron oxide NCs are synthesized by adding 7.2 g of iron oleate precursors, 1 mL of oleic acid, and 20 mL of 1-octadecene into a three-neck flask.

The reaction mixture is heated to 100 °C and kept under vacuum for 1 hour. Then, the mixture is heated to 315 °C at a rate of 3 °C/min. After 30 mins, the reaction mixture is cooled down to room temperature and precipitated by adding ethanol. The precipitation is re-dispersed in hexane and washed with ethanol twice more. Finally, the iron oxide NCs are re-dispersed in hexane and kept in a glove box. By increasing the amount of oleic acid added into the mixture, the size of iron oxide NCs is increased. Aged NCs are kept in ambient conditions over a year.

2.7.3. The oxidation of as-synthesized iron oxide NCs. As-synthesized iron oxide NCs after purification are dissolved into the mixture of 20 mL of 1-octadecene and 1 mL of oleic acid. Then, the solution is heated to 250 °C. After 2 hours, the solution is cooled down to room temperature and re-purified by adding ethanol and centrifugation. The final product is re-dispersed in hexane and kept in a glove box.

2.7.4. Mössbauer Spectroscopy. Mössbauer measurements were performed by using a transmission Mössbauer spectrometer. A 30 mCi ^{57}Co radioactive source was used was maintained at RT. The source was mounted on an SEE Co (Medina, Minnesota) electromechanical drive, operated at constant acceleration. The samples were dispersed in BN and mounted into a Janis Research

cryogenic dewar. Sample temperatures 4.2 < T < 300 K were maintained by using a SEE Co temperature controller. Spectra were fit to a superposition of iron subsites assuming Lorentzian absorption lines and allowing for distributions of hyperfine fields using the WMOSS software package, also by SEE Co.

2.7.5. DC magnetization measurements. DC magnetic characterizations are performed by using superconducting quantum interference device (SQUID) magnetometer with reciprocating sample option (Quantum Design MPMS-XL 7T). For the zero field cooled (ZFC) curves, the samples are cooled down to 15 K first without an external field. Then, the magnetization of samples are taken under an applied field of 0.01 T from 15 K to 300 K. For the field cooled (FC) curves, the samples are cooled down to 15 K in the presence of 0.01 T magnetic field first, and then the magnetization is measured under an applied field of 0.01 T from 15 K to 300 K. The magnetization hysteresis curves are taken from 3 T to -3 T at 300 K and 15 K.

2.7.6. AC characterization. Relative magnetic permeability of iron oxide NCs is measured by using 4395A Agilent Network Anaylzer and 16454A Agilent Magnetic Material Test Fixture. Iron oxide NCs are dispersed in a mixture of hexane and octane (2:8) and deposited into a toroidal shaped sample holder (8 mm of outer diameter, 3.2 mm of inner diameter, 3 mm of height, and 2.5 mm of

depth). After filling the sample holder with dry iron oxide NCs, the sample is placed into the test fixture. The sweep frequency is set to from 1 MHz to 500 MHz in log frequency. The reactance and resistance of test fixture with the sample holder are measured and converted into the μ_r' and μ_r'' by using equation 2 and 3. The inductance and resistance of inductor with iron oxide NC core are collected using 43961A RF Impedance Test Kit. After connecting the test kit to the 4395A Agilent Network Analyzer, hand wound iron oxide core inductor is connected to the impedance test kit and the inductance and resistance are collected. The sweep frequency is set to from 0.1 MHz to 100 MHz.

2.7.7. Morphological and Structural Characterization. TEM images are collected using a JEM-1400 microscope and JEOL-2100 microscope at the Singh Center for Nanotechonology in University of Pennsylvania. WAXS data are collected using a Rigaku Smartlab high-resolution diffractometer with Cu Kα radiation (λ=1.5416 Å). Small-angle X-ray scattering data are taken at the Multi-Angle X-ray Scattering Facility at the University of Pennsylvania. Small-angle X-ray scattering data are analyzed using Datasqueeze software.

2.7.8. Preparation of toroidal inductor with NC core. A hand-wound inductor with NC core is prepared by following a reported method.[26] First, iron oxide NCs

in hexanes are ligand exchanged by $NOBF_4$ in dimethylformamide.[140] After the ligand exchange, NCs are washed by hexane and toluene to remove any leftover organic ligand. Then, the NCs are dried under vacuum overnight. This procedure results in dry NC powder. The fine powder is transferred to a cylindrical mold (6.3 mm of diameter) and pressed into a thin pellet (~1 mm of thickness) under 70 MPa of pressure. The pellet is dip-coated with SU-8 polymer to increase its physical stability followed by drilling a center hole. Then, the dip-coated SU-8 layer is removed by acetone and wound with a magnet wire coated with polyurethane-coated nylon.

CHAPTER 3. Size and Composition Dependent Magnetic Permeability of Ferrite ($M_xFe_{3-x}O_4$, M = Zn, Mn, Co) Nanocrystals at Radio Frequencies. (Chapter 3.5. collaborated with Dr. Jungkwun Kim and Chapter 3.7 collaborated with Dichen Li)

3.1 Introduction

The magnetic properties of ferrite NCs are very sensitive to the metal elements added, varying from soft magnets (such as zinc and manganese ferrite) with low magnetocrystalline anisotropy (e.g. $MnFe_2O_4$: - 0.3 x 10^5 erg/cm^3)[93], to hard magnets (such as cobalt ferrite) with high magnetocrystalline anisotropy and H_c (e.g. $CoFe_2O_4$: 20 x 10^5 erg/cm^3).[93] The distinct responses of soft and hard spinel ferrite NCs to AC magnetic fields are the bases for two different application areas: electromagnetic devices and thermoablation. For the application of magnetic core materials in electronic devices, soft magnetic materials with high magnetic permeability and low power loss at high operation frequencies are needed.[68,141,142] Conversely, for RF thermoablation, such as cancer treatment and drug delivery, hard magnetic materials with high energy dissipation efficiency under AC magnetic field are desired.[143–145]

The concentration of substitutional cations within the spinel ferrite NCs has a significant effect on their magnetic properties.[146–149] In the case of zinc ferrite ($Zn_xFe_{3-x}O_4$) and manganese ferrite ($Mn_xFe_{3-x}O_4$), as Zn^{2+} and Mn^{2+} has no net orbital angular momentum, the spin-orbit coupling effect is absent, resulting in very low magnetocrystalline anisotropy.[28] For cobalt ferrite ($Co_xFe_{3-x}O_4$), in contrast, the magnetocrystalline anisotropy is very sensitive to the doping level of Co^{2+} with larger amounts of Co^{2+} resulting in higher magnetic anisotropy and H_c.[146,147] This is due to the spin-orbit coupling effect on the electrons of Co^{2+}, originating from their strong orbital angular momentum.[146,147,150] It has been established that the magnetic properties of ferrite NCs are strongly affected by their shapes[30,151,152] and sizes.[11,30,152–155] To study the effect of M:Fe ratio (M=Zn, Mn, and Co) on the AC magnetic properties of spinel ferrite, it is important to control the average size, shape, and monodispersity of NCs precisely. This brings a significant challenge to the synthesis of ferrite NCs with precise control over size, shape while varying the chemical compositions.

In this chapter, the size and composition dependent magnetic permeability of nonstoichiometric $M_xFe_{3-x}O_4$ (M = Zn, Mn, and Co) NCs in radio frequencies are investigated. In the first part of this chapter (Chapter 3.1 – 3.6), I focus on the superparamagnetic spherical $Zn_xFe_{3-x}O_4$ ($0 \leq x \leq 0.25$) NCs with precisely controlled sizes, compositions, and narrow size distribution (< 7 % by TEM images) for solution based deposition into the microfabricated inductors. Colloidal

NCs are dispersed in non-polar solvents such as hexane and toluene, which enables cheap large-area deposition through low temperature solution based processes.[156–158] These superparagmagnetic NCs are further analyzed by a one-turn inductor model for AC magnetic characterization from 1 MHz to 100 MHz. Microfabricated inductors with zinc ferrite NC cores are prepared *via* a simple drop-casting process and their inductances, resistances, and quality factors are measured. Finally, the control of interparticle interaction *via* ligand exchange with dendrimers is discussed.

In the last section of the chapter (Chapter 3.7), I discuss the synthesis, size selective precipitation, and systematic DC and AC magnetic properties characterizations of $Mn_xFe_{3-x}O_4$ (x=0.11-0.49) and $Co_xFe_{3-x}O_4$ (x=0.06-0.55) NCs, as model systems for soft and hard magnetic ferrites. Manganese and cobalt ferrite samples of similar average size (~ 6 nm in diameter) and shape were synthesized. In addition, size selective precipitation is used to further narrow the size distributions.

3.2 Synthesis of Zinc Ferrite NCs

Zinc ferrites are one of the most promising candidates because of their intrinsically high M_S (165 - 190 emu/g(Fe+Zn))[30] and low magnetocrystalline anisotropy energy (1-3 x 10^4 J/m^3).[30] In addition, the insulating layer of organic

ligands surrounding the NCs can suppress eddy currents which are significant sources of energy loss in conventional magnetic materials. Though there are studies that motivate the interest in the magnetic permeability of zinc ferrite NCs,[159–161] there has not been a systematic study which addresses both the control of size and composition. We use the insights gained to design AC devices based on zinc ferrite NCs operating at radio frequencies.

In addition to exploiting high performance magnetic materials, it is also important to build devices with optimized geometries to allow low energy loss at radio frequencies. With increasing demand for downsized electronic devices, microelectromechanical systems (MEMS) have been studied for miniaturizing inductors,[49,162,163] which are among the most widely used components in electrodevices such as power converters,[164,165] wireless chargers,[166–168] and inductive sensors[163,169]. It is important to design MEMS carefully to reduce the size of inductors while increasing the power density of the inductors. However, conventional inductor core materials have had limited success in miniaturized inductors due to large energy loss from hysteresis losse and eddy current losses in the magnetic materials at radio frequencies.[138,170,171]

Zinc ferrite NCs are synthesized through the high temperature solvothermal decomposition process by modifying a previously reported method.[34] Briefly stated, to prepare 12.3 nm $Zn_{0.25}Fe_{2.75}O_4$ NCs, 6 mmol of zinc (II) acetylacetonate, 12 mmol of iron (III) acetylacetonate, 100 mmol of oleic acid,

112 mmol of oleylamine are mixed in 72 mL of octadecene. The reaction mixture is heated to 110 °C under vacuum. After two hours, the temperature is increased to 300 °C at a rate of 15 °C/min and held for two hours. Then, the reaction vessel is allowed to cool to room temperature and zinc ferrite NCs are precipitated by adding a mixture of isopropanol and ethanol in 5 to 1 ratio. After removing the supernatant, the precipitate is readily dispersible in hexane and the NCs are further washed with isopropanol to get rid of any excess oleic acid and oleylamine. This reaction results in 12.3 nm $Zn_{0.25}Fe_{2.75}O_4$ NCs. The NC size can be decreased by reducing the heating rate to 12.5 C/min and 10 C/min to synthesize 10.1 nm and 8.3 nm $Zn_{0.25}Fe_{2.75}O_4$ NCs, respectively. To investigate the Zn^{2+} doping level dependence of magnetic permeability, iron oxide NCs and $Zn_{0.1}Fe_{2.9}O_4$ NCs are synthesized as well.

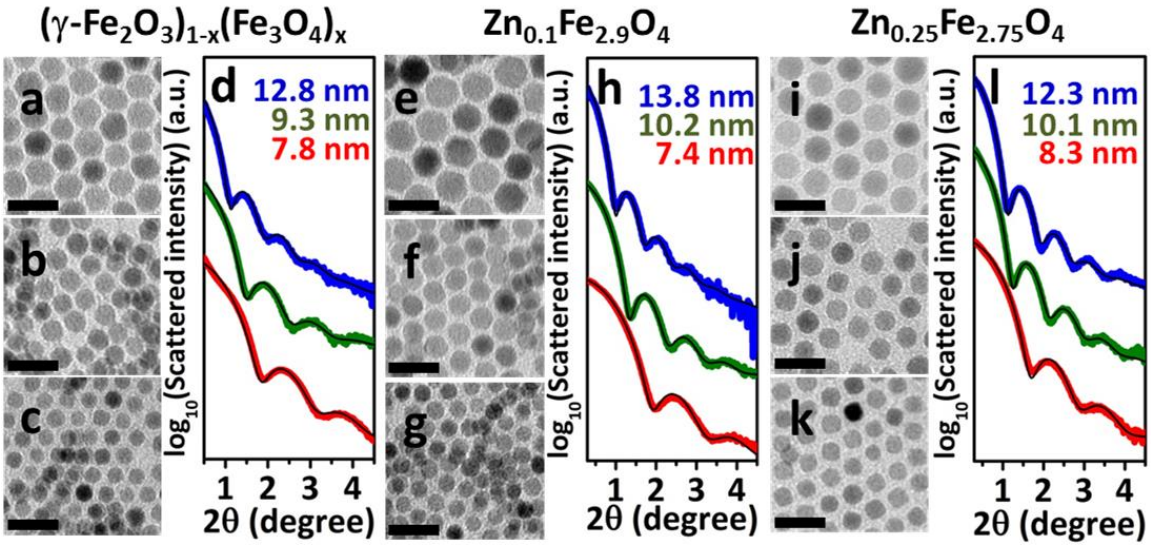

Figure 3.1. Transmission electron microscope (TEM) images of a) 12.8 nm, b) 9.3 nm, and c) 7.8 nm $(\gamma\text{-}Fe_2O_3)_{1-x}(Fe_3O_4)_x$ NCs and d) their SAXS data. The TEM images of e) 13.8 nm, f) 10.2 nm, and g) 7.4 nm $Zn_{0.1}Fe_{2.9}O_4$ NCs and h) their SAXS data. The TEM images of i) 12.3 nm, j) 10.1 nm, and k) 8.3 nm $Zn_{0.25}Fe_{2.75}O_4$ NCs and l) their SAXS data. The scale bars represent 20 nm.

In Figure 3.1, the transmission electron microscope (TEM) images of chemically synthesized ferrite NCs with various sizes and compositions are presented. Each size represents small, medium, and large NCs and each composition represents zero, small (0.03), and large (0.09) Zn to Fe ratio. The monodispersity of NCs is confirmed by SAXSand TEM images. The size distribution is narrow ranging from 7.3 % to 9.7 % by SAXS fitting simulation[101] and from 4.4 % to 6.9 % by TEM images (Table 3.1). It is worth noting that the size distribution improves as the Zn to Fe ratio increases. WAXS data (Figure 3.2)

confirms that all the samples possess spinel crystal structure (space group $Fd\bar{3}m$, No. 227). These structural analysis data indicate that the NCs are suitable subjects to study the size and Zn doping level dependence of the magnetic permeability of ferrite NCs. Note that as-synthesized iron oxide nanoparticles are a mixture of maghemite (γ-Fe_2O_3) and magnetite (Fe_3O_4) and tend to have more magnetite phase as their size increases.[3,26] These two phases share the same crystal structure (spinel) but maghemite contains only of Fe^{3+} whereas magnetite possesses both Fe^{2+} and Fe^{3+}. The exact analysis of the ratio between two different phases is out of the scope of this study and thus the "iron oxide NCs" indicate "$(\gamma\text{-}Fe_2O_3)_{1-x}(Fe_3O_4)_x$" throughout this study.[26]

Table 3.1. The average size of ferrite NCs measured by SAXS simulation and TEM images. The percentage numbers in the brackets indicate the size deviations.

	$(\gamma\text{-}Fe_2O_3)_{1-x}(Fe_3O_4)_x$		**$Zn_{0.1}Fe_{2.9}O_4$**		**$Zn_{0.25}Fe_{2.75}O_4$**	
	Size by SAXS	**Size by TEM**	**Size by SAXS**	**Size by TEM**	**Size by SAXS**	**Size by TEM**
Small	7.8 nm ($\pm$9.7 %)	6.1 nm ($\pm$6.9 %)	7.4 nm ($\pm$9.2 %)	6.3 nm ($\pm$6.6 %)	8.3 nm ($\pm$8.7 %)	7.3 nm ($\pm$5.8 %)
Medium	9.5 nm ($\pm$8.8 %)	7.7 nm ($\pm$6.3 %)	10.2 nm ($\pm$7.6 %)	8.5 nm ($\pm$5.6 %)	10.1 nm ($\pm$7.7 %)	8.5 nm ($\pm$4.4 %)
Large	12.8 nm ($\pm$8.6 %)	10.2 nm ($\pm$6.3 %)	13.8 nm ($\pm$8.0 %)	11.7 nm ($\pm$5.5 %)	12.3 nm ($\pm$7.5 %)	10.5 nm ($\pm$4.8 %)

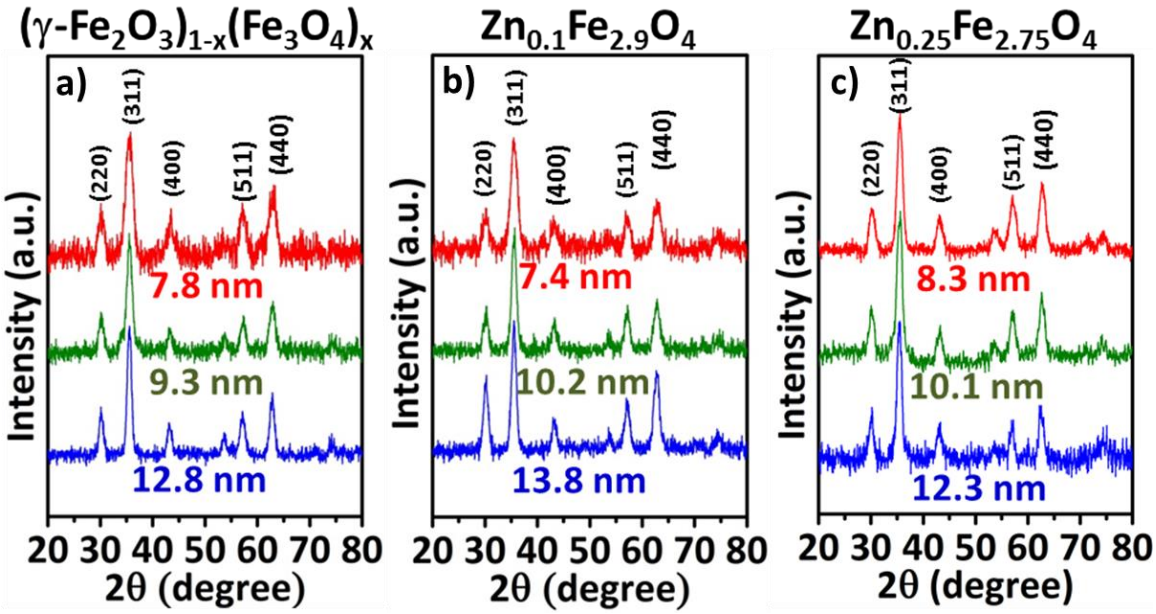

Figure 3.2. WAXS data of a) $(\gamma\text{-}Fe_2O_3)_{1-x}(Fe_3O_4)_x$ NCs, b) $Zn_{0.1}Fe_{2.9}O_4$ NCs, and c) $Zn_{0.25}Fe_{2.75}O_4$ NCs.

3.3 DC Magnetic Properties of Ferrite NCs

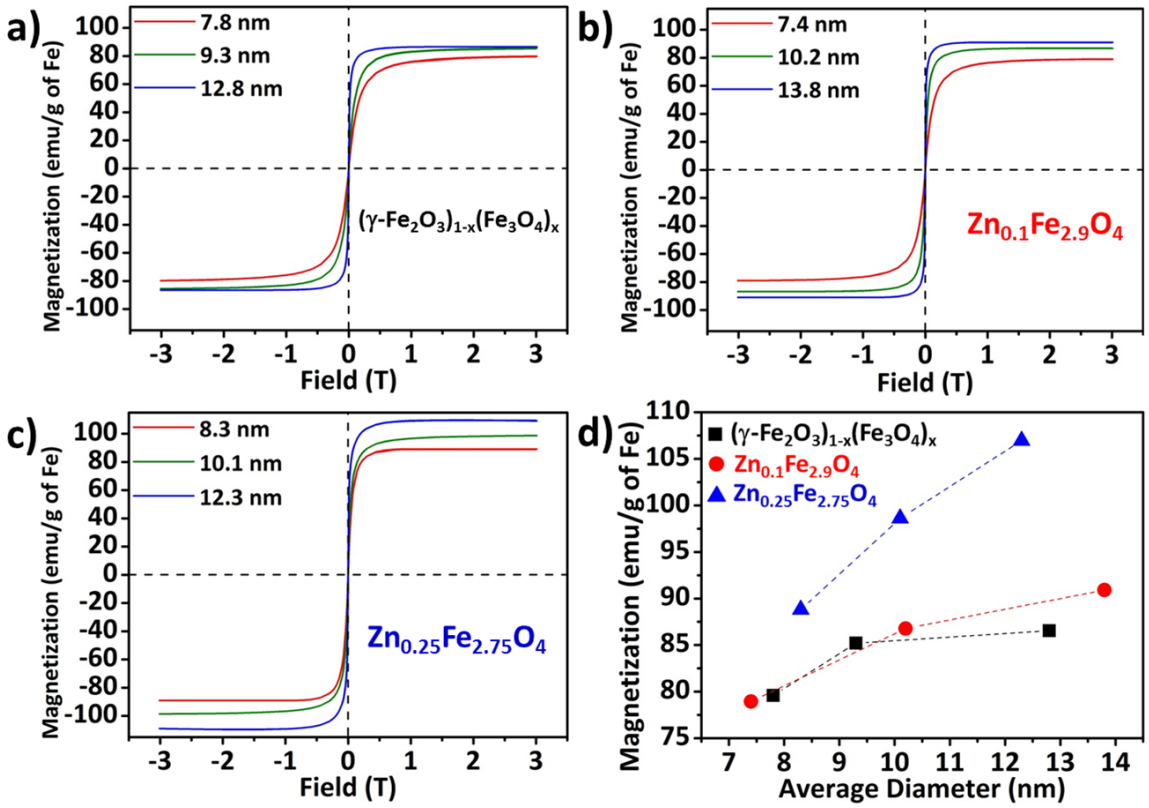

Figure 3.3. 300 K hysteresis curves of a) $(\gamma\text{-}Fe_2O_3)_{1-x}(Fe_3O_4)_x$ NCs, b) $Zn_{0.1}Fe_{2.9}O_4$ NCs, and c) $Zn_{0.25}Fe_{2.75}O_4$ NCs. d) M_s vs NC diameter curves of $(\gamma\text{-}Fe_2O_3)_{1-x}(Fe_3O_4)_x$ (black squares), $Zn_{0.1}Fe_{2.9}O_4$ (red circles), and $Zn_{0.25}Fe_{2.75}O_4$ (blue triangles) NCs.

The superparamagnetism of zinc ferrite NCs is observed in DC magnetic characterization with Superconducting Quantum Interference Device (SQUID) magnetometry. The hysteresis curves (Figure 3.3a, b, and c) at 300 K show zero H_c in all samples, which is the typical feature of superparamagnetism.[15] The M_s

increases with the size and zinc doping level of NCs as observed in Figure 3.3d and Table 3.2, which is consistent with the previously reported results.[26,131,159] For example, the M_s of 7.8 nm iron oxide NCs is 79.6 emu/g of Fe, while that of 12.3 nm $Zn_{0.25}Fe_{2.75}O_4$ is 107.0 emu/g of Fe. Zinc ferrite NCs possess a spinel structure (AB_2O_4) which is same as the structure of magnetite (Fe_3O_4) and maghemite (γ-Fe_2O_3). Zn^{2+} prefers to occupy tetrahedral A sites over octahedral B sites. As Zn^{2+} has no net orbital angular momentum, its replacement of Fe^{3+}, which also has quenched zero orbital angular momentum and takes A sites in iron oxide, does not significantly affect the magnetocrystalline anisotropy energy, so that the anisotropy energy of zinc ferrite is similar to that of maghemite.[172] This is reflected in the 15 K coercivities (H_c) (Figure 3.4 and Table 3.2); when the compositions are same, H_c increases with the size of the NCs, but there is no systematic correlation between the composition and H_c. In contrast, doping Zn^{2+} raises the M_s.[173] The magnetism of spinel structure materials is based on ferrimagnetism whose magnetic moment comes from the difference between the magnetic moment located at two B sites and one A site due to antiparallel alignment of spins in each site.[28] As Zn^{2+} has no unpaired electrons and it prefers to occupy the A site (normal spinel structure), Zn^{2+} doped iron oxide NCs possess higher M_s than magnetite or maghemite.[28,159] This explains why zinc ferrite NCs can be a good candidate for inductor cores due to the promise of low energy loss at radio frequencies. In Figure 3.3d, in general, the M_s increases with

the size and Zn doping level, but the difference in smallest samples is not as apparent as in larger sizes due to the higher surface to volume ratio of smaller NCs, which possess more disordered surface spins.[174]

Table 3.2. The summary of the H_c values of NCs at 15 K and the M_S values at 300 K.

$(\gamma\text{-}Fe_2O_3)_x(Fe_3O_4)_{1-x}$			$Zn_{0.1}Fe_{2.9}O_4$			$Zn_{0.25}Fe_{2.75}O_4$		
Size (nm)	H_c at 15 K (mT)	M_s at 300 K (emu/g of Fe)	Size (nm)	H_c at 15 K (mT)	M_s at 300 K (emu/g of Fe)	Size (nm)	H_c at 15 K (mT)	M_s at 300 K (emu/g of Fe)
7.8	4.6	79.6	7.4	5.2	78.9	8.3	6.7	88.8
9.3	9.8	85.2	10.2	10.6	86.8	10.1	8.7	98.6
12.8	8.8	86.5	13.8	11.6	90.9	12.3	10.9	107.0

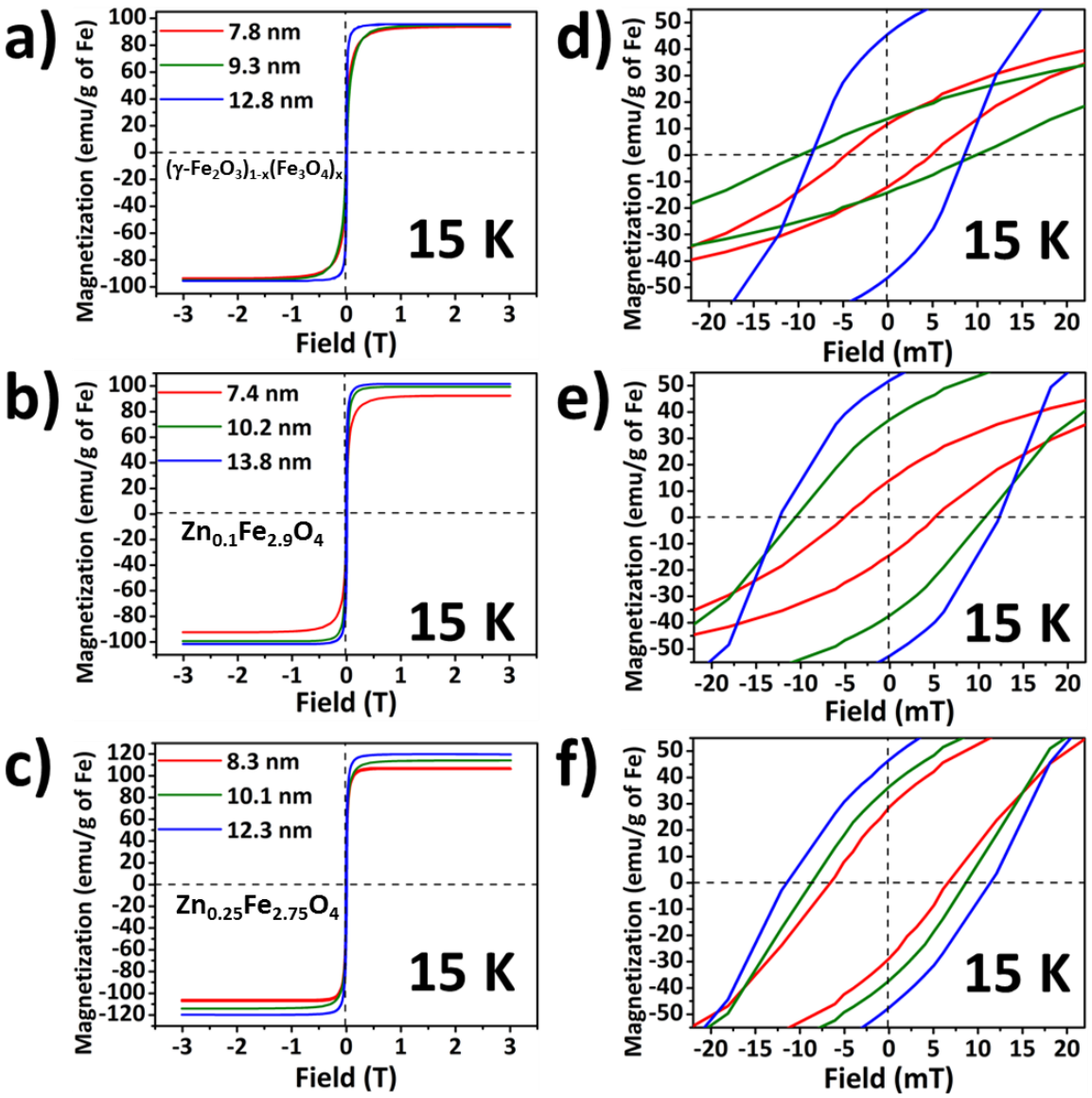

Figure 3.4. The hysteresis curves of a) $(\gamma\text{-}Fe_2O_3)_x(Fe_3O_4)_{1-x}$, b) $Zn_{0.1}Fe_{2.9}O_4$, and c) $Zn_{0.25}Fe_{2.75}O_4$ NCs at 15 K. The plots d), e), and f) are zoomed in plots of a), b), and c), respectively.

3.4 Size and Composition Dependent Magnetic Permeability of Zinc Ferrite NCs

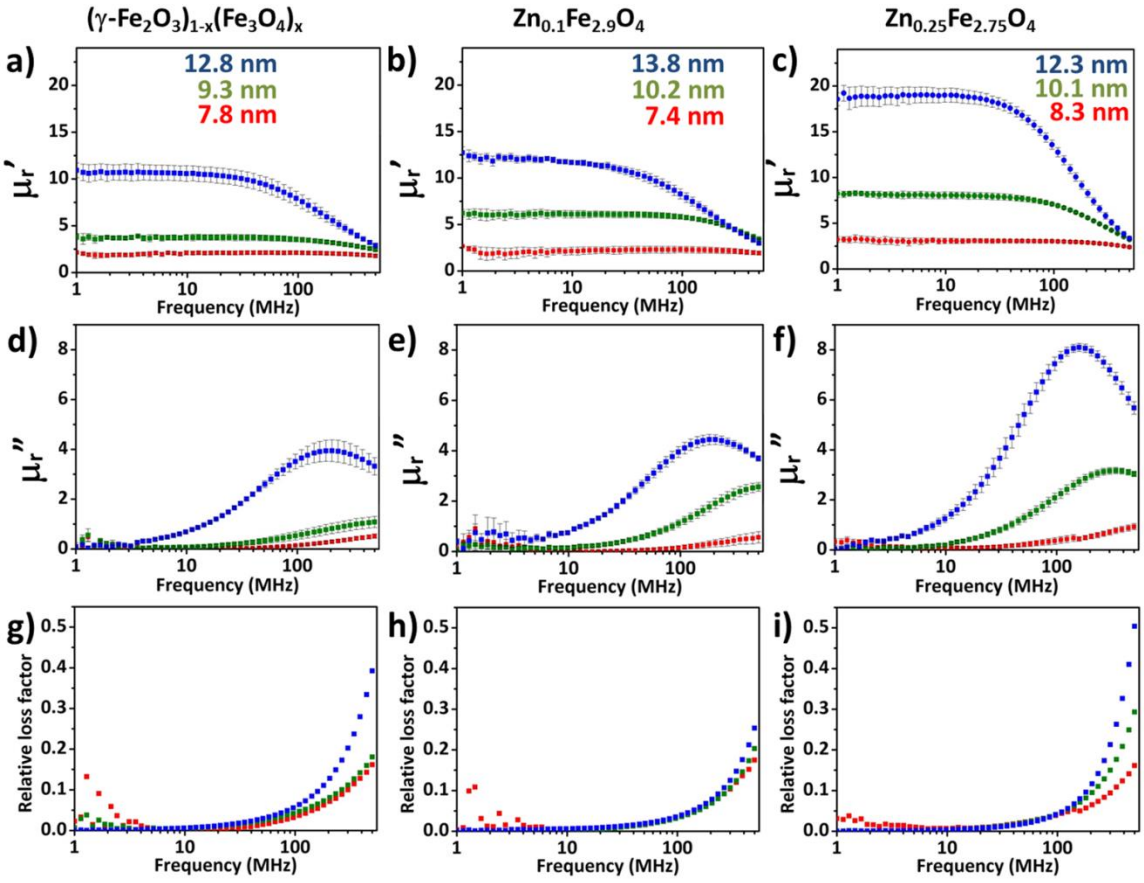

Figure 3.5. The μ_r' of a) $(\gamma\text{-}Fe_2O_3)_{1-x}(Fe_3O_4)_x$ NCs, b) $Zn_{0.1}Fe_{2.9}O_4$ NCs, and c) $Zn_{0.25}Fe_{2.75}O_4$. The μ_r" of d) $(\gamma\text{-}Fe_2O_3)_{1-x}(Fe_3O_4)_x$ NCs, e) $Zn_{0.1}Fe_{2.9}O_4$ NCs, and f) $Zn_{0.25}Fe_{2.75}O_4$. The relative loss factor ($tan\ \delta/\mu_r'$) of g) $(\gamma\text{-}Fe_2O_3)_{1-x}(Fe_3O_4)_x$, h) $Zn_{0.1}Fe_{2.9}O_4$ NCs, and i) $Zn_{0.25}Fe_{2.75}O_4$ NCs.

The AC magnetic characterization of zinc ferrite NCs is performed in a one-turn inductor model system[127] and summarized in Figure 3.5. In Figure 3.5a, b,

and c, the μ_r' curves of iron oxide, $Zn_{0.1}Fe_{2.9}O_4$, and $Zn_{0.25}Fe_{2.75}O_4$ are presented. This term is the in-phase value of the relative magnetic permeability and related to how much the material can increase the magnetic flux density in itself, that is the larger the μ_r', the higher the magnetic flux density.[93] The result shows that μ_r' increases as the NC size and Zn doping level increase. This can be attributed to the increased domain size and reduced surface area of larger NCs, which results in larger magnetic moments for each NC.(Figure 3.3d) However, it is worth noting that μ_r' is not linearly proportional to the M_s value. For example, while the M_s of 12.3 nm $Zn_{0.25}Fe_{2.75}O_4$ is 30 % larger than that of 12.8 nm iron oxide NCs, μ_r' is almost 60 % larger, which indicates the importance of the AC magnetic characterizations. Compared to the previously reported values of iron oxide NCs,[26,68] μ_r' of zinc ferrite NCs is much higher due to their higher magnetic moment relative to iron oxide NCs. μ_r' of 12.3 nm $Zn_{0.25}Fe_{2.75}O_4$ is stable at 18-19 MHz and up to about 20-30 MHz and this is not significantly different from the trend of similar size iron oxide NCs and $Zn_{0.1}Fe_{2.9}O_4$ NCs, as can be seen in a normalized curve (Figure 3.6a). Therefore, by increasing the doping level of Zn in iron oxide NCs one can increase the magnetic flux density without significantly sacrificing the operating frequency. This enhancement is possible because the Zn^{2+} has no net angular momentum which leads to low magnetocrystalline anisotropy of the system, as mentioned before. In the case of small NCs in the 7-8 nm range, μ_r' tends to increase as the amount of Zn

increases, but the difference is not as apparent as the difference seen between larger NCs with different Zn content due to the high surface to volume ratio. One thing should be noted is that μ_r' of iron oxide NCs is much higher than the previously reported values. In this study, μ_r' of 12.8 nm iron oxide NCs is about 11 at 1 MHz, while the similar size of NCs show 4-5 of μ_r' in our previous study.[26] Also, at 100 MHz, μ_r' of 9.3 nm iron oxide NCs show 3.5 of μ_r' in this study, but iron oxide NCs with similar size were reported to possess ~2 of μ_r'.[68] The reason for this difference is still under investigation.

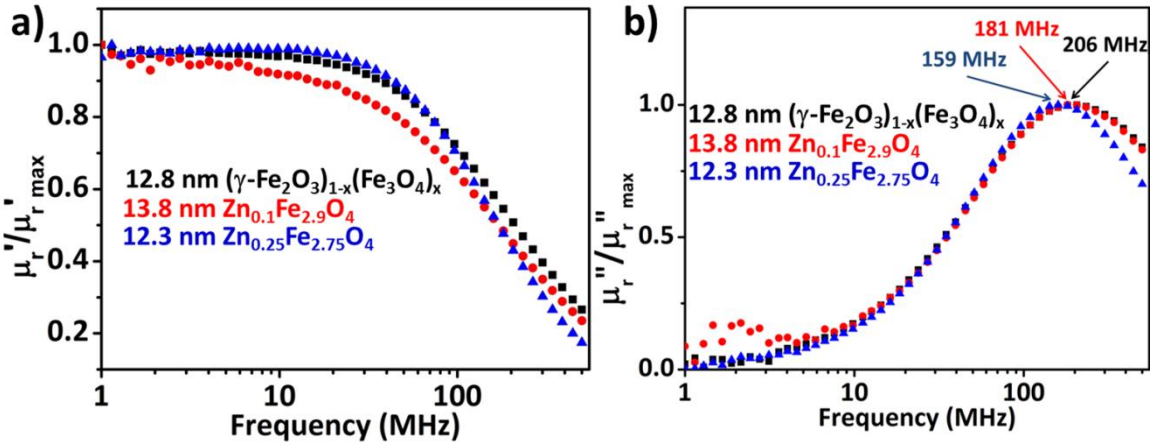

Figure 3.6. The normalized curves of a) the μ_r' and b) the μ_r". Black squares represent 12.8 nm iron oxide NCs, red circles represent 13.8 nm $Zn_{0.1}Fe_{2.9}O_4$ NCs, and blue triangles represent 12.3 nm $Zn_{0.25}Fe_{2.75}O_4$ NCs.

In Figure 3.5d, e, and f, the μ_r" of ferrite NCs is shown. This term is the out-of-phase value of magnetic permeability and related to the energy loss of magnetic materials, that is, the larger the μ_r", the greater the energy loss. In general, the data show that μ_r" increases as the size of NCs increases as expected. This is consistent with the result in Figure 3.5a-c. Since μ_r" can be written in terms of μ_r' *as* $\mu_r" = \mu_r' tan\delta$ where δ is the phase delay of magnetic moments of materials from an external field, a larger μ_r' results in a higher μ_r" if the phase delay, δ, is same in two different materials. Therefore, considering the result presented in Figure 3.5a, it is reasonable that μ_r" increases as the size of NCs increases. In particular, the maximum value of μ_r" of 12.3 nm $Zn_{0.25}Fe_{2.75}O_4$

NCs is almost double of that of 12.8 nm iron oxide NCs, which is consistent with the result from μ_r' data. The highest peak of μ_r'' can be interpreted as ferromagnetic resonance (FMR), which occurs when the precession frequency of magnetic spins around the anisotropy field in a ferromagnetic material concurs with the external alternating field frequency. The FMR frequency decreases as the size and the amount of Zn incorporated into the NCs increases, which can be explained by Snoek's limit.[175] For example, 12.3 nm $Zn_{0.25}Fe_{2.75}O_4$ has its maximum peak at 159 MHz while those of 13.8 nm $Zn_{0.1}Fe_{2.9}O_4$ and 12.8 nm iron oxide NCs are at 181 MHz and 206 MHz.(Figure 3.6b) This implies that the operable frequency range for zinc ferrite NCs is more limited than that for iron oxide NCs in the RF range. Even so, considering the fact that the current state of the art devices are operating at up to only a few hundred kHz,[87] our zinc ferrite NCs can be considered as an option for low magnetic loss material at radio frequencies.

The efficiency of magnetic materials under an AC magnetic field can be expressed as the relative loss factor (RLF), $\tan \delta/\mu_r'$. Magnetic energy loss occurs due to the lag of internal magnetic spin directions with respect to the external field direction.[176] Therefore, it is desirable to reduce the RLF as much as possible for low energy loss applications. In Figures 3.5g, h, and i, the RLFs of NCs with respect to frequency is presented. Surprisingly, the RLFs of NCs with different sizes are almost the same up to ~ 200 MHz. This suggests that zinc

ferrite NCs can increase the magnetic flux density of a system at high frequency without suffering from energy loss compared to iron oxide NCs. Also, as observed in Figure 3.7, it is notable that the RLF value is in the range between 10^{-4} and 10^{-2} up to 30 MHz for 12.3 nm $Zn_{0.25}Fe_{2.75}O_4$ NCs, which is lower than that of ferrites prepared by a conventional ceramic method. Also, compared to iron oxide NCs and $Zn_{0.1}Fe_{2.9}O_4$ NCs with a similar size to 12.3 nm $Zn_{0.25}Fe_{2.75}O_4$ NCs, the RLF value does not increase or change significantly, indicating that doping Zn^{2+} into the iron oxide NCs does not cause a decrease in efficiency. This implies the use of magnetic ferrite NCs as inductor core is a promising approach for low energy loss applications.

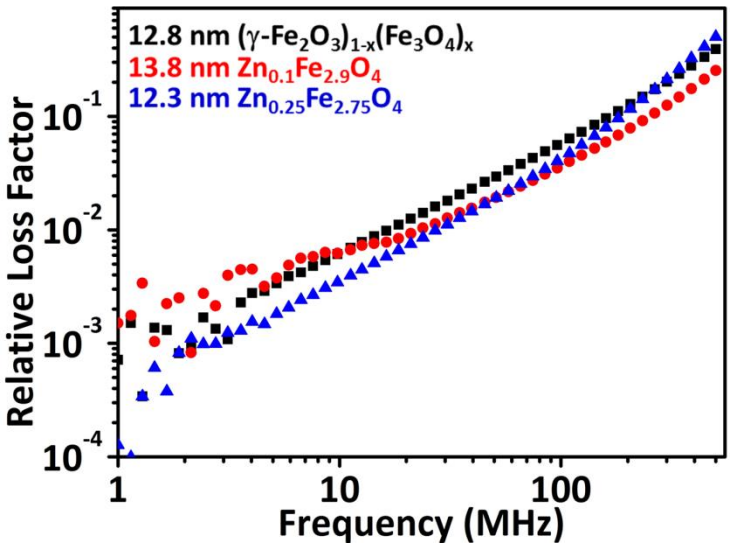

Figure 3.7. The relative loss factor of 12.8 nm iron oxide NCs (black squares), 13.8 nm $Zn_{0.1}Fe_{2.9}O_4$ NCs (red circles), and 12.3 nm $Zn_{0.25}Fe_{2.75}O_4$ NCs (blue triangles) from 1MHz to 500 MHz with y-axis in log scale.

3.5 Microfabricated Inductors with Ferrite NCs

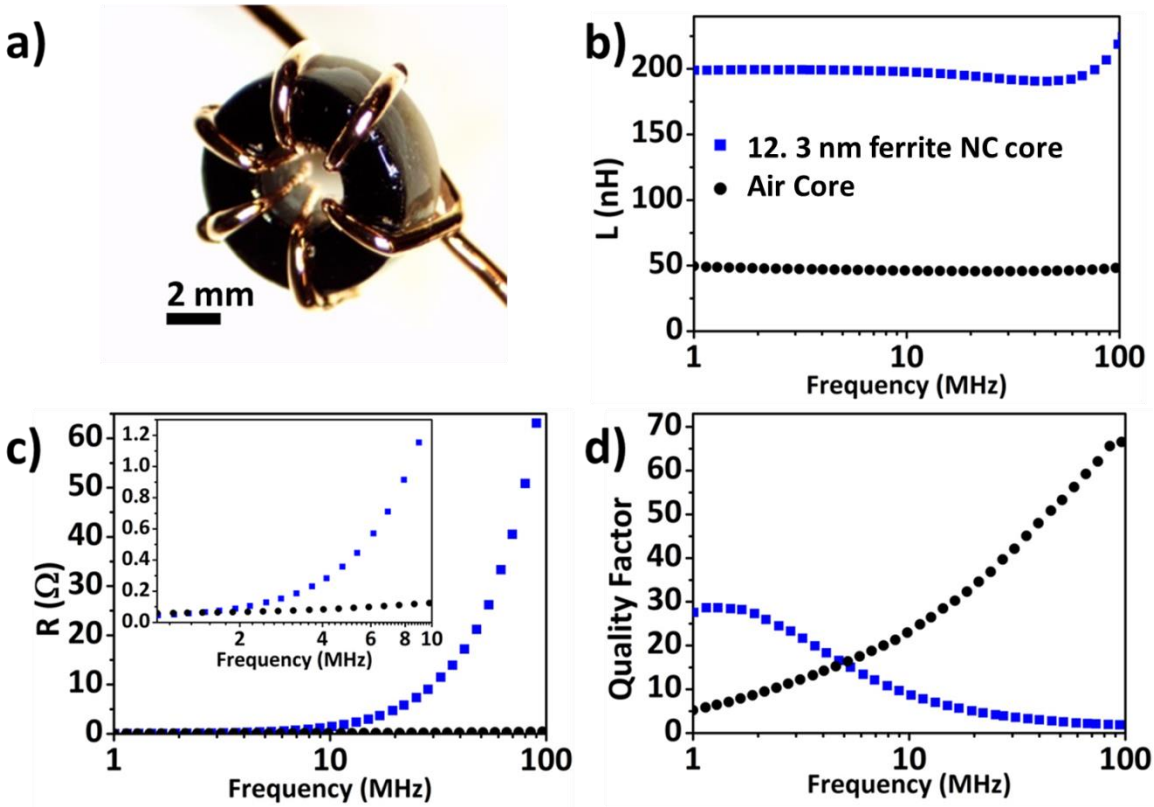

Figure 3.8. Toroidal inductor characterization: a) a photograph image of 6-turn toroidal inductor, b) inductance, c) resistance, and d) quality factor of the NC core toroidal inductor (blue square) and air core inductor with the same geometry (black circle). The inset in c) is the enlarged image of the resistance curve from 1 MHz to 10 MHz.

We have incorporated our NCs into microfabricated inductors through a drop casting process. Briefly, a toroidal sample holder (8 mm of outer diameter, 3.2 mm of inner diameter, 3 mm of height, and 2.5 mm of depth) prepared by machining is filled with 12.3 nm $Zn_{0.25}Fe_{2.75}O_4$ NCs and covered with an epoxy

shield. Then, a seed metal layer forming an inductor structure is wound around the sample holder and electroplated. Note that the proposed micromachining process is not limited by the toroid shape (Figure 3.8a). A solenoid inductor was also fabricated and characterized (Figure 3.9), which demonstrates the flexibility of the NCs as inductor cores. Figure 3.8a shows a photograph of the inductor with zinc ferrite NC core. The fabricated toroidal inductor is electrically characterized using an Agilent 4395A impedance analyzer in terms of inductance, resistance, and quality factor as a function of frequency and compared with an air-core inductor as shown in Figure 3.8. An average inductance of approximately 200 nH was measured in the frequency range of 1 to 100 MHz as shown in Figure 3.8b. In a 10-turn solenoid inductor with NC core, about 440-450 nH inductance is observed to be stable up to 40-50 MHz. At higher frequencies, a resonant behavior is shown in both geometries. The inductor resistance, shown in Figure 3.8c, measures approximately 0.05 Ω at 1 MHz and slowly increased as the frequency goes up. The quality factor is plotted in the frequency range of 1-100 MHz as shown in Figure 3.8d and compared with an air core inductor. The quality factors of the toroidal inductor and solenoid inductor with NC core are observed to be higher than those of air core inductors with the same geometries in the frequency ranges of 1-5 MHz and 1-9 MHz with the values over 15 and 20, respectively, in which most integrated power converters are operating. The quality factors reach to the maximum values of 28.6 at 1.3 MHz for the toroidal

inductor Figure 3.8d) and 44.2 at 1.7 MHz for the solenoid inductor (Figure 3.9d), indicating that the 12.3 nm $Zn_{0.25}Fe_{2.75}O_4$ NCs are energy efficient materials. In this measurement, the inductor permeability is rather low compared to that of the NCs due to the inductor winding geometry as well as the volume of the sample holder.

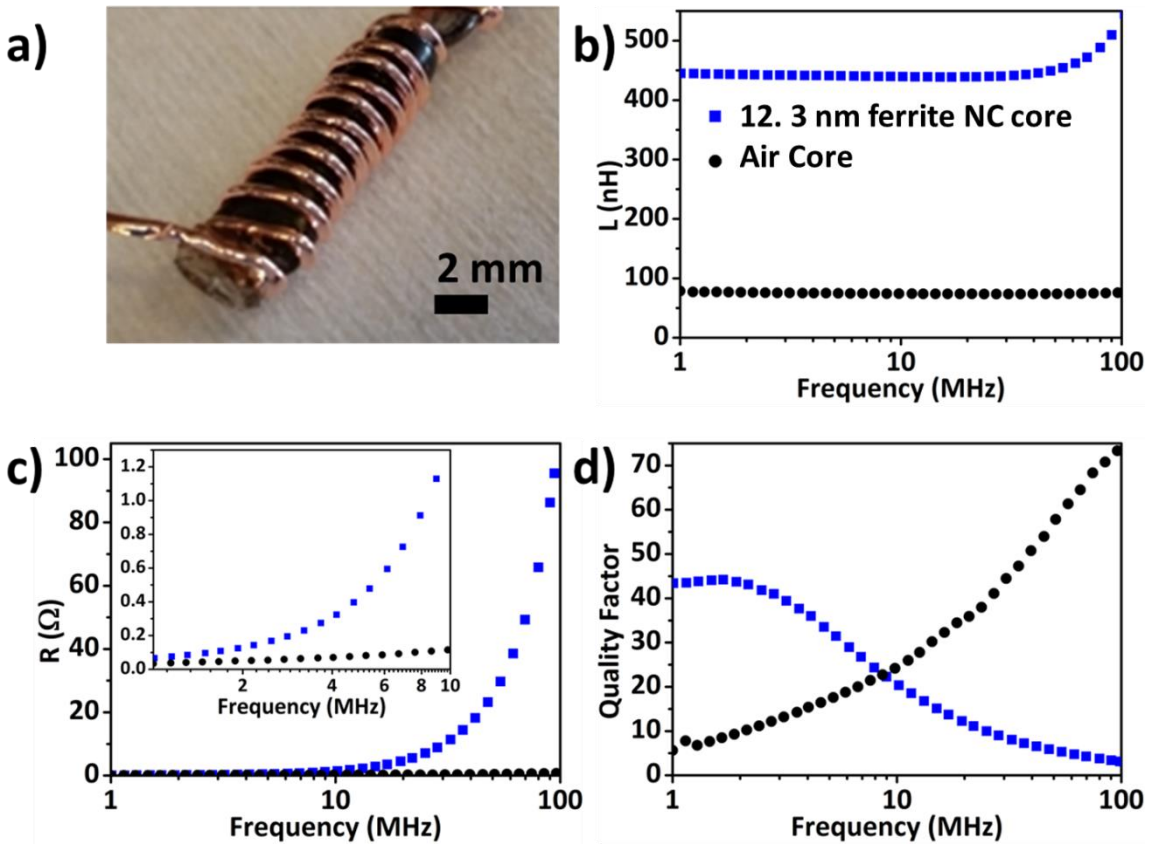

Figure 3.9. Solenoid inductor characterization: a) a photograph image of 10-turn solenoid inductor, b) inductance, c) resistance, and d) quality factor of the NC core solenoid inductor (blue square) and air core inductor with the same geometry (black circle).

3.6 Dendrimer Mediated Dipolar Interaction Control among NCs

As described in chapter 2, there is strong dipole-dipole interaction between magnetic NCs. These can be observed from the value of remnant magnetization ratio (M_r/Ms)[93] at under T_B or from the flattened FC curves.[113–115] Strong dipolar interactions between NCs lag the thermal relaxation of NC magnetic moments, leading to higher energy barrier for the thermal fluctuation of NCs.[177] Therefore, it is necessary to reduce the dipolar interaction to increase the operating frequencies of magnetic devices. Song *et al.* reported that the dipole-dipole interaction can be tuned by controlling the interparticle distance between Fe_3O_4 NCs using core-shell structure.[68] In their work, 8 nm SiO_2 shell on 9 nm Fe_3O_4 NCs keeps the NCs apart from each other so that the T_B is decreased from 86 K to 37 K, which is the apparent evidence of weakened dipolar interaction. However, this approach lowers the filling factor of NCs too much, sacrificing μ_r'. In this section, we discuss about controlling the magnetic permeability of $Mn_{0.08}Zn_{0.33}Fe_{2.59}O_4$ NCs *via* ligand exchange with dendrimers. Unlike the core-shell approach, the ligand exchange process is reversible and the NCs with dendrimers are still soluble in non-polar solvents, keeping its compatibility with solution based deposition processes.

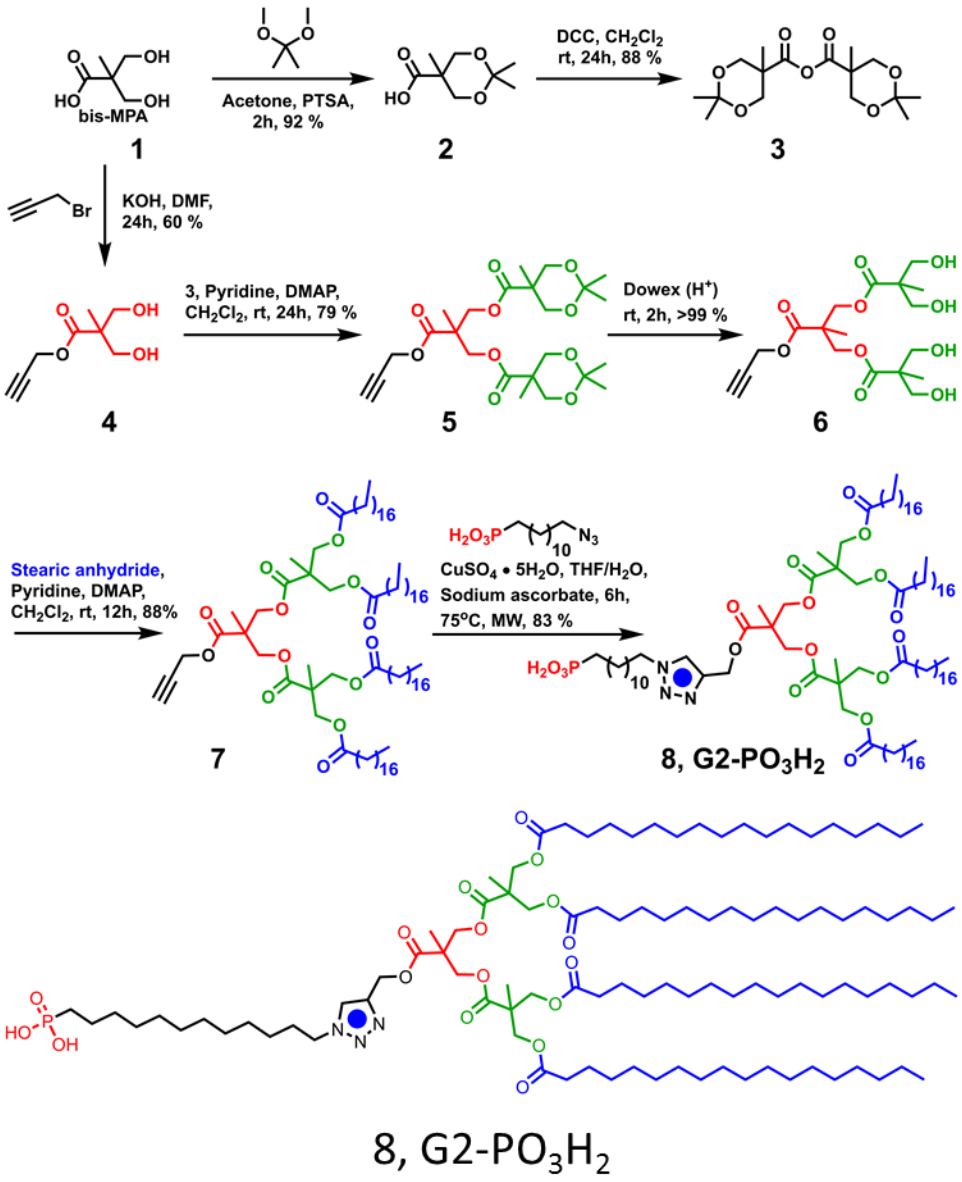

8, G2-PO_3H_2

Scheme 3.1. A scheme of the synthetic routes for the synthesis of G2-PO_3H_2 and the structure of G2-PO_3H_2.

The synthetic procedure of the dendrimer used in this study is shown in Scheme 3.1. The detailed procedure can be found in the experimental section.

The end G2 product can be used to prepare various types of end groups such as carboxylic acid, thiol, and phosphonic acid. Since as-synthesized NCs are covered by oleic acid, it might be hard to perform ligand exchange with a dendrimer with carboxyl group. We try to employ G2-SH dendrimer, but no significant difference is observed when the dendrimer is mixed with the NCs in hexane and kept for 24 hours at 40 °C with stirring. Under the same ligand exchange condition, G2-PO_3H_2 makes a clear difference in TEM images before and after the process.

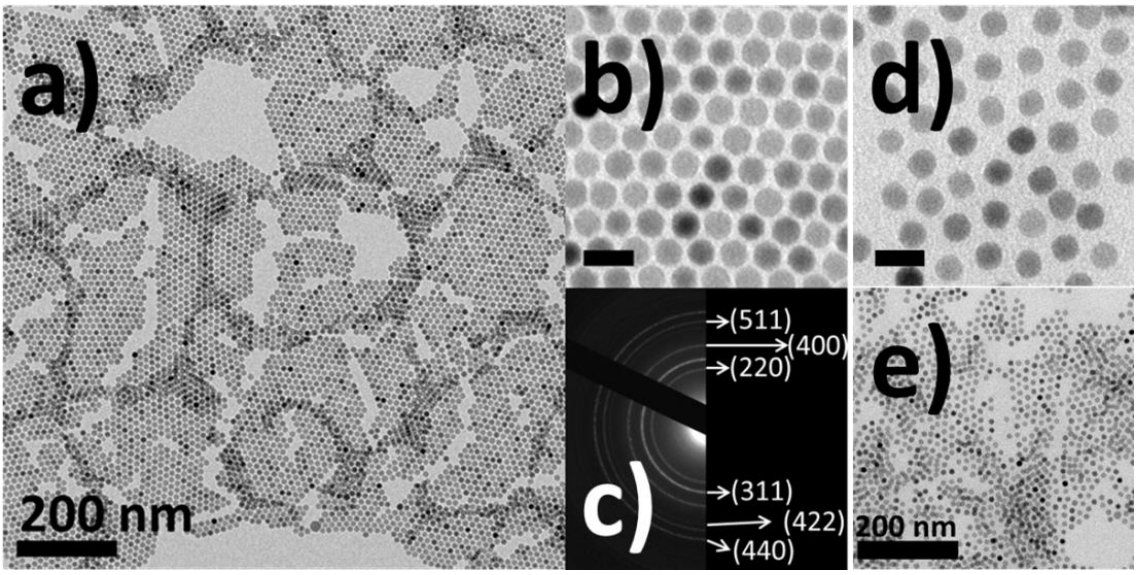

Figure 3.10. TEM images of as-synthesized $Mn_{0.08}Zn_{0.33}Fe_{2.59}O_4$ NCs at a) low magnification and b) high magnification. c) Selected area electron diffraction pattern of the NCs. TEM images of ligand exchanged NCs at d) high magnification and e) low magnification. The scale bars in b) and d) represent 20 nm.

In Figure 3.10a and b, the TEM images of 11 nm as-synthesized $Mn_{0.08}Zn_{0.33}Fe_{2.59}O_4$ NCs are shown. As can be observed in the low (Figure 3.10a) and high (Figure 3.10b) magnification images, the NCs are highly monodisperse and the standard deviation of the size is only 3.7 %. From the selected area electron diffraction pattern in Figure 3.10c, it is observed that the NCs possess spinel crystal structure. Before the ligand exchange, the average interparticle distance is 2.5 nm with 15.7 % of standard deviation. In Figure 3.10d and 3.10e, the TEM image of $Mn_{0.08}Zn_{0.33}Fe_{2.59}O_4$ NCs at high magnification and low magnification after the ligand exchange with G2-PO_3H_2 is presented, respectively. At first glance, it is apparent that the interparticle distance is extended after the ligand exchange. From the TEM image, the average interparticle distance is 5.0 nm with 23.1 % of standard deviation, which means that the interparticle distance is increased by twofold. Even though the standard deviation for the interparticle distance is high, the interparticle distance in each case is in a obviously different range as shown in Figure 3.11.

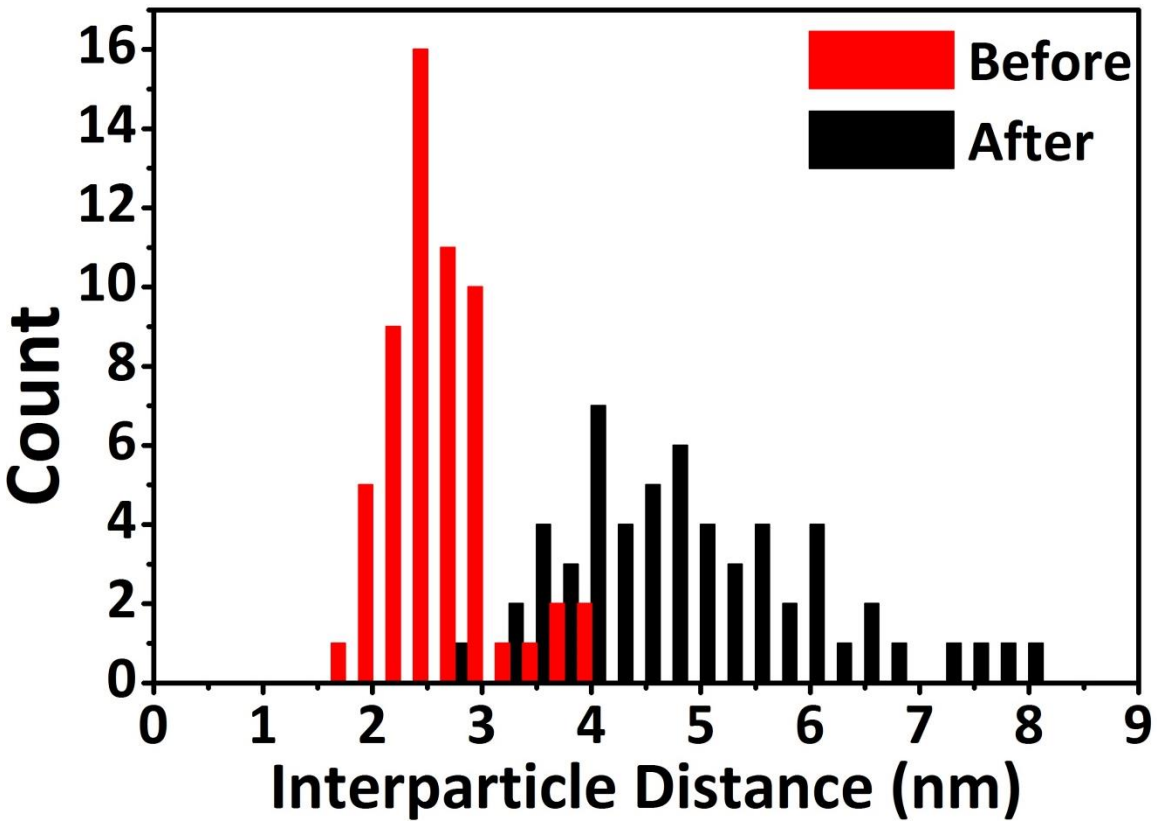

Figure 3.11. The interparticle distance before (red) and after the ligand exchange (black).

After the ligand exchange, we have analyzed how the elongated interparticle distance affects the DC and AC magnetic properties of NCs. In Figure 3.12, the normalized ZFC curves of $Mn_{0.08}Zn_{0.33}Fe_{2.59}O_4$ NCs are given. T_B, the maximum point of the ZFC curve, of the NCs coated is reduced from 114 K to 75 K after the ligand exchange with dendrimers. Although the change is not as huge as the work done by Song *et al.*(~50 K change),[68] it is apparent that the dipolar

interactions between $Mn_{0.08}Zn_{0.33}Fe_{2.59}O_4$ NCs are reduced, which might be useful to increase the FMR frequency of NCs.

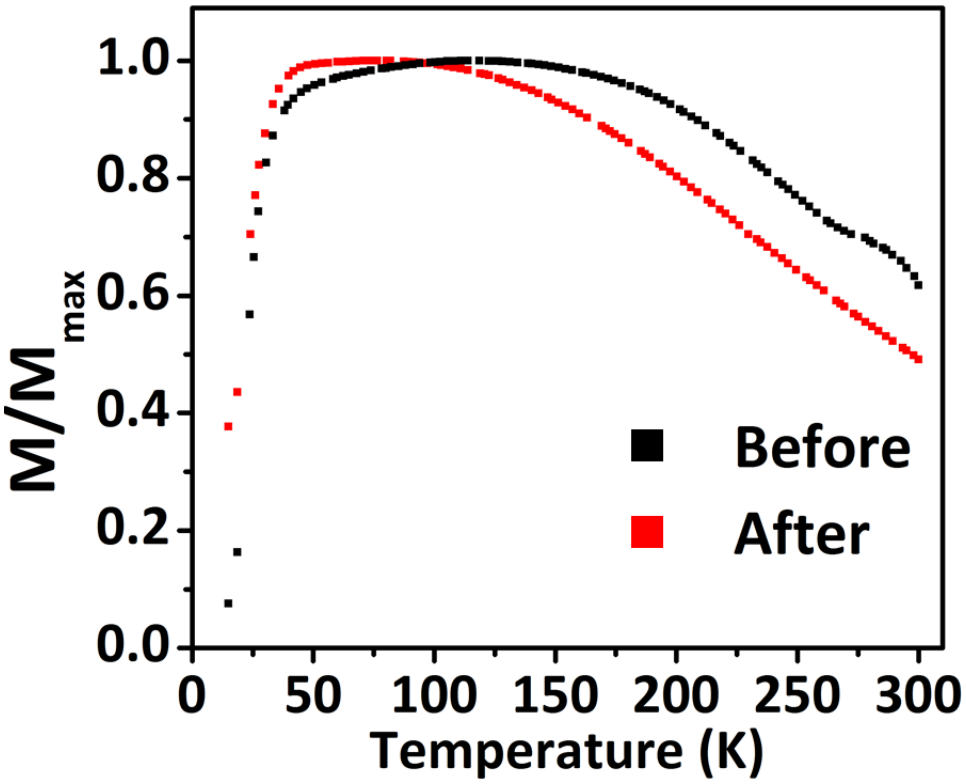

Figure 3.12. ZFC curves of $Mn_{0.08}Zn_{0.33}Fe_{2.59}O_4$ NCs before (black) and after (red) the ligand exchange with dendrimers.

3.7 Composition Dependent DC and AC Magnetic Properties of Manganese Ferrite NCs and Cobalt Ferrite NCs

Cobalt ferrites ($Co_xFe_{3-x}O_4$) with x values from 0.06 to 0.55 and manganese ferrites ($Mn_xFe_{3-x}O_4$) with x values from 0.11 to 0.49 are synthesized by the

literature method with minor modifications.[100] The as-synthesized products have relatively wide size distributions. Therefore size selective precipitation is conducted by adding oleic acid as a precipitant.

In conventional methods,[31,37] polar antisolvents such as ethanol and methanol have been used for size selective precipitation. However, it has been reported that excessive use of short chain protic solvents can strip off the protecting oleate capping ligand on NC surfaces,[178] thus destabilizing the particles. Therefore, oleic acid is employed in this study to avoid this problem. Although oleic acid is a common capping ligand for NCs, it was reported that an excess of oleic acid functioned as an antisolvent to precipitate and purify PbS NCs.[179,180] This can be explained by increased solvent polarity of the hexane – oleic acid mixture. In general, it is observed that as the amount of oleic acid increases, larger particles precipitate first. Thus, oleic acid can serve as an alternative choice for size selective precipitation.

For example, the size selection of the $Mn_{0.44}Fe_{2.56}O_4$ NCs was conducted as described in the experimental section. First, 10 ml oleic acid was added to 20 ml of manganese ferrite hexane dispersion and centrifuged to collect particles in the precipitate and to remove smaller particles remaining in solution. Next, the solid particles were redispersed in 20 ml hexane. Then 7.5 ml oleic acid was added to remove the larger particles in precipitates, and the particles remaining in solution had similar sizes after the selection. On the other hand, when 5 ml & 7.5 ml of

oleic acid were used for size selection, larger average sized particles were obtained. The samples before size selection (A), after size selection by 5 ml - 7.5 ml oleic acid (to remove largest and smallest particles, respectively) (B), and by 7.5 ml - 10 ml oleic acid (C) were collected, and characterized by SAXS to measure their average sizes and size distributions. Figure 3.13 shows the TEM images and SAXS results of samples fitted using spherical form factors.[181] It is shown that the size distribution of both Samples B and C are significantly narrowed after size selection. Moreover, the average size of Sample C (6.3 nm) is obviously smaller than those of Samples A and B (both 7 nm). This proves that the method significantly narrows size distributions and, by adjusting the amount of oleic acid, also produces controllable average sizes within a small range. Using the method described above, the average sizes of different samples were narrowed down and brought closer.

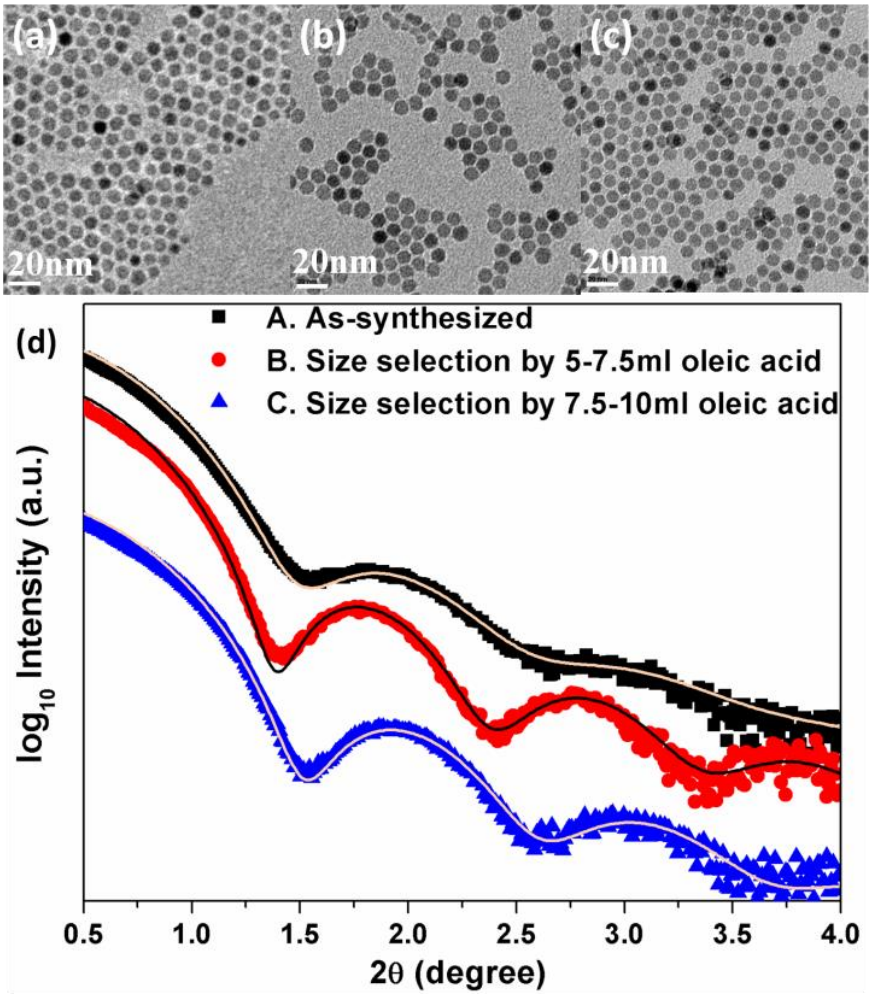

Figure 3.13. TEM images of $Mn_{0.44}Fe_{2.56}O_4$ NCs before size selection(a), after size selection by 5 mL - 7.5 mL oleic acid (b), and by 7.5 mL - 10 mL oleic acid (c). Figure (d) shows SAXS results of the corresponding samples. The average sizes are A: 7.0 nm, B: 7.0 nm C: 6.3 nm. The standard deviations of sizes are A: 12%, B: 6% and C: 8%.

Figure 3.14 shows the TEM and corresponding HRTEM images of representative cobalt ferrite and manganese ferrite samples after size selective

precipitations. The TEM images in Figure 3.15 show that the samples have similar sizes and spherical shapes. Good crystallinity is observed in the HRTEM (Figure 3.14b and d) of the NCs. The lattice distances shown in the images are about 0.257 nm and 0.253 nm for cobalt ferrite NCs and manganese ferrite NCs, respectively, which are close to the reported values[182] of (311) plane spacing in inverse spinel structure.

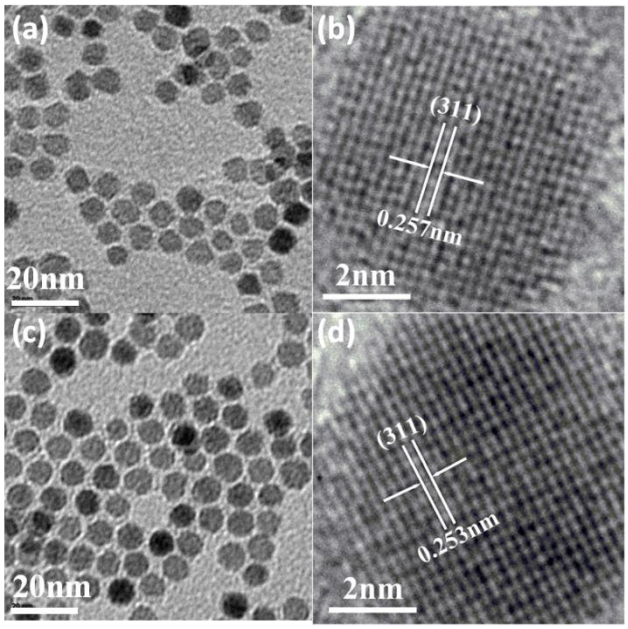

Figure 3.14. TEM and HRTEM images of representative ferrite samples. (a) TEM and (b) HRTEM images of $Co_{0.42}Fe_{2.58}O_4$. (c) TEM and (d) HRTEM images of $Mn_{0.44}Fe_{2.56}O_4$.

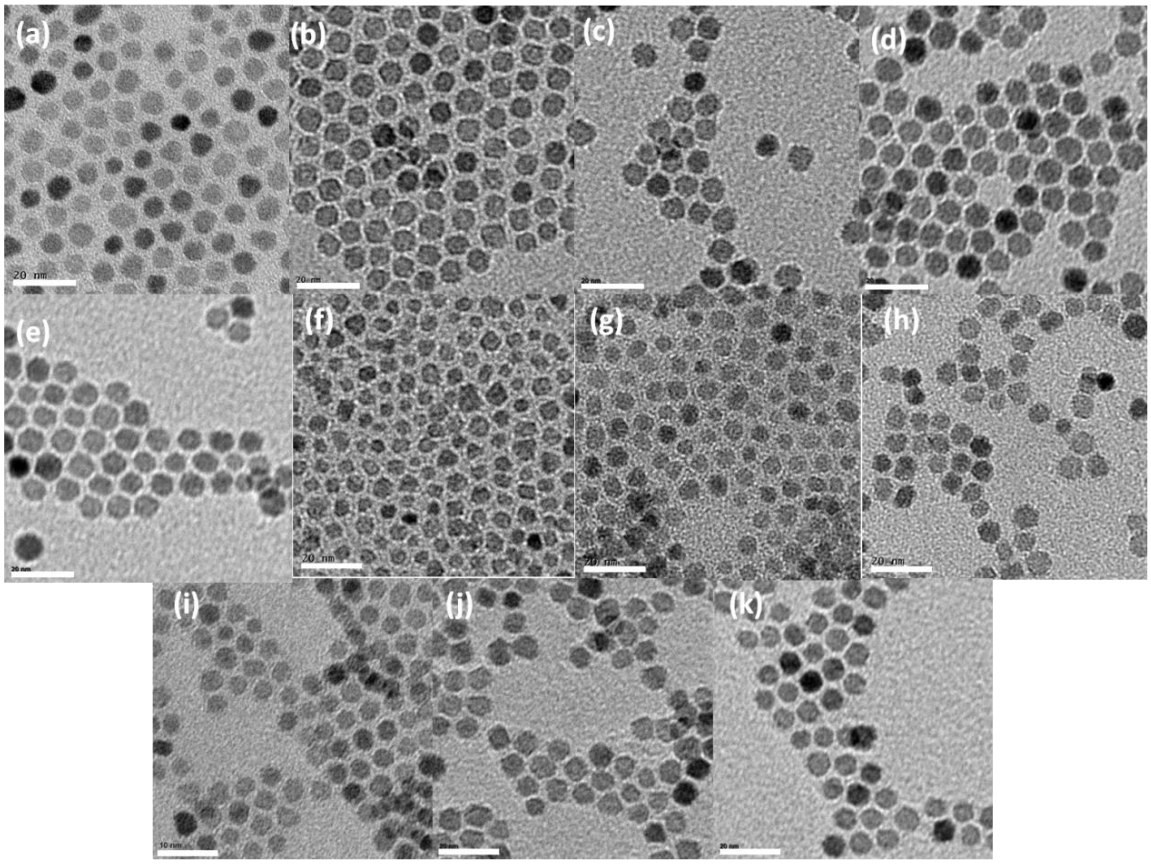

Figure 3.15. TEM images of manganese ferrite and cobalt ferrite NCs. (a) $Mn_{0.11}Fe_{2.89}O_4$, (b) $Mn_{0.18}Fe_{2.82}O_4$, (c) $Mn_{0.29}Fe_{2.71}O_4$, (d) $Mn_{0.44}Fe_{2.56}O_4$, (e) $Mn_{0.49}Fe_{2.51}O_4$, (f) $Co_{0.06}Fe_{2.94}O_4$, (g) $Co_{0.12}Fe_{2.88}O_4$, (h) $Co_{0.19}Fe_{2.81}O_4$, (i) $Co_{0.37}Fe_{2.63}O_4$, (j) $Co_{0.42}Fe_{2.58}O_4$, (k) $Co_{0.55}Fe_{2.45}O_4$. All the scale bars are 20 nm.

Table 3.3. Summary of Mn:Fe and Co:Fe ratios of ferrite samples

	$M(acac)_2$: $Fe(acac)_3$ molar ratios in synthesis	M:Fe molar ratios in products	x values
$Mn_xFe_{3-x}O_4$	1:1.6	1:5.1	0.49
	1:2	1:5.8	0.44
	1:3	1:9.3	0.29
	1:5	1:15.2	0.18
	1:11	1:26.9	0.11
$Co_xFe_{3-x}O_4$	1:1.6	1:4.5	0.55
	1:2	1:6.1	0.42
	1:3	1:7.0	0.37
	1:6	1:15.2	0.19
	1:11	1:23.4	0.12
	1:23	1:47.3	0.06

The compositions of the particles are controlled by adjusting the precursor ratios ($M(acac)_2$: $Fe(acac)_3$, M=Co or Mn) in synthesis. The M:Fe ratios in the NCs were characterized by inductively coupled plasma atomic emission spectroscopy (ICP-AES). In general, higher M:Fe ratios in precursor give rise to higher ratios in products, but the M^{2+} concentrations in products are lower than those in precursors. The $Co(acac)_2$:$Fe(acac)_3$ and $Mn(acac)_2$:$Fe(acac)_3$ molar ratios from synthesis, and the corresponding ratios in NCs are summarized in Table 3.3.

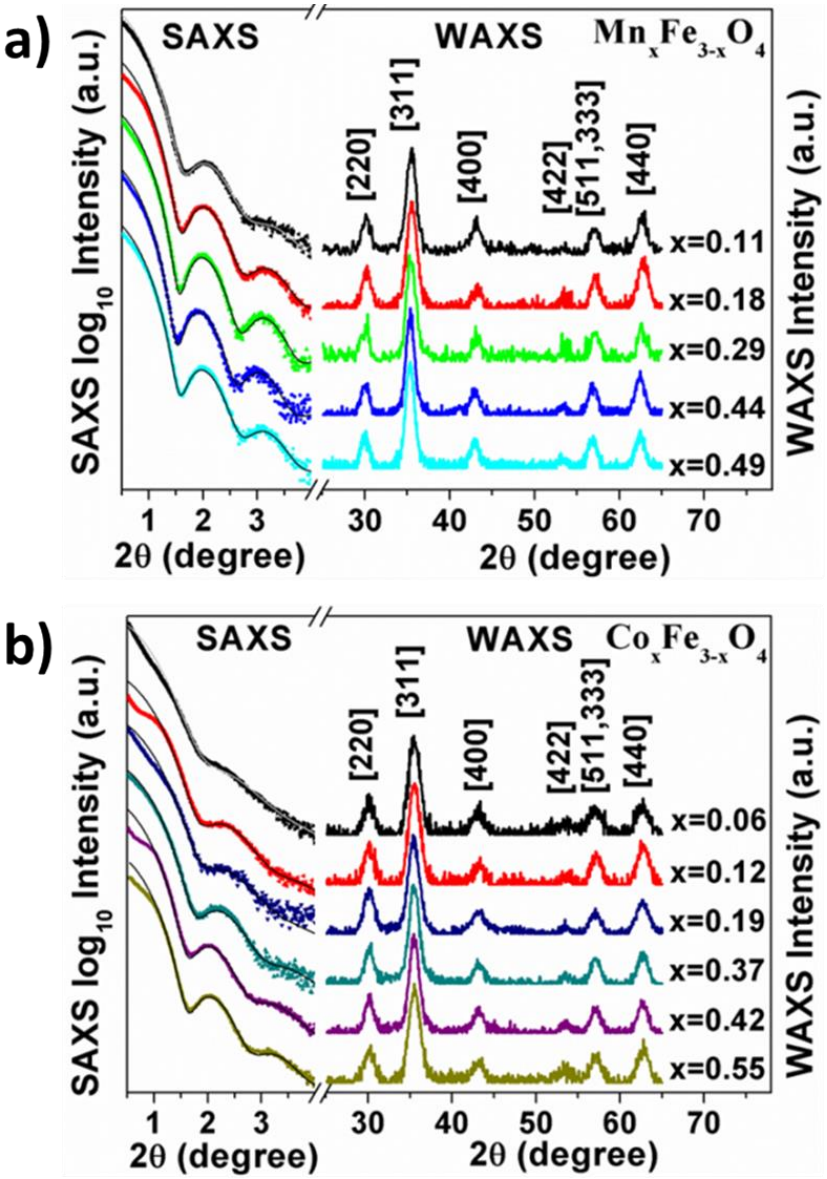

Figure 3.16. SAXS (left) and WAXS (right) plots of (a) manganese ferrites and (b) cobalt ferrites samples. For SAXS plots, the lines show fitting results by Rayleigh function. For WAXS plots, all the peaks correspond to the diffractions from the planes of the spinel ferrite type crystals. (220): 30.1°, (311): 35.5°, (400): 43.0°, (422): 53.3°, (511) and (333): 56.9°, (440): 62.5°.

Table 3.4. Average and standard deviation of sample diameters, determined by SAXS fitting results.

Composition	Average size (nm)	Standard deviation of size (σ)
$Mn_{0.11}Fe_{2.89}O_4$	6.4	11%
$Mn_{0.18}Fe_{2.82}O_4$	6.3	8%
$Mn_{0.29}Fe_{2.71}O_4$	6.3	7%
$Mn_{0.44}Fe_{2.56}O_4$	6.5	7%
$Mn_{0.49}Fe_{2.51}O_4$	6.4	9%
$Co_{0.06}Fe_{2.94}O_4$	6.3	18%
$Co_{0.12}Fe_{2.88}O_4$	5.9	13%
$Co_{0.19}Fe_{2.81}O_4$	6.0	15%
$Co_{0.37}Fe_{2.63}O_4$	6.0	12%
$Co_{0.42}Fe_{2.58}O_4$	6.4	10%
$Co_{0.55}Fe_{2.45}O4$	6.4	10%

The samples were further characterized by x-ray scattering. Figure 3.16 shows the SAXS (left) and WAXS (right) patterns of (a) manganese ferrites and (b) cobalt ferrites samples. The WAXS patterns indicate typical spinel crystal structures in good agreement with reported values.[12,146] The SAXS plots are fitted using Rayleigh function. The average particle sizes and standard size deviations are derived from the fitting results, and summarized in Table 3.4. It can be seen that the NCs with different x values have similar average sizes (5.9 nm to 6.5 nm). The signals from 0.5° to 1.0° were depressed compared to the fitted curves, this is mainly caused by strong interparticle interactions or even aggregation. The size distributions of samples vary with different x values. In synthesis, higher concentration of $Fe(acac)_3$ precursor tends to cause wider size

distribution in the products. For cobalt ferrites, the samples of x = 0.55, 0.42, 0.37 have relatively narrow size distributions (standard deviation σ ≈ 10%), but as the ratio of Fe continues to increase, the x = 0.19, 0.12, 0.06 samples have larger size distributions (σ = 13% to 18%). In contrast, all the manganese ferrite samples show good monodispersity (σ ≤ 9 %) except the sample of x = 0.11(σ = 11%). In general, because of the similar average size, shape and surface coating (oleic acid), the composition dependence of magnetic properties of cobalt and manganese ferrites can be independently studied.

Figure 3.17 shows the DC magnetic properties (ZFC, FC and hysteresis) on cobalt and manganese ferrites NCs. Figure 3.17a and b show the ZFC-FC curves of samples. The temperature at which the ZFC and FC curves converge is the T_B above which the hysteresis of NCs reduce to zero and the NCs become superparamagnetic.[37] At T_B, the anisotropic energy KV is proportional to the thermal energy of particles, $k_B T_B$.[93,30] Considering that all samples have similar volume, a higher T_B indicates higher magnetocrystalline anisotropy (K) of the NCs.

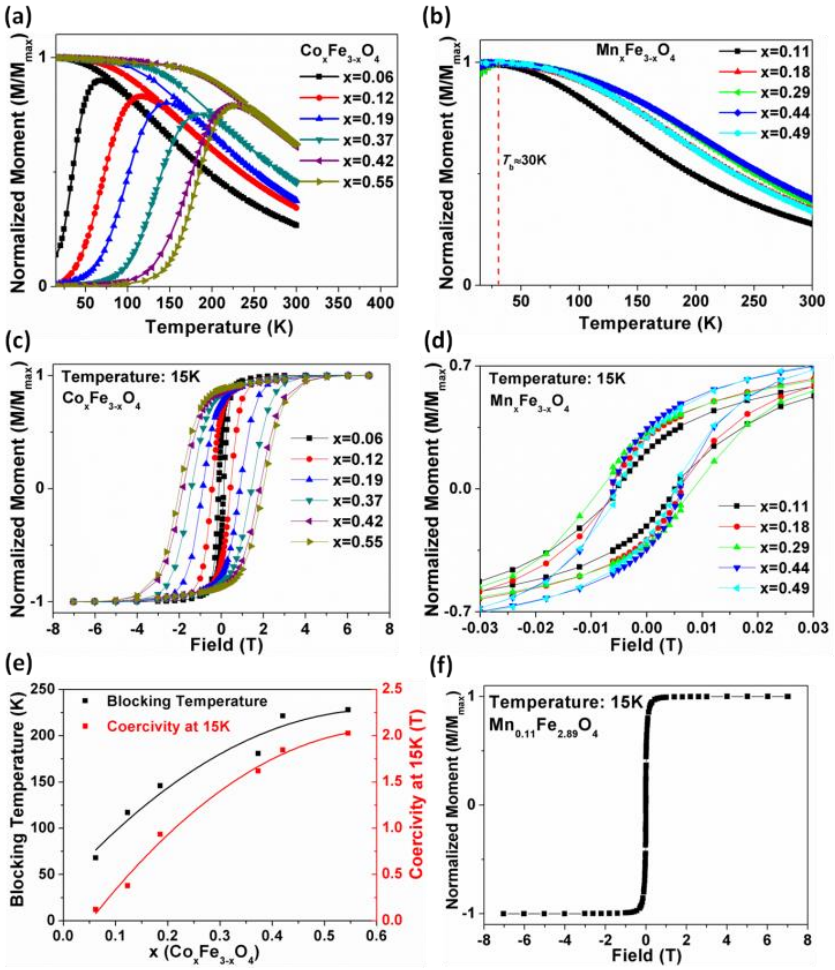

Figure 3.17. DC magnetic characterizations of cobalt and manganese ferrites samples. ZFC and FC curves of (a) cobalt ferrites and (b) manganese ferrites. (c) Hysteresis curves of cobalt ferrites taken at 15K. (d) Hysteresis curves of all manganese ferrites samples zoomed in at around zero field to show H_c of samples. (e) $\boldsymbol{T_B}$ (black), and H_c at 15K (red) plotted against x of $Co_xFe_{3-x}O_4$, the curves are polynomial fitting results to show the trends. (f) Hysteresis curve of manganese ferrite ($Mn_{0.11}Fe_{2.89}O_4$) at 15K.

The T_B values of cobalt ferrites are summarized in figure 3.17e. It can be seen that T_B increases from 60K to 260K as x increases from 0.06 to 0.55, revealing the same trend for anisotropy values. Figure 3.17c shows the 7 T hysteresis curves of cobalt ferrite samples at 15K. Figure 3.17e summarizes the H_c at 15K for all samples. The H_c of samples increases as the ratio of Co increases in composition. This is in good agreement with the literature results.[146] At 300K, all samples show superparamagnetic behavior, with zero H_c (Figure 3.18). In general, the increasing H_c and T_B is due to the increasing magnetocrystalline anisotropy associated with the spin-orbital coupling effect of Co^{2+}.

The magnetic properties of manganese ferrites show sharp contrast with those of cobalt ferrites. Figure 3.18b shows that all manganese ferrite samples have almost the same T_B (~ 30K), which is much lower than that of cobalt ferrites. The spin-orbital coupling effect of Co^{2+} is absent in Mn^{2+} because the orbital momentum is quenched in Mn^{2+},[28] which explains why T_B is not affected by the amount of manganese as much as that of cobalt. Considering that all samples have similar average size, the same T_B indicates that all samples have similar anisotropy coefficient. Besides, all the samples show very small H_c values (about 6 mT) even at 15 K (Figures 3.17d, 3.17f, and 3.19). At 300 K, all samples show almost identical hysteresis with zero H_c (Figure 3.20). In general, the

manganese ferrite samples share similar DC magnetic properties despite differences in their compositions.

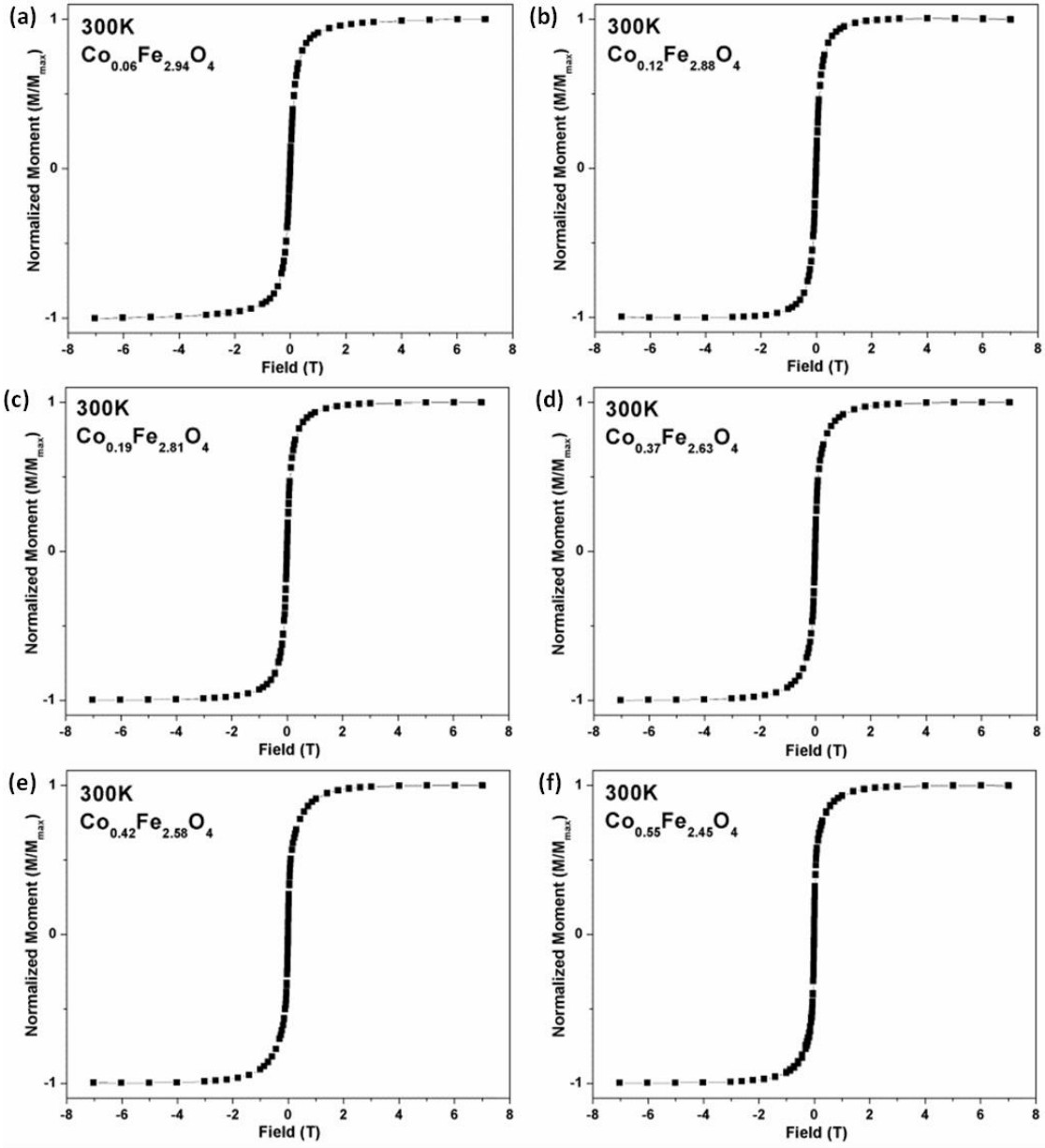

Figure 3.18. Hysteresis curves of cobalt ferrite ($Co_xFe_{3-x}O_4$) NCs taken at 300K. (a) x = 0.06, (b) x = 0.12, (c) x = 0.19, (d) x = 0.37, (e) x = 0.42, (f) x = 0.55.

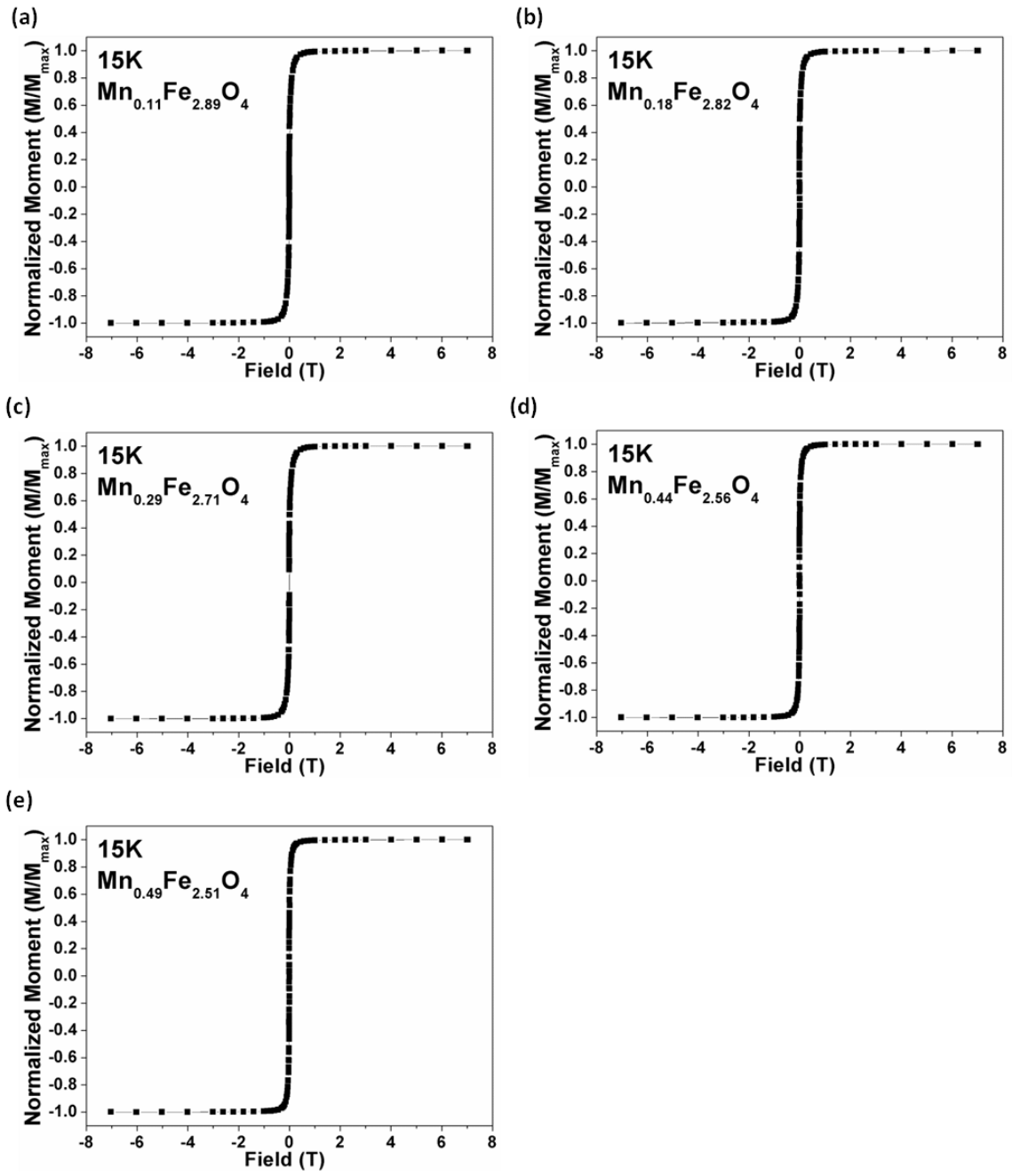

Figure 3.19. Hysteresis curves of manganese ferrite ($Mn_xFe_{3-x}O_4$) NCs taken at 15K. (a) x = 0.11, (b) x = 0.18, (c) x = 0.29, (d) x = 0.44, (e) x = 0.49.

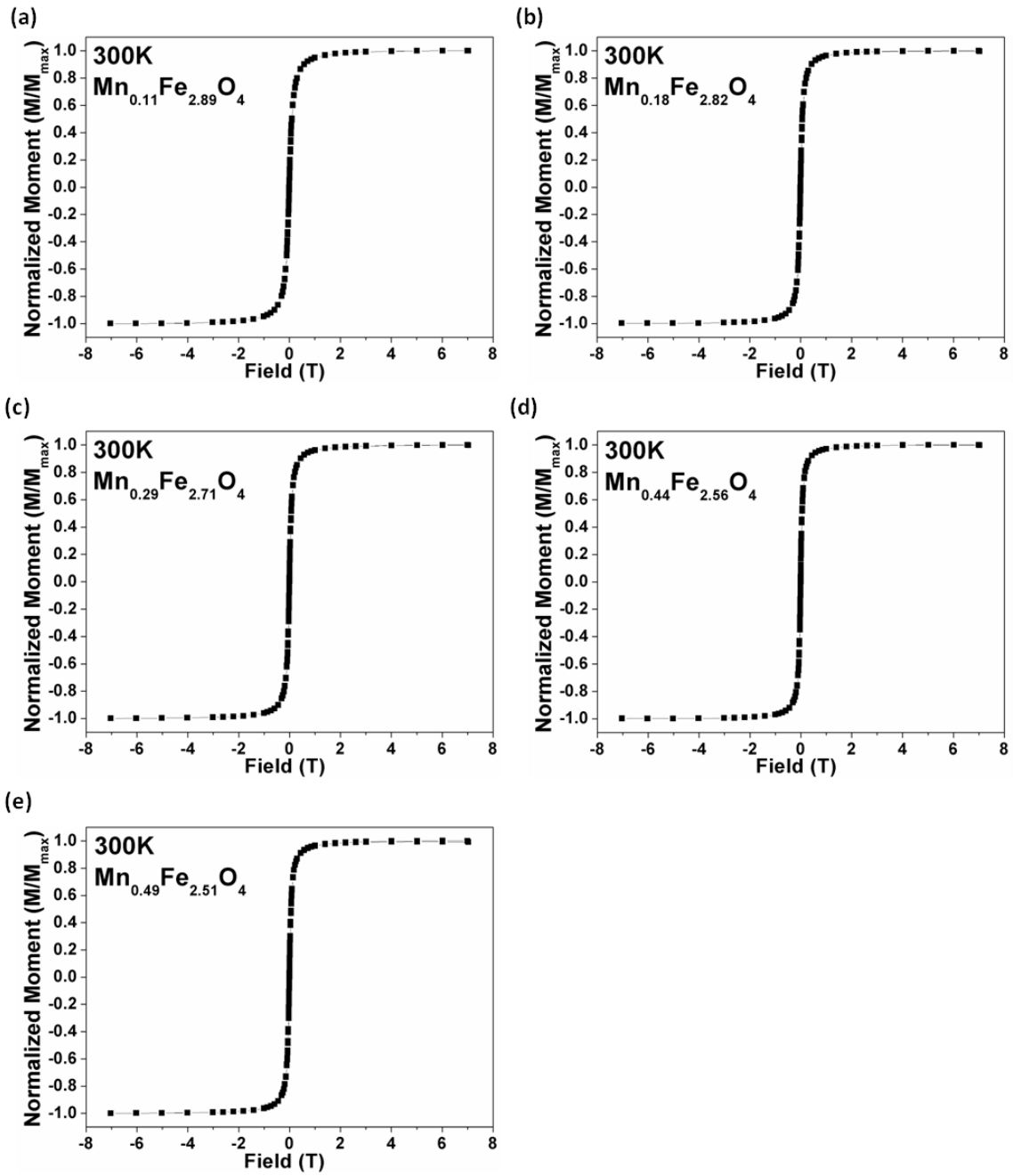

Figure 3.20. Hysteresis curves of manganese ferrite ($Mn_xFe_{3-x}O_4$) NCs taken at 300K. (a) x = 0.11, (b) x = 0.18, (c) x = 0.29, (d) x = 0.44, (e) x = 0.49.

Figure 3.21b and d shows the frequency dependent χ' and χ'' for manganese ferrite samples. Again, the trend is very different from that of cobalt ferrites. The χ' and χ'' values for manganese ferrites are higher than those of cobalt ferrite samples, this is because manganese ferrite has higher M_S associated with a larger moment for Mn^{2+} versus Co^{2+}.[28,183] Manganese ferrite is inverse spinel ferrite and Mn^{2+} replaces Fe^{2+} ions in the octahedral sites.[184,185] Because Fe^{2+} has only 4 unpaired electrons, compared to 5 for Mn^{2+}, as the ratio of Mn:Fe increases, higher M_S results,[32] which explains why the χ' and χ'' values increases with increasing Mn:Fe ratios.

Unlike the trend of cobalt ferrites, the χ'' values of manganese ferrites increase monotonically with frequency (Figure 3.21d). This implies that the superparamagnetic-ferromagnetic relaxation frequencies of samples are higher than 500MHz, so the Néel relaxation time of manganese ferrites is much shorter than that of cobalt ferrites, which indicates very small anisotropic energy (KV) of particles. Also, this is originated from the 3d orbital configurations. The 5 unpaired electrons of Mn^{2+} occupy all 3d octahedral orbitals symmetrically, leading to zero net orbital angular momentum. As a result, the spin-orbital coupling is mostly quenched, giving rise to a much lower crystal anisotropy.[28]

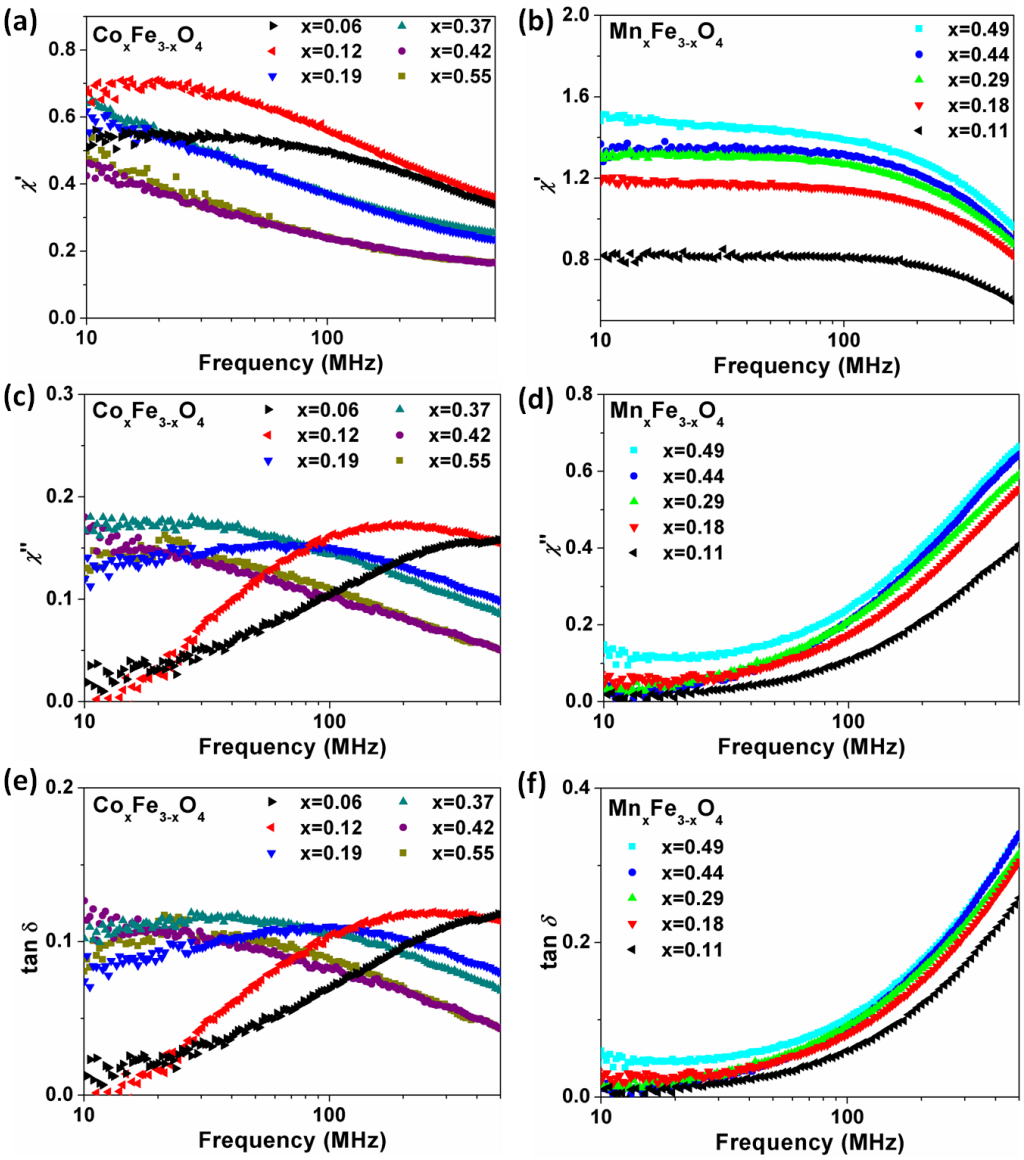

Figure 3.21. Frequency dependent χ' and χ'' plots of cobalt and manganese ferrites. χ' plots of (a) cobalt and (b) manganese ferrites. χ'' plots of (c) cobalt and (d) manganese ferrites. Loss tangent (*tan* δ) plots of (e) cobalt and(f) manganese ferrites.

χ" is closely related to the energy dissipation efficiency. According to Rosensweig's model[46,72], the specific loss of power (SLP) is proportional to the product of AC field frequency and χ". When other conditions are identical, it is expected that magnetic NCs with higher χ" value will have higher energy dissipation efficiency. Therefore, from the χ" plots in Figure 3.21c and 3.21d we can predict that the SLP of the cobalt ferrite NCs vary with different Co:Fe ratios at the frequency of measurement. On the other hand, for manganese ferrites, SLP is relatively insensitive to Mn doping level. A very low SLP value is expected below 100MHz, but increases rapidly as frequency continue to increase, as can be seen from the trend of χ" plots.

Figure 3.21e and 3.21f shows the loss tangent curves of cobalt and manganese ferrite samples. The loss tangent is defined as tan $\delta = \chi"/(\chi'+1)$. For low power loss device applications, high χ' and low χ" are desired to enhance magnetic field strength and suppress energy loss at the same time. Therefore tan δ is a comprehensive indication of the energy efficiency of NCs as magnetic core material for electromagnetic device applications. From Figure 3.21f we can see that the values of tan δ are very close for all samples except $Mn_{0.11}Fe_{2.89}O_4$. Although the magnetic moment is slightly enhanced by introducing higher amount of manganese, the χ" value increases by the same ratio, giving rise to higher energy loss at the same time. On the other hand, the sample $Mn_{0.11}Fe_{2.89}O_4$ has slightly lower tan δ value in the frequency range of

measurement. This is probably caused by its wider size distribution.[55] For cobalt ferrites, the loss tangent curves are very similar to the χ" curves. By changing the amount of cobalt, the maximum value for the tangent loss shifts from about 10 MHz (x=0.55) to about 500MHz (x=0.06).

3.8 Conclusion

In summary, I have shown the synthesis of various types of nonstoichiometric ferrite NCs such as $Zn_xFe_{3-x}O_4$, $Mn_xFe_{3-x}O_4$, $Co_xFe_{3-x}O_4$, and $Mn_aZn_bFe_{3-a-b}O_4$ NCs. We observe that iron oxide NCs with higher Zn concentration and larger sizes possess higher μ_r', but also a higher μ_r''. 12.3 nm $Zn_{0.25}Fe_{2.75}O_4$ NCs show the highest magnetic permeability with ~ 19 at 1 MHz and almost twice of that of similar sized iron oxide NCs. Even though the FMR frequency is reduced as the Zn doping level increases, the relative loss tangent curves indicate that zinc ferrite NCs do not suffer from significant energy loss as compared to iron oxide NCs. These inductors are prepared through a cheap and scalable solution based deposition process. Both toroidal and solenoid inductors exhibit higher quality factor than those of the air core inductors with same geometries up to 5 MHz and 8-9 MHz, respectively, which proves that zinc ferrite NCs are suitable for miniaturized inductors operating at radio frequencies. The ligand exchange with dendrimers weakens the interparticle interaction and effectively increases the FMR frequency, allowing the NCs to be operable in a wider range of frequencies.

Further investigation should be conducted to understand and improve the AC magnetic properties of chemically synthesized magnetic NCs.

On the other hand, the composition dependent magnetic characterizations of $Co_xFe_{3-x}O_4$ show that introducing Co^{2+} to ferrite NCs increases significantly the magnetocrystalline anisotropy energy, causing shifts in superparamagnetic-ferromagnetic relaxation frequency. In the case of $Mn_xFe_{3-x}O_4$, different amounts of Mn^{2+} in ferrite NCs result in similar DC and AC magnetic properties. The superparamagnetic-ferromagnetic relaxation frequencies, and loss tangents curves all have identical trends. These composition dependent behaviors provide another important dimension of tuning the DC and AC magnetic properties of spinel ferrite NCs, other than changing the size, shape and various surface modifications, to meet the needs for different applications.

3.9 Experimental Section

3.9.1 Materials. Zinc (II) acetylacetonate, iron (III) acetylacetonate (99+ %), manganese (II) acetylacetonate, 1-octadecene (technical grade, 90 %) were purchased from Acros Organics. Cobalt (II) acetylacetonate (97%), oleic acid (technical grade, 90 %) and oleylamine (technical grade, 70 %), 1,2-tetradecanediol (90%), and benzyl ether (98 %) were purchased from Sigma-Aldrich. All the chemicals were used as received.

3.9.2. Synthesis of $Zn_{0.25}Fe_{2.75}O_4$ NCs. 6 mmol of zinc (II) acetylacetonate, 12 mmol of iron (III) acetylacetonate, 100 mmol of oleic acid, 112 mmol of oleyl amine, and 72 mL of 1-octadecene are mixed in a 250 mL flask. The reaction mixture is heated to 110 °C and kept under vacuum for two hours. Then, the temperature is increased to 300 °C at a rate of 10 °C/min. After two hours, the reaction mixture is cooled down to the room temperature and zinc ferrite NCs are precipitated by adding isopropanol. Zinc ferrite NCs could be redispersed in hexane and washed further using isopropanol for three times. In result, 8.3 nm spherical $Zn_{0.25}Fe_{2.75}O_4$ NCs are obtained as can be seen in Figure 3.2k The composition ratio between zinc and iron is decided by ICP-OES. By increasing the heating rate to 11.7 and 15 °C/min, the size of zinc ferrite NCs can be increased to 10.1 and 12.3 nm, respectively (Figure 3.2j and i).

3.9.3. Synthesis of iron oxide NCs and $Zn_{0.1}Fe_{2.9}O_4$ NCs. 12 mmol of iron (III) acetylacetonate, 100 mmol of oleic acid, 112 mmol of oleyl amine, and 72 mL of 1-octadecene are mixed in a 250 mL flask. The reaction mixture is heated to 110 °C and kept under vacuum for two hours. Then, the temperature is increased to 300 °C at a rate of 10 °C/min. After one hour, the reaction mixture is cooled down to the room temperature and iron oxide NCs are precipitated by adding isopropanol. Iron oxide NCs are redispersed in hexane and washed further using isopropanol for three times. In result, 7.8 nm spherical iron oxide NCs are

obtained as can be seen in Figure 3.2c. By increasing the amount of iron (III) acetylacetonate from 12 mmol to 15 mmol and 18 mmol, 9.3 nm and 12.8 nm iron oxide NCs could be obtained, respectively. To synthesize 7.4 nm $Zn_{0.1}Fe_{2.9}O_4$ NCs, 0.5 mmol of Zn (II) acetylacetonate is added into the same reaction mixture for 7.8 nm iron oxide NC synthesis. For larger sizes of NCs, the amount of Zn (II) acetylacetonate is increased to 0.63 mmol and 0.75 mmol for 10.2 nm and 13.8 nm $Zn_{0.1}Fe_{2.9}O_4$ NCs, respectively.

3.9.4. Synthesis of $Mn_{0.08}Zn_{0.33}Fe_{2.59}O_4$ NCs. To synthesize 11 nm $Mn_{0.08}Zn_{0.33}Fe_{2.59}O_4$ NCs, 3 mmol of Mn (II) acetylacetonate is added into the reaction condition for the synthesis of 8.3 nm $Zn_{0.25}Fe_{2.75}O_4$ NCs and all the other conditions are kept same.

3.9.5. Synthesis of cobalt and manganese ferrites NCs. The nonstoichiometric cobalt ferrite NCs are synthesized by methods reported in the literature[25] with minor modifications. First, iron (III) acetylacetonate and cobalt (II) acetylacetonate with molar ratios varying from 23:1 to 1.6:1 and a total of 12 mmol are added to a three neck flask, together with 8 mmol of oleic acid, 40 mmol of oleylamine, 24 mmol of 1,2-tetradecanediol, and 12 mL of benzyl ether. The mixture is heated to 110 °C under fast N_2 flow and kept for 60 minutes and then heated at a rate of 8 °C/min to 205 °C and kept for 90 minutes. Next, the

reaction is heated to 295 °C with 8 °C/min ramp rate and kept at this temperature for one hour to yield narrow size distribution,[5] then cooled to room temperature. To purify samples, oleic acid is added to reaction mixture with 1:1 volume ratio to precipitate NCs. The particles are then redispersed in hexane solution, and washed with ethanol one time. By replacing cobalt (II) acetylacetonate with manganese(II) acetylacetonate while keeping all the other experimental conditions the same, nonstoichiometric manganese ferrite NCs are prepared.

3.9.6. Size selective precipitation of NCs. To further reduce the size distribution of particles (from 12 % to 6-8 % in the case of $Mn_{0.44}Fe_{2.56}O_4$ NCs), size selective precipitation is conducted using oleic acid as the precipitant. To 20 mL of hexane dispersion of NCs is added 10 mL of oleic acid dropwise and mixed by shaking the solution after each drop. When precipitates are observed in the solution during the process, the solution is centrifuged under 8000 RPM for 10 minutes and then the supernatant is discarded removing the smaller particles in the dispersion. The precipitate is redispersed in 20 mL of hexane, and 7.5 mL of oleic acid is added dropwise, shaking after each drop to partially precipitate the NCs. The solution is centrifuged again under 8000 RPM for 10 minutes to remove largest particles in the distribution. Next, 5 mL oleic acid is added to the supernatant and centrifuged to precipitate all remaining particles. The precipitate

is dispersed in hexane, and washed one more time with ethanol to remove extra oleic acid.

3.9.7. Preparation of solenoid inductor. To prepare solenoid inductor with 12.3 nm $Zn_{0.25}Fe_{2.75}O_4$ NCs, a tube made of polyolefin, which contracts if heated, is used. This tube has 10.9 mm of length and 3.4 mm of diameter. One of the ends is closed and the other end is open. The tube is filled with 12.3 nm $Zn_{0.25}Fe_{2.75}O_4$ NCs by simple solution drop and dry process. After the tube is completely filled with the NCs, the open end is also sealed by melting the polyolefin. Then, the tube is heated by a heat gun to induce contraction, which increases the filling factor of the NCs. After the contraction, the final diameter became 3.1 mm. Then, a seed metal layer is wound around the tube for 10 times and electroplated.

3.9.8. Synthesis of ((11-(4-(((2-Methyl-3-((2-methyl-3-(stearoyloxy)-2-((stearoyloxy) methyl)propanoyl)oxy)-2-(((2-methyl-3-(stearoyloxy)-2-((stearoyloxy)methyl) propanoyl)oxy)methyl)propanoyl)oxy)methyl)-1H-1,2,3-triazol-1-yl)undecyl) phosphonic acid) 8, G2-PO3H2. Synthesis of 8 is achieved *via* late stage functionalization strategy. NC anchoring unit, phosphonic acid is installed on dendritic alkyne 7 using click reaction during the last synthetic step avoiding the use of protecting groups. Advanced intermediate 7 is prepared from commercially available 2,2-bis(hydroxymethyl)propionic acid (Bis-MPA) 1

via number of synthetic transformations through anhydride coupling (Scheme 3.1) followed by a literature procedure reported previously.[186]

To a stirred solution of (((2-methyl-2-((prop-2-yn-1-yloxy)carbonyl)propane-1,3-diyl)bis(oxy))bis(carbonyl))bis(2-methylpropane-2,1,3-triyl) tetrastearate 7 (0.5 g, 0.34 mmol), (12-azidododecyl)phosphonic acid (0.119 g, 0.41 mmol) and $CuSO_4 \bullet 5H_2O$ (0.13 g, 0.52 mmol) in THF/H_2O 4:1 (5 mL) was added sodium ascorbate (0.135 g, 0.68 mmol) and the resulting mixture stirred at 65 °C for 10 h under microwave irradiation (constant temperature mode). The solvent is evaporated and the residue is dissolved in $CHCl_3$ (60 mL) and washed with 2N HCl (3 x 20 mL). The organic layer is dried over anhydrous Na_2SO_4, filtered and the filtrate is concentrated under reduced pressure. The crude product is redisolved in $CHCl_3$ (5 mL) and mixed with MeOH (100 mL). White precipitate is collected by filtration and dried to afford title compound 8 (0.497 g, 83%) as white solid. ^{1}H NMR ($CDCl_3$, Figure 3.23) δ 7.72 (s, 1H), 5.25 (s, 2H), 4.36 (t, *J* = 7.3 Hz, 2H), 4.23 (q, *J* = 11.1 Hz, 4H), 4.14 (t, *J* = 8.4 Hz, 8H), 2.27 (t, *J* = 7.5 Hz, 8H), 1.98 – 1.83 (m, 2H), 1.83 – 1.67 (m, 2H), 1.57 (p, *J* = 7.3 Hz, 11H), 1.47 – 1.18 (m, 133H), 1.17 (s, 6H), 0.87 (t, *J* = 6.7 Hz, 12H); ^{13}C NMR ($CDCl_3$, Figure 3.24) δ 173.34, 172.27, 172.13, 65.64, 65.09, 58.48, 50.71, 46.79, 46.49, 34.16, 32.06, 30.71, 30.60, 30.39, 29.84, 29.82, 29.80, 29.78, 29.64, 29.61, 29.52, 29.49, 29.44, 29.28, 29.21, 29.14, 26.67, 25.00, 22.82, 22.24, 17.89, 17.65,

14.24; MALDI-TOF (m/z): $[M+Na]^+$ calcd. for $C_{102}H_{190}N_3O_{17}Na$, 1783.3731; found 1783.696.

3.9.9. Ligand exchange of Mn0.08Zn0.33Fe2.59O4 NCs with G2-PO3H2 dendrimers. Into 5 mL of the NCs solution in hexane (~ 5mg of NCs/mL), 25 mg of G2-PO_3H_2 is added and kept for 24 hours at 40 °C. Then, the NCs are precipitated by adding isopropanol and centrifuged. The colorless and transparent supernatant is removed and the precipitate is redispersed in hexane.

Please refer chapter 2.7 for the experimental procedure for DC (Chapter 2.7.5), AC (Chapter 2.7.6) magnetic characterizations, and structural characterization (Chapter 2.7.7).

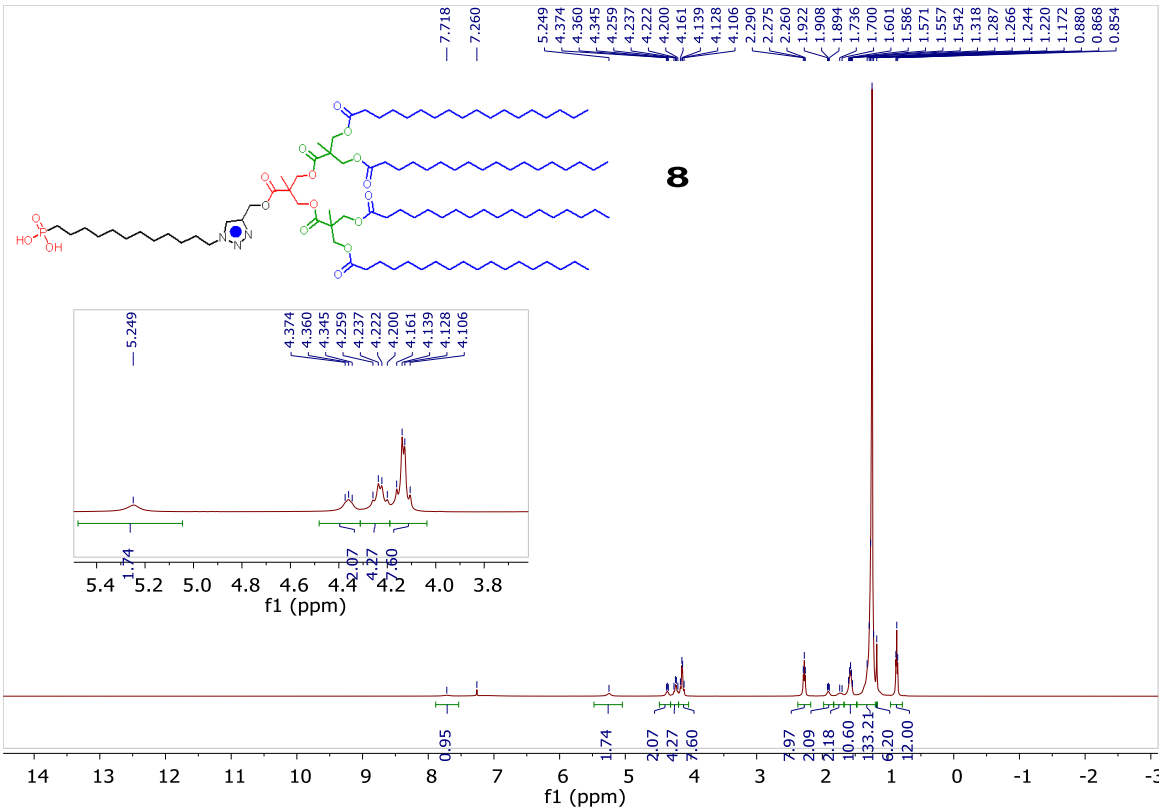

Figure 3.22. The ^{1}H-NMR of G2-PO_3H_2 dendrimer.

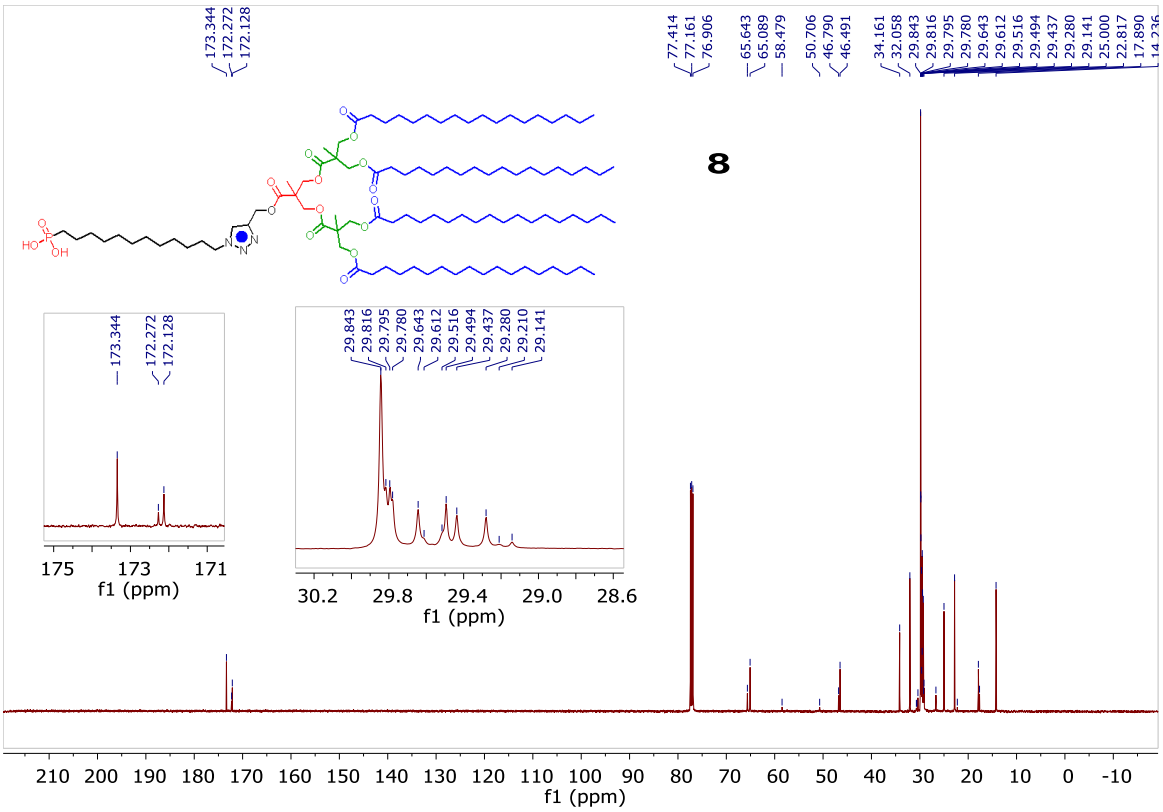

Figure 3.23. The ^{13}C-NMR of G2-PO_3H_2 dendrimer.

CHAPTER 4. Temperature Dependent Energy Efficiency of Hand-Wound Inductors with Zinc Ferrite Nanocrystal Cores (Collaborated with David Otten)

4.1 Introduction

One of the intriguing characters of magnetic NCs is that they can release heat under an AC magnetic field. Hyperthermal cancer treatment takes advantage of this heat to kill tumor cells, and there have been many reports about how much heat is actually dissipated from NCs.[11,43,44,72] In particular, Riedinger *et al.* show that the local temperature of diluted NCs in water under an AC magnetic field can be increased up to 45 °C (ΔT) at distances below 0.5 nm from a given magnetic nanoparticle.[45] This result indicates how much single nanoparticle can increase the local temperature of proximate environment. There are several heat release mechanisms such as hysteresis loss,[94] eddy current loss,[187] and Néel[42] and Brownian relaxation loss.[46] Néel relaxation is expressed as $\tau = \tau_0 exp^{KV/k_bT}$, as discussed in Chapter 2. This thermal relaxation equation indicates that the relaxation time is dependent on the temperature of the NC.

While the heat is released to the surroundings in the case of colloidal NCs, how their AC magnetic behavior interplays with a temperature change has not been well-studied in a solid state. High temperature AC magnetic behavior is important, especially in magnetic devices, such as inductors and transformers,

because the typical operating temperature of such devices is 70 – 100 °C.[28] For inductors operating at radio frequencies, the AC properties of magnetic materials are important to miniaturize the system without suffering from magnetic energy losses such as hysteresis loss and eddy current loss. At high frequencies, hysteresis loss and eddy current loss dominate and reduce the energy efficiency of the system with magnetic materials. Thus a large amount of energy is dissipated as heat and the temperature of the system increases.[94,187] Due to the raised temperature, the resistance of the inductor increases as well, leading to a larger resistive loss and lower efficiency of the circuit. This explains the necessity for the magnetic property characterizations at high temperature. In this section, I will discuss the temperature dependent power efficiency of a power converter with a NC core inductor.

4.2 DC and AC Magnetic Characterization of Zinc Ferrite NCs

In Figure 4.1, a representative TEM image and WAXS of 9.5 nm (averaged by TEM) $Zn_{0.27}Fe_{2.73}O_4$ NCs are presented. The TEM image shows fairly uniform zinc ferrite NCs with 9 % size distribution according to the TEM images and WAXS data indicate that the NCs possess spinel structures. The ratio between Zn and Fe is determined by ICP-OES. The hysteresis curve at 300 K (Figure 4.2) proves that the NCs are in a superparamagnetic state. The H_c values are 0 and ~12 mT at 300 K and 15 K, respectively. Therefore, these NCs can be

considered proper subjects to analyze the high temperature AC magnetic behavior of superparamagnetic NCs.

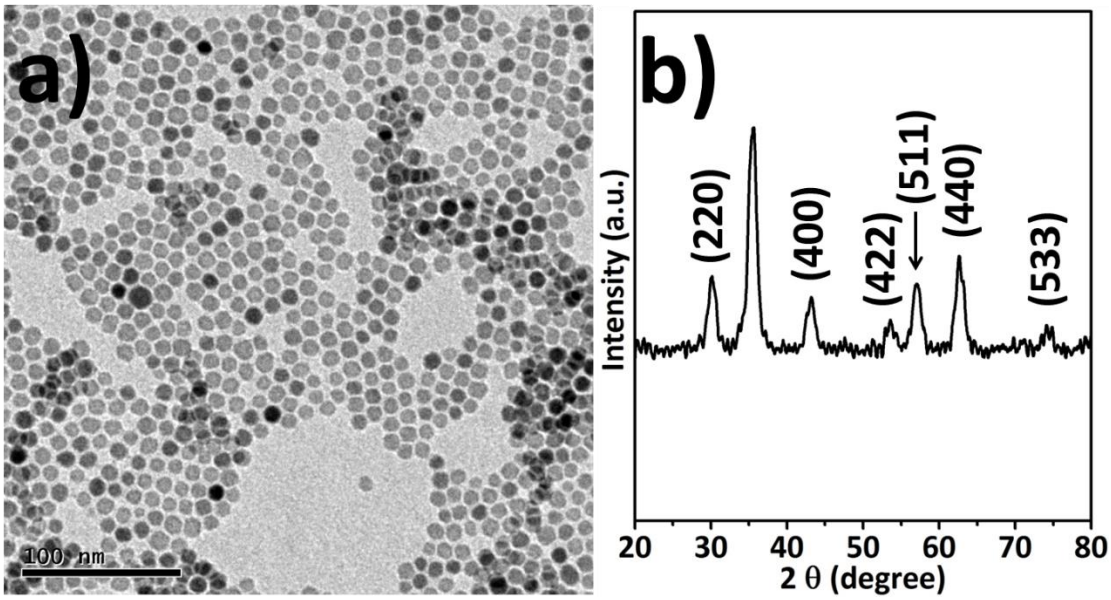

Figure 4.1. a) A TEM image of 9.5 nm $Zn_{0.27}Fe_{2.73}O_4$ NCs and b) their WAXS.

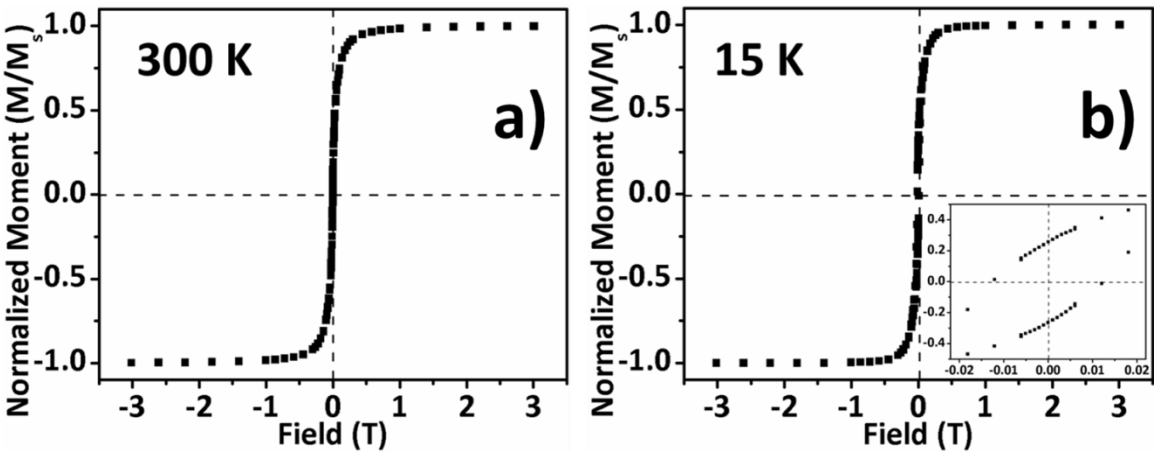

Figure 4.2. Hysteresis curves of 9.5 nm $Zn_{0.27}Fe_{2.73}O_4$ NCs at a) 300 K and b) 15 K. The inset in b) is the enlarged image of b).

In Figure 4.3a-c, the relative magnetic permeability data of the NCs are presented. 9.5 nm zinc ferrite NCs possess 9-10 of μ' value at 1 MHz, which is consistent with the size dependence trend demonstrated in Chapter 3. μ' is stable up to 30-40 MHz and then decreases steadily. μ'' increases exponentially and reaches to its maximum at ~300 MHz. This sample is formed into a toroidal shape core (6.3 mm of outer diameter, 3 mm of inner diameter, and 1 mm of thickness) by using the process demonstrated in Chapter 2. The inductance is about 1.6 μH and the quality factor is ~ 60 at 1 MHz. The inductance reduces spontaneously from 1 MHz to 50 MHz and then increases due to the resonance of the inductor. The operating frequency of the power converter in this study is from 5 MHz to 7 MHz, where this inductor maintains relatively low resistance and a good quality factor (~ 10).

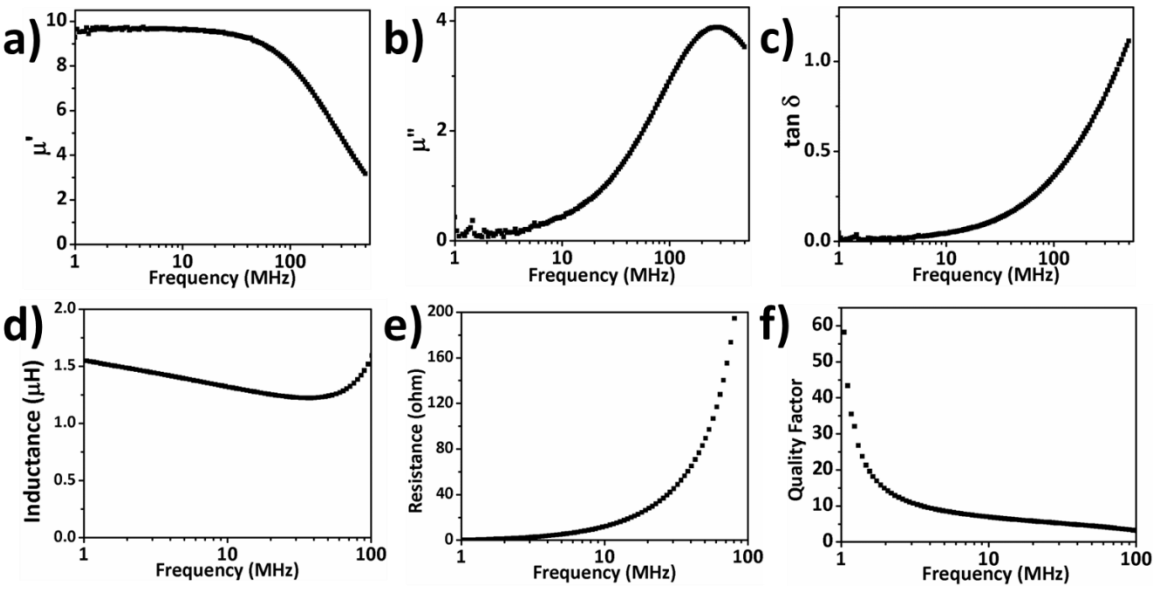

Figure 4.3. a) The μ_r', b) μ_r", and c) tangent loss of 9.5 nm $Zn_{0.27}Fe_{2.73}O_4$ NCs. d) The inductance, e) resistance, and f) quality factor of a 25 turn hand-wound toroidal inductor with a NC core.

4.3 Temperature Dependent Efficiency of a Power Converter with an Inductor with NC Core

In Figure 4.4a, the photograph image of the experimental setup for the temperature measurement of a power converter is presented. With the setup, the temperature of the inductor can be measured while the power efficiency of the power converter is collected. In Figure 4.4b, the area labeled as “AR01” is where the inductor is placed and “AR02” is where an aluminum support plate is placed as a control group to measure temperature. While the converter is running, a fan running on 6 volts blows over the inductor to prevent overheating. For the

measurements, the converter is run for 20 seconds at a given setpoint and then turned off for about a minute to cool down. Then, the current set point is increased and test. By repeating these steps, the performance of the converter is measured as the inductor heats up. The whole data series is presented in Figure 4.5. A more detailed experimental setup can be found in the experimental section of this chapter.

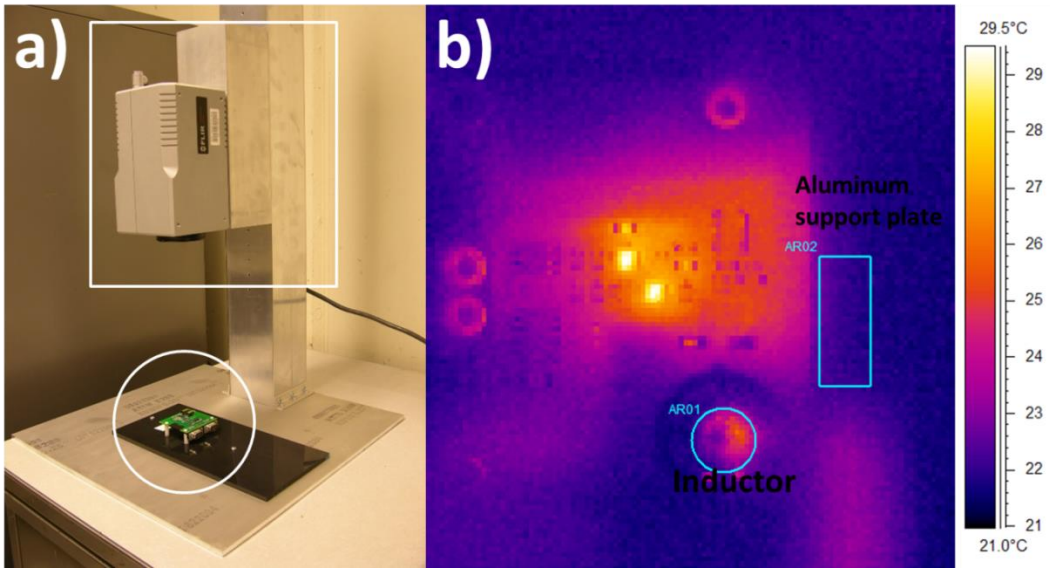

Figure 4.4. a) A photograph of the experimental setup to measure the temperature of a power converter. The component in the white circle is the power converter; the component in the white squares is the infrared (IR) b) The image from the IR camera. The white circle indicates the position of the inductor with NC core and the white square is an aluminum support plate.

As can be observed in Figure 4.5, the temperature is not directly increased from room temperature to ~ 170 °C, but the maximum temperature of the each 20 second run cycle is raised by slowly increasing the setpoint current or output power. Therefore, there are three variables: temperature, efficiency, and output power. From each 20 second cycle, the efficiency and output power of the power converter with the same range of the inductor temperature are collected. For example, in all cycles, there are data points whose temperatures are in between 70 and 80 °C but with different output powers and efficiencies. I collect all the output power and efficiency data, make an output power vs efficiency plot and compare it with data collected in the same way but in different temperature ranges.

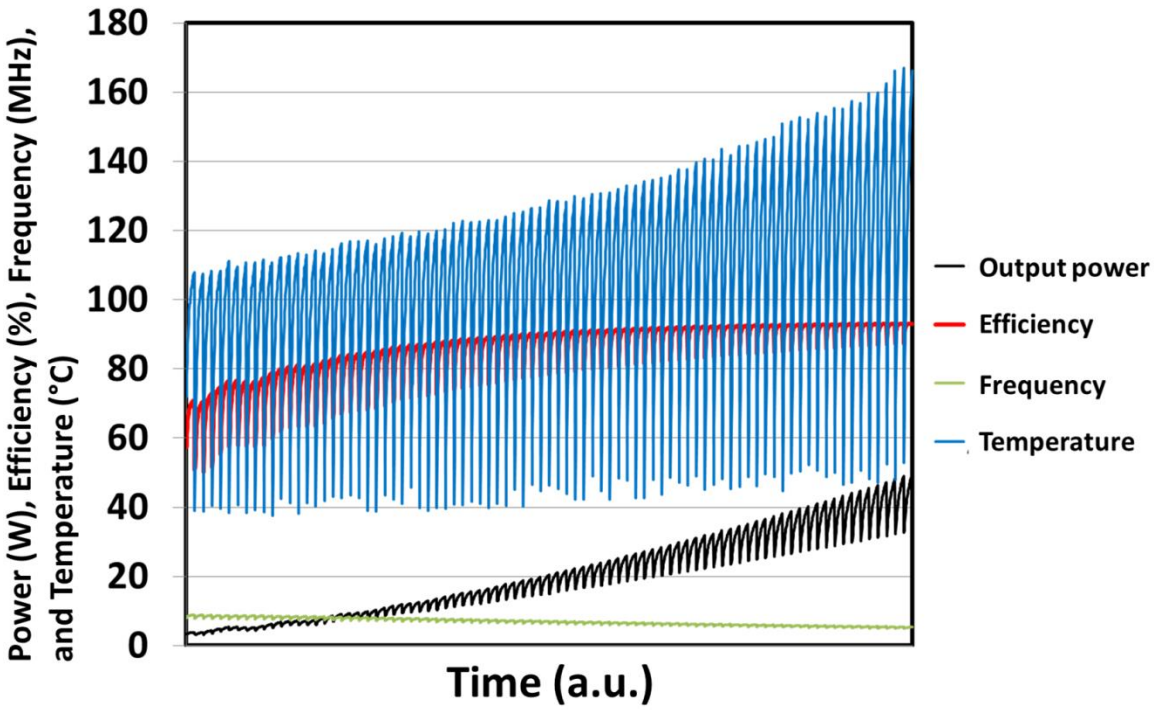

Figure 4.5. The whole data series collected from a power converter.

The output power vs efficiency curves are extracted in Figure 4.6 as described in the previous paragraph. In Figure 4.6a, the curves are plotted in the temperature range from 50 °C to 160 °C. In general, the energy efficiency of the power converter is increasing as the temperature increases. To see a clear temperature dependence, the enlarged image of 4.6a at high output power and temperature is displayed in 4.6b. These curves show that the efficiency increases as the temperature rises and then starts merging at 130-140 °C to its maximum value. From 130 – 160 °C, the output power vs efficiency curves (yellow, orange, and red curves) are nicely superimposed to each other and the efficiency reaches to its maximum value, 93 %, at 47.9 watt and 153.9 °C. Even though the

temperature could not be raised further due to the possibility of burning off the inductor, our observation clearly demonstrates that the power efficiency is highly related to the temperature of the inductor with NC core. This temperature dependent efficiency can be partially attributed to the fact that the thermal relaxation of NCs is strongly dependent on temperature. As can be observed from the ZFC curve in Figure 4.7a, at above $T_{B,}$ the magnetic moments of NCs decrease steadily with temperature at a given field (0.01 T). For example, the relative magnetic moments at 370 K are 74.4 % of the moments at 310 K. In Figure 4.7b, the M_s difference is not as huge as the case of small fields. Still, M_s decreases as temperature increases and the M_s at 370 K is 93.6 % of M_s at 310 K. These two observations are the proofs of faster magnetic relaxation at higher temperature.

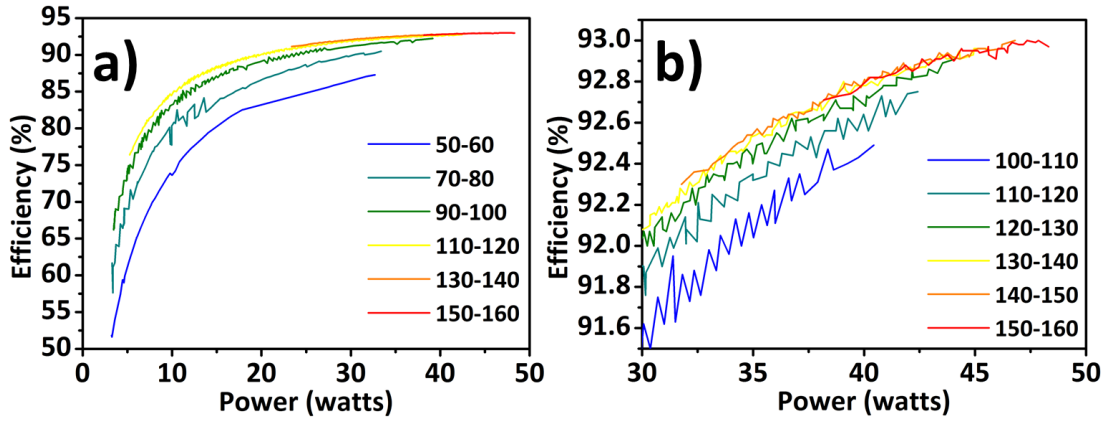

Figure 4.6. a) Temperature dependent efficiency curves vs output power. b) The temperature dependent output power vs efficiency curves at high output power and efficiency.

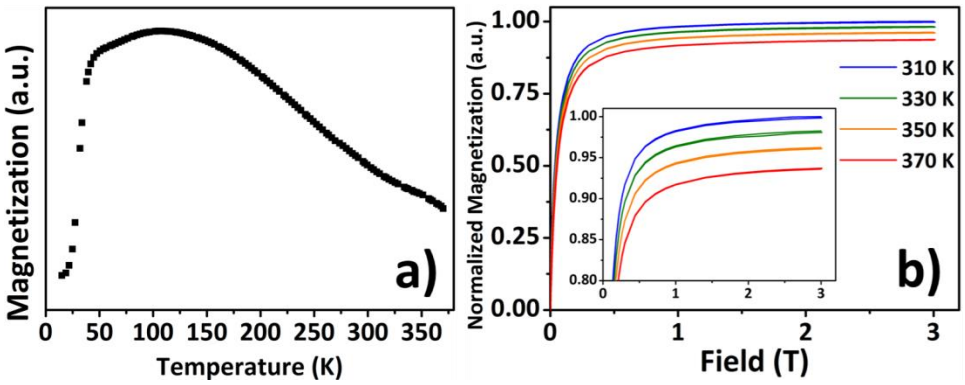

Figure 4.7. a) ZFC curves of $Zn_{0.27}Fe_{2.73}O_4$ NCs from 15 K to 370 K. b) Hysteresis curves of $Zn_{0.27}Fe_{2.73}O_4$ NCs at 310 (blue), 330 (green), 350 (yellow), and 370 K (red).

This is not the same case in two types of inductors: air core inductor and commercial core inductor. Figure 4.8 shows the output power vs efficiency curves of an air core inductor and a commercial ferrite core inductor. The commercial core is a T20-2 iron powder toroid purchased from Coilcraft. In both cases, the power efficiencies drop as the temperature increases. In the temperature range from 20 °C to 30 °C, the efficiency of the air core inductor is ~ 90 % and reduces to 88.6 % in the temperature range from 100 °C to 110 °C at similar output powers. The main reason of the power efficiency drop can be attributed to the fact that the resistance of the inductor winding increases as the temperature increases. Especially, the air core inductor has a longer winding length to keep the inductance level similar to those of the other inductors (NC core and commercial ferrite core). Due to the high resistive loss of the air core

inductor, the power efficiency is less than those of the NC core inductor and commercial ferrite core inductor even without the magnetic core material. On the other hand, the power efficiency of the commercial ferrite core inductor also decreases as the temperature increases, though the power efficiency is still higher by ~1.2 % at the highest temperature range (150 °C – 160 °C) than that of the NC core inductor. We do not have clear understanding about this phenomenon yet, but it is still worth investigating the temperature dependence of the power efficiency further and improving the NC properties to exceed the efficiency of the current state-of-the-art materials.

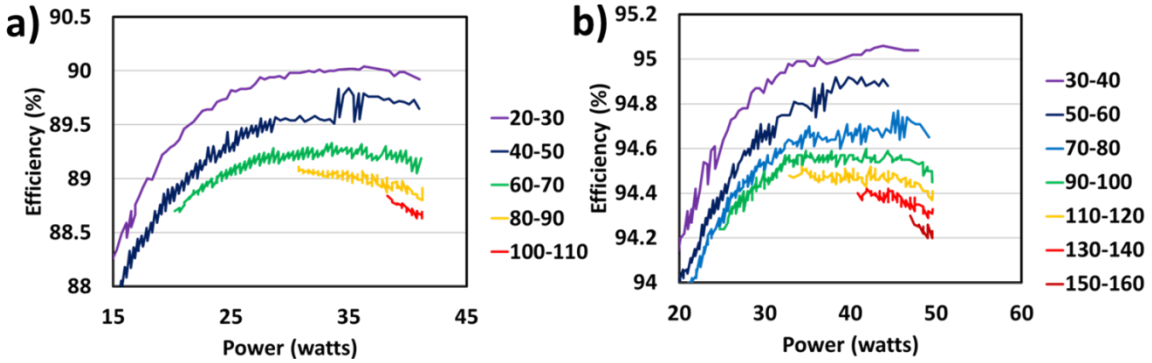

Figure 4.8. The efficiency curves vs output power of a) air core inductor and b) commercial ferrite core inductor.

4.4 Conclusion

In this chapter, I have discussed the temperature dependent energy efficiency of a power converter with an inductor with a NC core. It is observed that the energy efficiency is strongly correlated to the temperature of the inductor. It increases as the temperature increases and reaches to the maximum efficiency with 93 % in the range from 130 °C to 160 °C. The comparison with an air core inductor and a commercial core inductor with similar values of inductance indicates that the magnetic dynamics of the NCs at high temperature is significantly different from that of the commercial ferrites. In contrast to the temperature dependence of the inductor with NC core, the power efficiency of the air core inductor and commercial core inductor reduce from 90 and 95 % to 88.6 and 94.2 %, respectively, as the temperature rises. Still, the power efficiency of the commercial core inductor is about 1.2 % higher than that of the NC core inductor. Further investigation on the AC magnetic properties of NCs might offer improvement in their energy efficiency at high temperature.

4.5 Experimental Section

4.5.1. Synthesis of $Zn_{0.27}Fe_{2.73}O_4$ NCs. To prepare 9.5 nm $Zn_{0.27}Fe_{2.73}O_4$ NCs, 4 mmol of iron (III) acetylacetonate, 1 mmol of zinc (II) acetylacetonate, 10.6 mL of oleic acid, 12.8 mL of oleylamine are mixed in a 125 mL flask. The mixture is

kept at 100 °C under vacuum for an hour. Then, the mixture is rapidly heated to 295 °C. After 30 mins, the reaction mixture is cooled down to room temperature and NCs are precipitated out by adding 50 mL of ethanol. After centrifugation, the supernatant is removed and the precipitation is re-dispersed into hexane. The NC solution is further washed with ethanol two more times and then re-dispersed back to hexane. The ratio between zinc and iron is determined by Inductively Coupled Plasma Optical Emission Spectroscopy (ICP-OES).

4.5.2. Temperature dependent efficiency measurements. To test the temperature dependence of the power efficiency of an electronic circuit with a hand-wound inductor, an IR camera is used. The setup is presented in Figure 4.4a and the view from the IR camera is in Figure 4.4b. The area labeled as AR01 is where the inductor is placed; the area labeled AR02 is where an aluminum support plate is placed as control groups to measure temperature. The inductor is painted in black and the aluminum support plate is covered with white electrical tape. At IR wavelengths, white and black tape have the same emissivity. The temperature is recorded while the converter is running. While the converter is running, a fan running on 6 volts blows over the inductor to prevent overheating which can burn off the inductor. The converter is run for 20 seconds at each current setpoint and then turned off for about a minute to cool down. Then, the current setpoint is increased and the test is repeated. By repeating the

steps, the performance of the converters could be measured as the inductor heated up. Air-core and commercial core inductors are also characterized in the same way.

Please refer chapter 2.7.8 for the experimental procedure of a NC core inductor preparation.

CHAPTER 5. Hydrodeoxygenation Reaction of DMF by Bimetallic Nanocrystals under a Continuous Flow Reactor (Collaborated with Jing Luo)

5.1 Introduction

5-Hydroxymethylfurfural (HMF) is a key platform chemical in biomass conversion.[50,53] It is readily obtained by the acid-catalyzed dehydration of C-6 sugars (e.g, glucose, fructose) but its high oxygen content precludes its direct use as a fuel. One promising approach to stabilize HMF is the selective HDO to form 2,5-dimethylfuran (DMF). A relatively small amount of hydrogen is consumed in the formation of DMF and DMF can be used directly as fuel due to its high energy density and octane rating. DMF can also undergo Diels-Alder reaction with ethylene and be converted to p-xylene, an important precursor of terephthalic acid.[188,189]

The reaction of HMF to DMF has been studied extensively over various metal and metal-alloy catalysts[6,7,53,57,190] but selectivity of DMF over ring-opened and ring-hydrogenated (e.g. dimethyltetrahydrofuran) products is often poor. Bimetallic alloy has an extra degree of freedom for modification of electronic and geometric structure, so that there is a chance to improve the catalytic activity of a catalyst. Recently, Pt_3Co nanoparticles in hollow carbon spheres are reported to have 98 % of selectivity for DMF in a batch reaction,[7] though the study does not

provide good understanding on how cobalt affects the HDO of HMF. PtCo NCs prepared by solvothermal methods have been extensively studied for catalysis[5,191,192] and ultra-high density magnetic recordings.[2,193,194] The solvothermal method can easily control the size, morphology, and composition of NCs. These parameters are strongly correlated to their catalytic properties.[29,38] Therefore, this synthetic technique enables us to design and optimize the properties of materials by understanding how the different variables of the materials affect their catalytic activities.

In chapter 5, the HDO of HMF into DMF catalyzed by Pt, Pt_3Co, and Pt_3Co_2 NCs is presented. The reactions are performed *via* continuous flow reactor.[6] The NCs are synthesized by solvothermal method and the compositions of NCs are controlled to clarify the composition dependent catalytic activity of NCs. The catalytic behavior of bimetallic NCs with other composition including PtMn, PtFe, and PtNi is also discussed.

5.2 Synthesis of bimetallic NCs

Nearly monodisperse Pt, Pt_3Co, and Pt_3Co_2 NCs are synthesized by following either literature procedures or modifying them according to specific goals (See experimental section).[2,29] For platinum cobalt bimetallic NC synthesis, 1,2-hexadecanediol (HDD) is used to reduce Pt, which is called “polyol process.”[195] On the other hand, for the synthesis of Pt_3Co_2, hexadecylamine is replaced by

oleylamine and HDD is not added. After the injection of $Co_2(CO)_8$ at 170 °C, the reaction vessel is heated to 300 °C and kept for 30 mins. Since oleylamine is a relatively milder reducing agent than HDD,[196] this reaction resulted in relatively cobalt rich NCs as compared to the reaction done through the polyol process. From the TEM images of NCs in Figure 5.1, the average diameters of NCs are found to be 2.5 nm, 3.2 nm, and 3.7 nm, with less than 7 % of size distribution for Pt, Pt_3Co, and Pt_3Co_2 NCs, respectively (Table 5.1). The formation of superlattice structure in each composition of NCs is observed, indicating the high monodispersity of these NCs. WAXS data show that all the NCs possess face-centered cubic (fcc) crystal structure as displayed in Figure 5.1d. Slight shifts of the x-ray peaks are observed due to the replacement of Pt by Co in the lattice structure. A cobalt atom is smaller than a platinum atom and it reduces the d-spacing between the atoms in the crystal, which results in the increase of 2θ as the amount of cobalt increases in the structure.[196] For example, the (111) peak is shifted from 39.85° for Pt NCs to 40.1° and 40.3° for Pt_3Co and Pt_3Co_2, respectively. The compositions of NCs are further confirmed by ICP-OES.

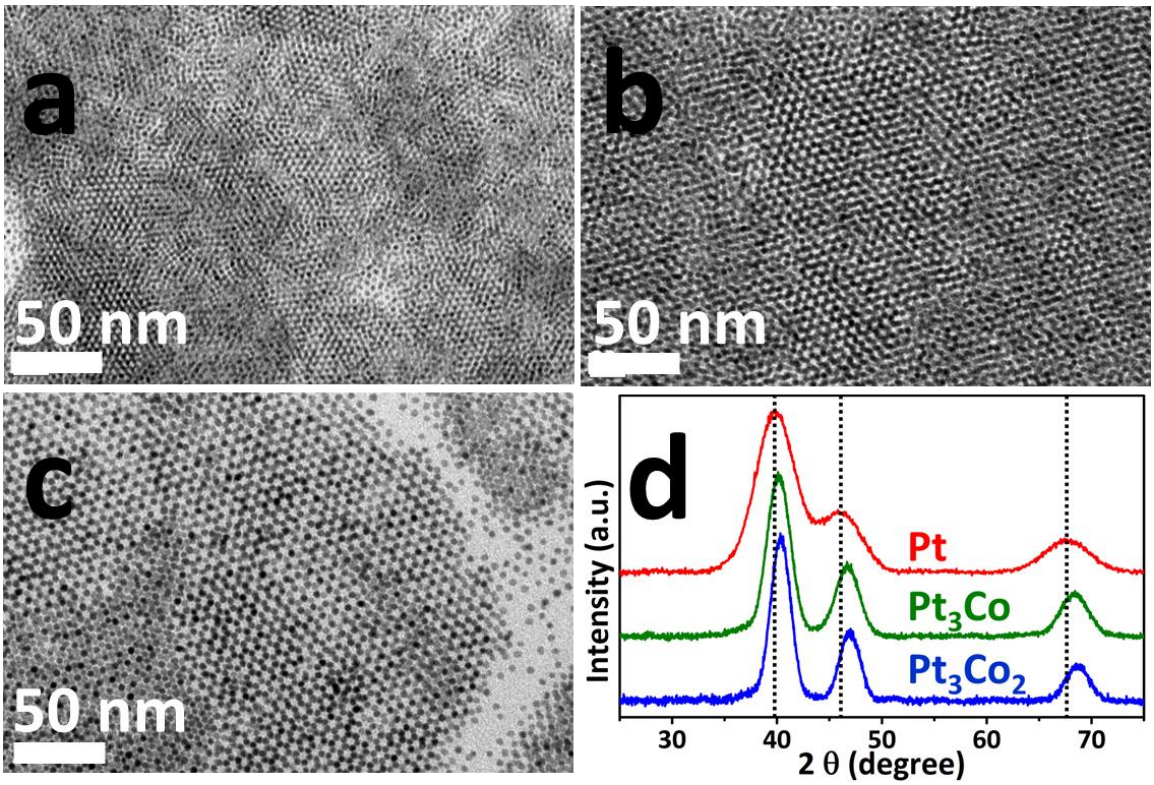

Figure 5.1. The TEM images of a) Pt NCs, b) Pt_3Co NCs, and c) Pt_3Co_2 NCs. d) WAXS data of Pt (red), Pt_3Co (green), and Pt_3Co_2 (blue). The scale bars in the insets represent 2 nm.

Table 5.1. Average sizes and standard deviations NCs determined by TEM images.

Pt	**Pt_3Co**	**Pt_3Co_2**
2.5 nm (6.7 %)	3.2 nm (6.5 %)	3.7 nm (6.9 %)

The NCs are dispersed onan activated carbon support to prepare 10 weight % of metals on carbon (Experimental section). As the colloidal NCs are covered by organic ligands such as oleic acid and oleylamine for colloidal stability, the catalytic reactions are inhibited due to the limited access of reactants to the binding sites on the NC surface. Therefore, the surface ligands should be removed to maximize their available surface area by using plasma and thermal annealing processes. After these treatments (Figure 5.2d-f), no significant change in size and morphology is observed in all the cases of NCs, which proves the reliability of these surface treatment techniques and provide high reproducibility. Also, from WAXS study (Figure 5.3), it is confirmed that the phase of Pt_3Co and Pt_3Co_2 are not transformed from disordered fcc to ordered fct structure. Therefore, we can exclude the potential effects of crystal structure ordering on the catalytic activity and attribute any difference to the compositional effect.[197]

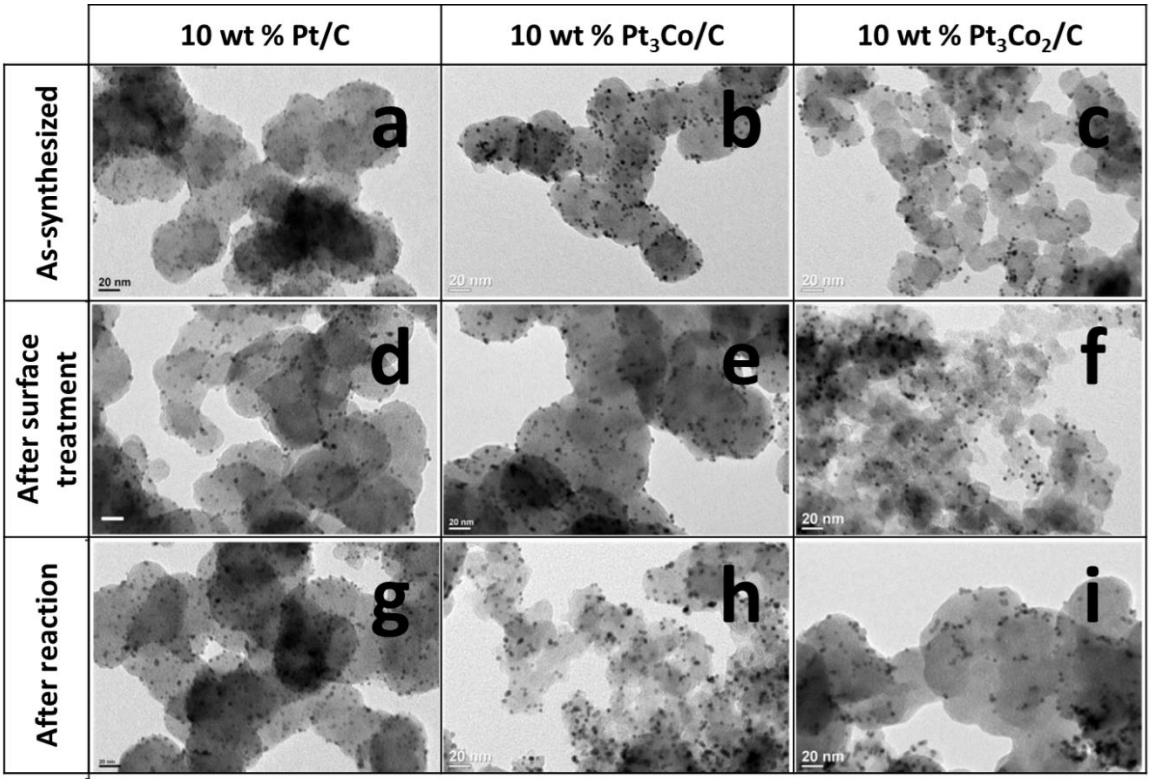

Figure 5.2. The TEM images of (a-c) as-sythesized NC catalyst on carbon support, (d-f) after surface treatment, and (g-i) after reaction. The scale bars represent 50 nm.

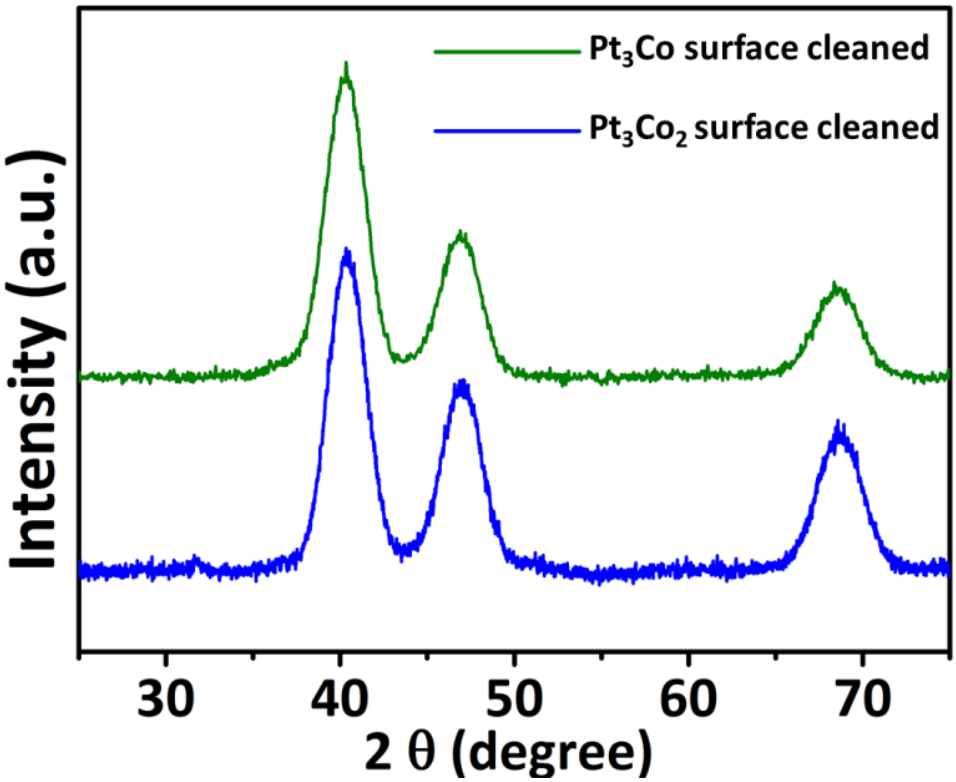

Figure 5.3. WAXS data of Pt_3Co (green line) and Pt_3Co_2 (blue line). after surface cleaning process by plasma treatment and rapid thermal annealing at 500 °C.

5.3 The HDO reactions catalyzed by Pt NCs, and PtCo NCs.

Then, the NC catalysts are tested under a continuous flow reactor following the experimental procedure. Previous studies on carbon-supported Pt and Co catalysts have shown that HDO of HMF to DMF is a series reaction, with reaction proceeding as indicated in Scheme 5.1.[6] The HMF first reacts to a group of partially hydrogenated intermediate compounds, including 5-propoxymethyl-2-furanmethanol, 5-propoxymethyl-2-methylfuran (ether-methyl furan), 5-methyl furfural (MF), 5-methyl-2-furanmethanol (methyl furfuryl alcohol), and 2,5-bis(hydroxymethyl)furan (BHMF). These intermediate compounds can all be converted to DMF, which in turn reacts further to form over-hydrogenated/ring-opened products: dimethyl tetrahydrofuran (DMTHF), 2-hexanone, 2-hexanol, 2,5-hexandione, and their etherification derivatives, 2-propoxy-1-methyl-pentane (2-propoxyhexane) and 1,4-dipropoxy-1,4-dimethyl-butane (2,5-dipropoxyhexane).

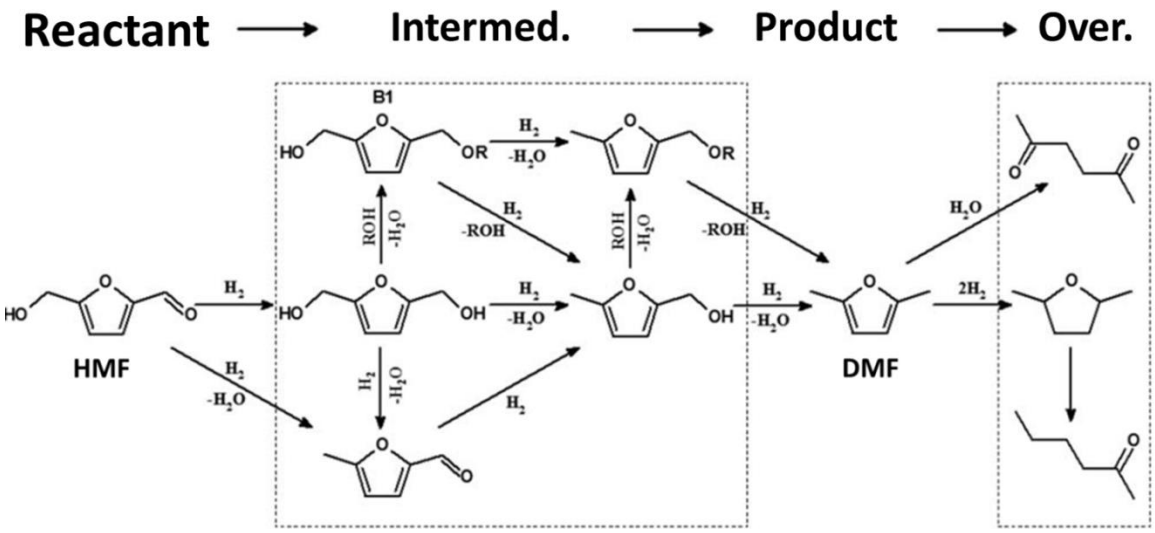

Scheme 5.1. A reaction network scheme for the HDO reaction of HMF. (Adapted from reference 7.) “Intermed.” and “Over.” refer intermediate products and over-reacted products, respectively.

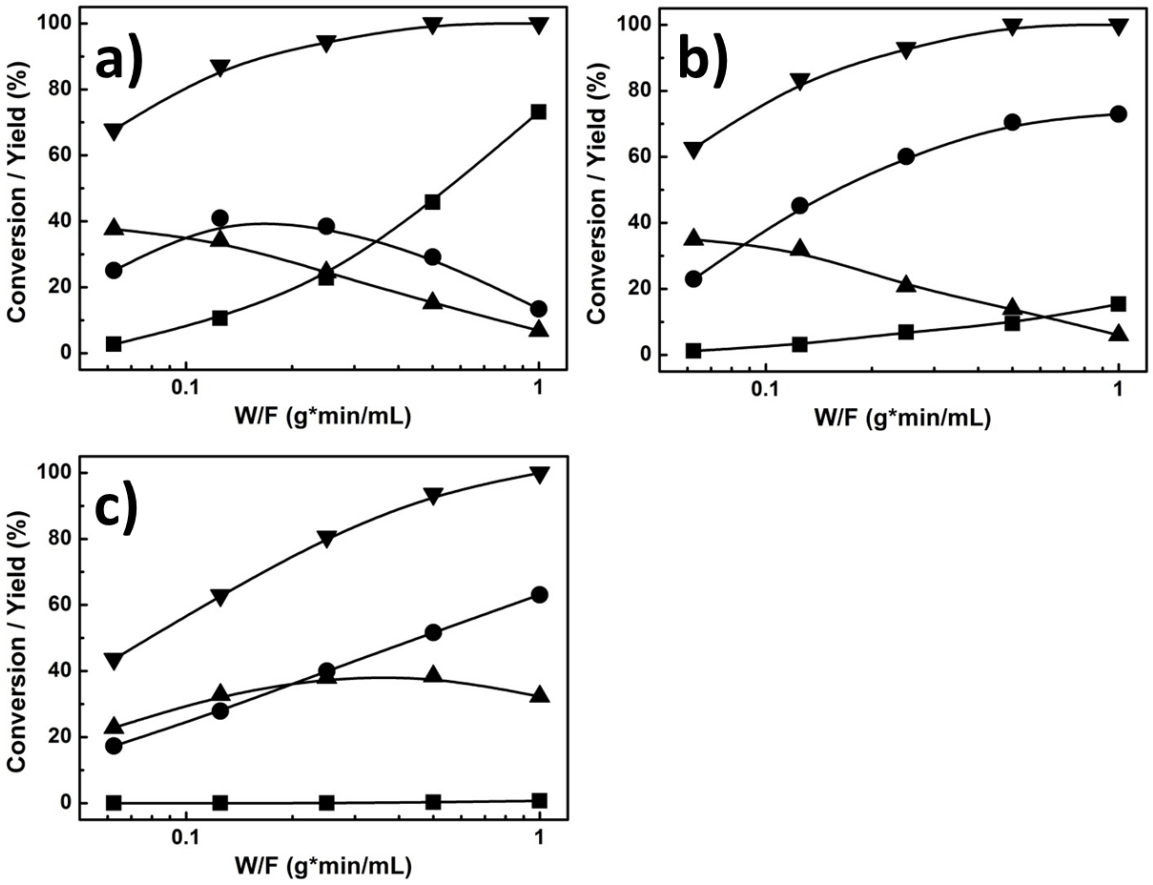

Figure 5.4. Conversion and product distribution for the HDO reaction of HMF over (a) 10-wt% Pt/C, (b) 10-wt% Pt_3Co/C, (c) 10-wt% Pt_3Co_2/C, as a function of reactor space time. Reaction conditions: 33 bar and 120 ºC. (▼) HMF conversion, (▲) Intermediate products, (●) DMF, (■) Overreacted products.

Figure 5.4a, which is the plot of conversion and product yields as a function of space time on the 10-wt% Pt/C catalyst prepared from Pt NCs, shows that Scheme 5.1 also applies to HDO reaction of HMF in this case. Space time is the catalyst weight to flow rate ratio, indicating the relative interaction time between reactants and catalysts. These experiments are carried out at 120°C, a

significantly lower temperature than that used in a previous study with Pt catalysts prepared by infiltration of metal salts,[6] because NC catalysts are much more active. Even for the shortest space time and at this low temperature, the HMF conversion is greater than 65%. Initially, partially hydrogenated products (Intermed.) are formed in the highest yields but they decline steadily with space time (Figure 5.4a). DMF yields initially increase and then decrease, providing strong evidence that these are an intermediate product in a series reaction. The maximum yield is approximately 41%. Over-hydrogenated compounds (Over.) are only formed at higher space times, indicating that they are not primary products. The fact that their formation follows the consumption of DMF strongly suggests they are formed from DMF. A detailed analysis of the partially hydrogenated (B) and over-hydrogenated (D) compounds is given in the Table 5.2.

Table 5.2. Yields of partially hydrogenated compounds over different metal catalysts at a space time of over 10-wt% Pt/C at 120 ºC and 33 bar.

W/F (g·min/mL)	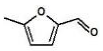	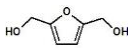	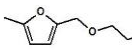	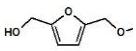	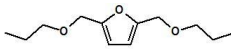
0.0625	1.3	3.7	3.8	25.4	3.4
0.125	1.8	2.8	3.5	21.8	4.2
0.25	0	2.1	2.7	17.0	2.7
0.5	0	1.8	0	13.4	0
1	0	0	0	6.8	0

Similar experiments are performed on the 10 wt-% Pt-Co bimetallic NC catalysts. Data at 120°C and 33 bar are shown in Figures 5.4b and 5.4c. For a given space time, the HMF conversions over the Pt_3Co (Figure 5.4b) are similar to that obtained on the pure Pt NCs. The initial products are again the same partially hydrogenated compounds, B, and these are again converted to DMF at a similar rate. However, on the Pt_3Co catalyst, the DMF yield continues to increase, to a value of 75%; and only relatively small quantities of over-reacted compounds are formed at the longest space times. The activity of the Pt_3Co_2 NC catalyst is noticeably lower than that of the other two samples and 100% conversion of HMF is achieved only at the longest space time. Because of the low activity, the DMF yield is still linearly increasing at the highest space time and the production of over-reacted compounds is negligible, whereas the amount of intermediate products is significantly higher (~ 30 %) than other catalysts (10 % for Pt and 5 % for Pt_3Co), implying that the Pt_3Co_2 NC catalyst is not active enough at 120 °C.

Because of the lower rates on the Pt-Co bimetallic NC catalysts, additional reaction measurements are performed at 160°C and 33 bar in order to determine the evolution of products, with results shown in Figure 5.5. As shown in Figure 5.5a, the HMF conversion is nearly 90% on the Pt_3Co, even at the lowest space time. The intermediate products again decline steadily with space time but DMF yields go through a maximum of about 75% at 160 °C, with over-reacted

products being produced from the DMF. However results for the Pt_3Co_2 sample (Figure 5.5b) show the DMF yields continuing to increase, up to 98%. No significant change of the size and shape of Pt_3Co_2 bimetallic NCs is observed in the TEM images after 4 hours of HDO reaction at 160 °C, proving the stability of the NCs (Figure 5.2g-i).

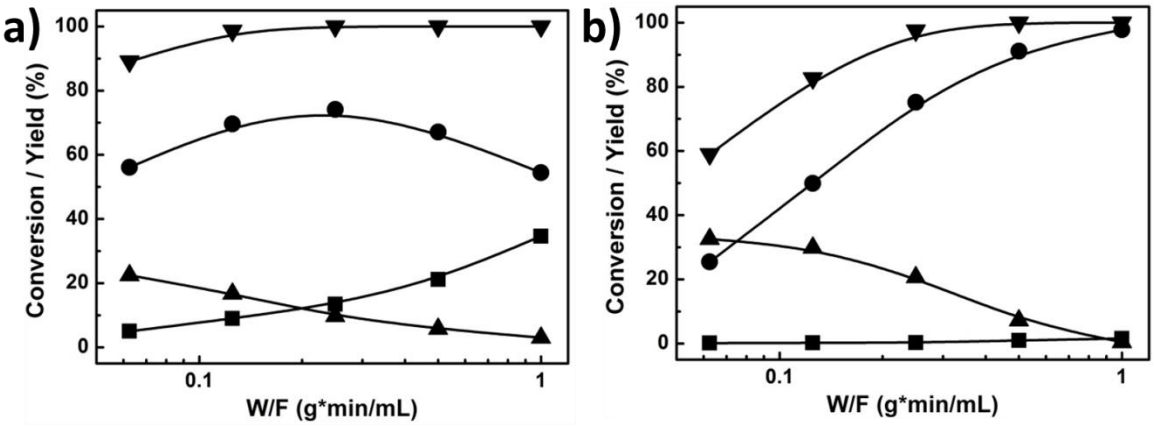

Figure 5.5. Conversion and product distribution for the HDO reaction of HMF over (a) 10-wt% Pt-Co/C with Pt:Co molar ratio 3:1, (b) 10-wt% Pt-Co/C with Pt:Co molar ratio 3:2, as a function of reactor space time. Reaction conditions: 33 bar and 160 ºC. (▼) HMF conversion, (▲) intermed., (●) DMF, (■) over..

The results in Figures 5.4 and 5.5 strongly suggest that the Co alloying with Pt has a modest effect on HDO rates for HMF but strongly suppresses DMF reactions. To investigate this in more detail, the reaction of DMF on the same three catalysts is examined, with conversions and product distributions shown in

Figure 5.6. The reactions are again carried out at 120 °C and 160 °C and 33 bar, using 1-propanol solutions with the same DMF molarity as that used in the HMF experiments. Since water is formed in the reaction of HMF, these experiments do not perfectly mimic the sequential reaction found in HMF; however, some water is also formed in the DMF reaction measurements by dehydration of the alcohols to form di-propyl ether. In Figure 5.6a, DMF is converted rapidly on Pt/C, even at 120°C. The main products are the open-ring ketones and ethers, the products that are also formed at high space times for the reaction of HMF (Figure 5.7a). Because of the lower reactivity of the PtCo bimetallic NC catalysts, measurements on these two samples are carried out at 160°C. Even at this higher temperature, DMF conversions on the Pt_3Co sample are lower than those observed on the Pt catalyst, although still significant (Figure 5.6b). The products on the Pt_3Co catalyst are essentially the same as that observed on Pt. However, the conversion of DMF on the Pt_3Co_2 sample at 160°C, shown in Figure 5.6c, are very low for all space times, reaching a value of only 10% at a space time of 1.0 g•min/mL.

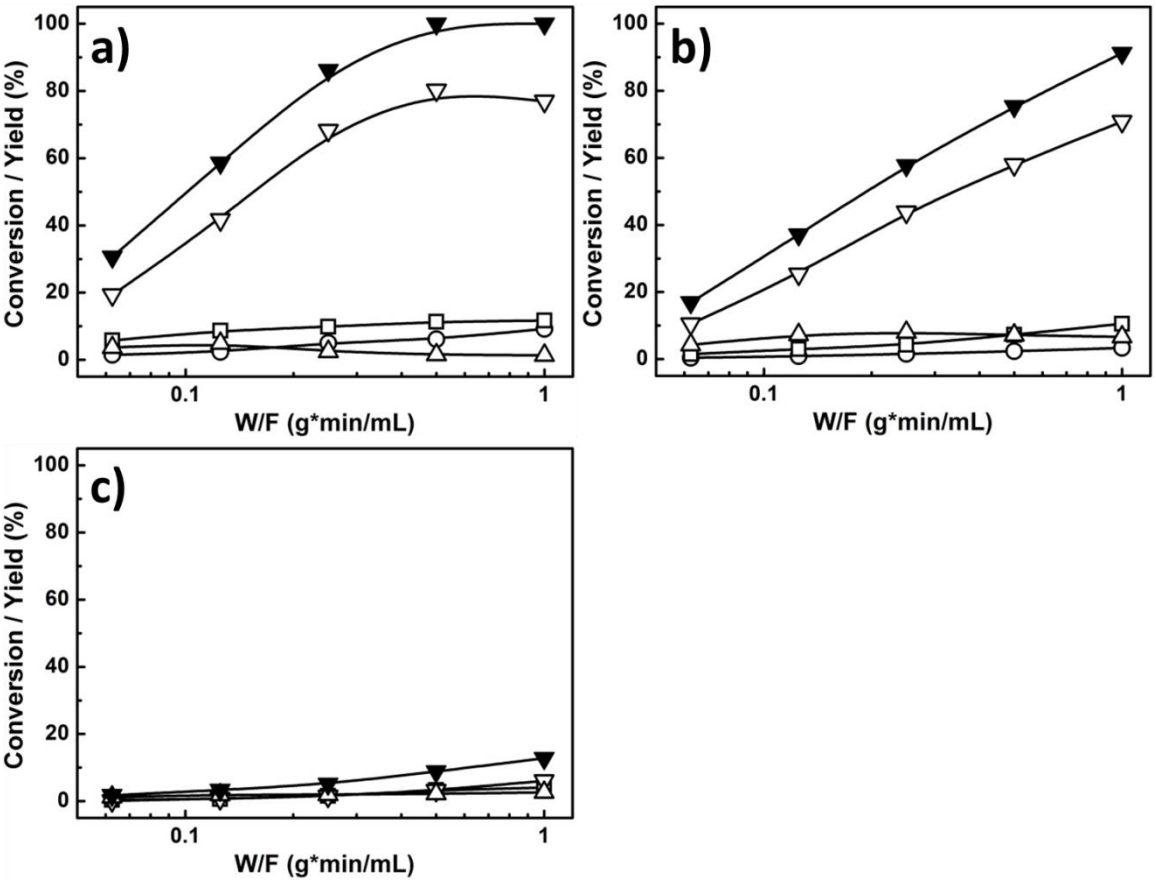

Figure 5.6. Conversion and product distribution for the reaction of DMF as a function of space time at 33 bar: (a) 10-wt% Pt/C at 120 ºC; (b) 10-wt% Pt_3Co NCs/C at 160 ºC, (c) 10-wt% Pt_3Co_2 NCs/C at 160 ºC. (▼) DMF conversion, (□) DMTHF, (▽) 2-hexanone, 2-hexanol and 2-propoxyhexane, (△) 2,5-hexandione, 2,5-dipropoxyhexane, (○) hexane.

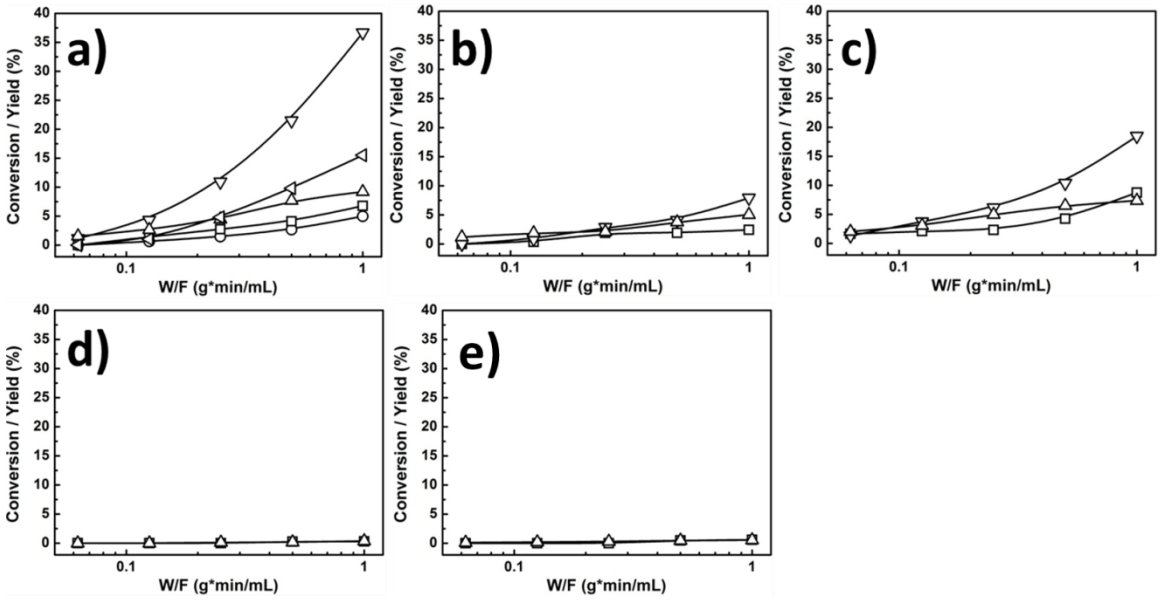

Figure 5.7. Over-reacted product distribution as a function of space time at 33 bar: (a) 10-wt% Pt/C, (b) 10-wt% Pt_3Co NCs/C, (c) 10-wt% Pt_3Co_2 NCs/C, at at 120 ºC; (d) 10-wt% Pt_3Co NCs/C, (e) 10-wt% Pt_3Co_2 NCs/C, at 160 ºC. (□) DMTHF, (▽) 2-hexanone, 2-hexanol and 2-propoxyhexane, (△) 2,5-hexandione, 2,5-dipropoxyhexane, (○) hexane, (◁) unidentified.

Understanding the sequential properties of the HMF HDO is very important to develop the strategy to improve catalytic material and process for high DMF yield. Typically, the formation of secondary products has often been regarded as parallel reactions, so that the goal is to turn off these side reactions. However, for a sequential reaction, HMF → Intermediate → DMF → Over-reacted Product, with DMF as the desired products, the maximum selectivity for DMF is decided by the formation rate from intermediate to DMF and the consumption rate from DMF to over-reacted products. In order to achieve high yield of DMF, the key is

to optimize the reaction conditions (reaction time, temperature, pressure) and choose good catalytic materials. The successful achievement of 98% DMF yield in the present study is indeed following these points. First of all, we identify a good catalytic material, PtCo alloy, which has been demonstrated by both experiment that it is unreactive for DMF. Even though the addition of cobalt composition also decreases the HDO rate of HMF a bit, such effect is not as significant as on DMF over-hydrogenation. Second, we optimize the reaction temperature and space time that is most selective for DMF. Due to the decrease of HDO rate after introducing cobalt component, a higher reaction temperature is preferred to convert HMF and intermediates to DMF. However, the trade-off is increased over-hydrogenation products, as shown from the results of Pt_3Co at 160°C. So choosing a temperature with best relative rate of HDO to over-hydrogenation is critical.

From the data, it can be deduced that the PtCo NCs have a higher energy barrier for DMF over-hydrogenation, thus it is highly selective for DMF in HMF HDO. One critical issue with the alloy studied is that the structure and composition of the catalyst particle must be well-controlled. In this study, the thermal decomposition method is used to precisely control the size and metal composition for each PtCo NCs, so that the composition effect on the performance of HDO reaction can be investigated. For the PtCo catalyst prepared by incipient wetness impregnation method, the particles are not well-

controlled. In this sample, both large chunks and small particles can be observed, and the Pt to Co ratio might vary from one particle to another. It could be inferred that the local HDO reaction may also differ over different particles. The HDO of HMF over impregnated Pt-Co (1:3) catalyst is shown in Figure 5.8. Even though the overall cobalt composition is significantly higher than the Pt_3Co_2 NCs, the maximum selectivity for DMF obtained from this sample is less than 80%.

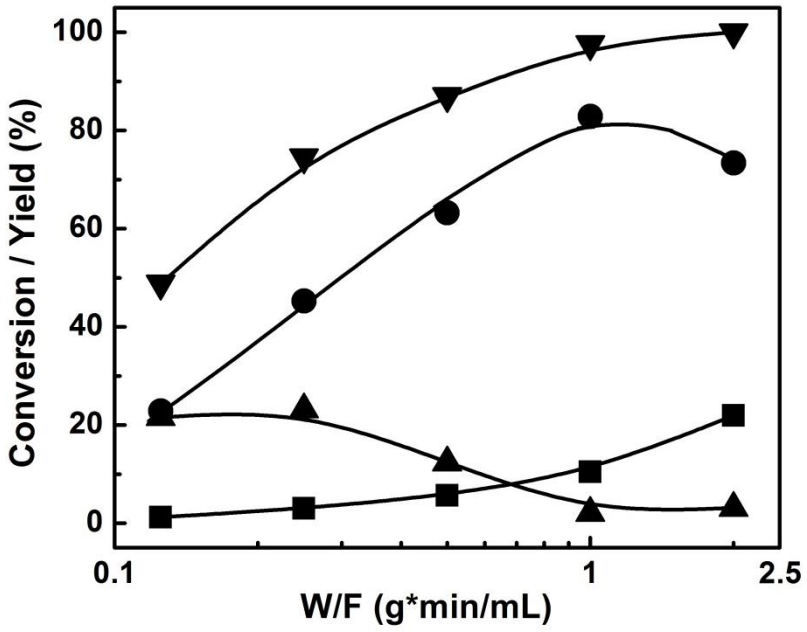

Figure 5.8. Conversion and product distribution for the HDO reaction of HMF over impregnated 10-wt% Pt-Co/C with Pt:Co molar ratio 1:3, as a function of reactor space time. Reaction conditions: 33 bar and 180 ºC. (▼) HMF conversion, (▲) intermed., (●) DMF, (■) over..

5.4 HDO reaction of DMF with PtM (M=Mn, Fe, Co, and Ni)

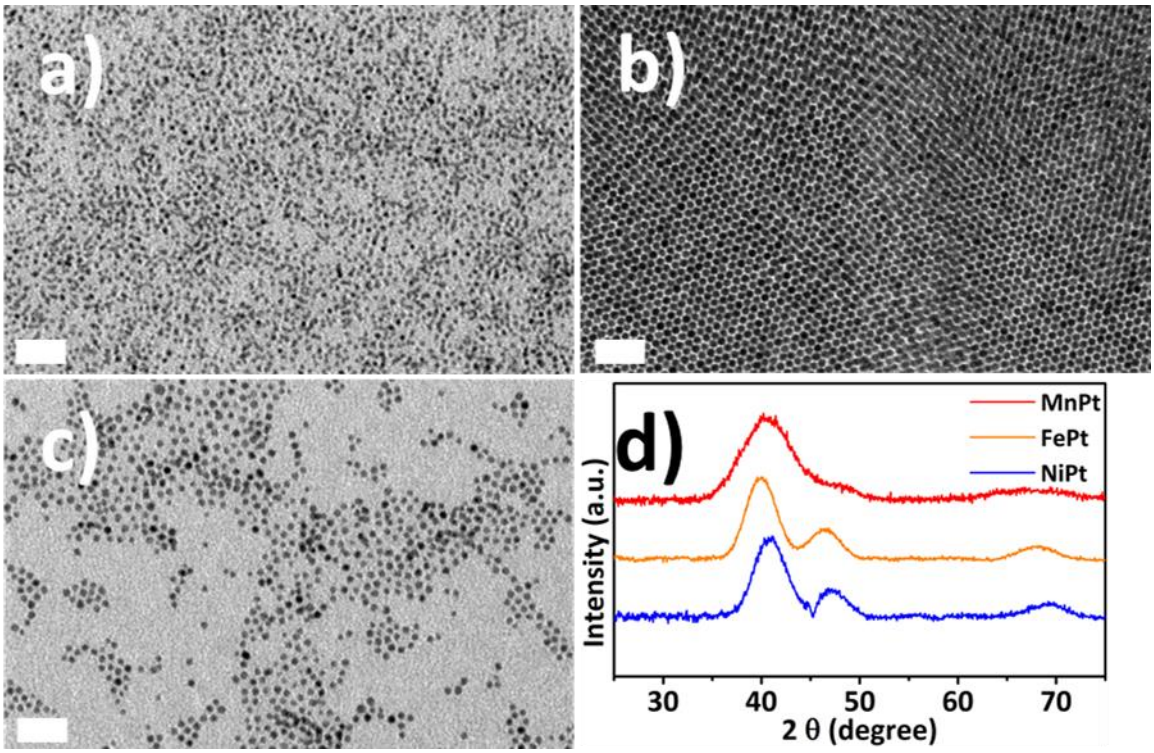

Figure 5.9. TEM images of a) $Pt_{88}Mn_{12}$, b) $Pt_{52}Fe_{48}$, and c) $Pt_{88}Ni_{12}$. d) WAXS data of $Pt_{88}Mn_{12}$ (red), $Pt_{52}Fe_{48}$ (orange), and $Pt_{88}Ni_{12}$ (blue).

In this section, the catalytic activities for the HDO reaction of DMF into HMF *via* other types of platinum based alloys, including PtMn, PtFe, and PtNi are discussed. In Figure 5.9, the TEM images of PtMn, PtFe, and PtNi and their WAXS data are presented. The NC sizes of each composition are measured to be close to each other: 1.7 nm of $Pt_{88}Mn_{12}$, 3.0 nm of $Pt_{52}Fe_{48}$, and 2.2 nm of $Pt_{88}Ni_{12}$. All the NCs possess fcc structure and the shift of (111) peak from 39.85° indicates that the NCs are alloys. These NCs are deposited on the carbon

support to yield 10 wt % PtM NCs/C catalysts and gone through the surface cleaning process. The composition ratio is determined by ICP-OES.

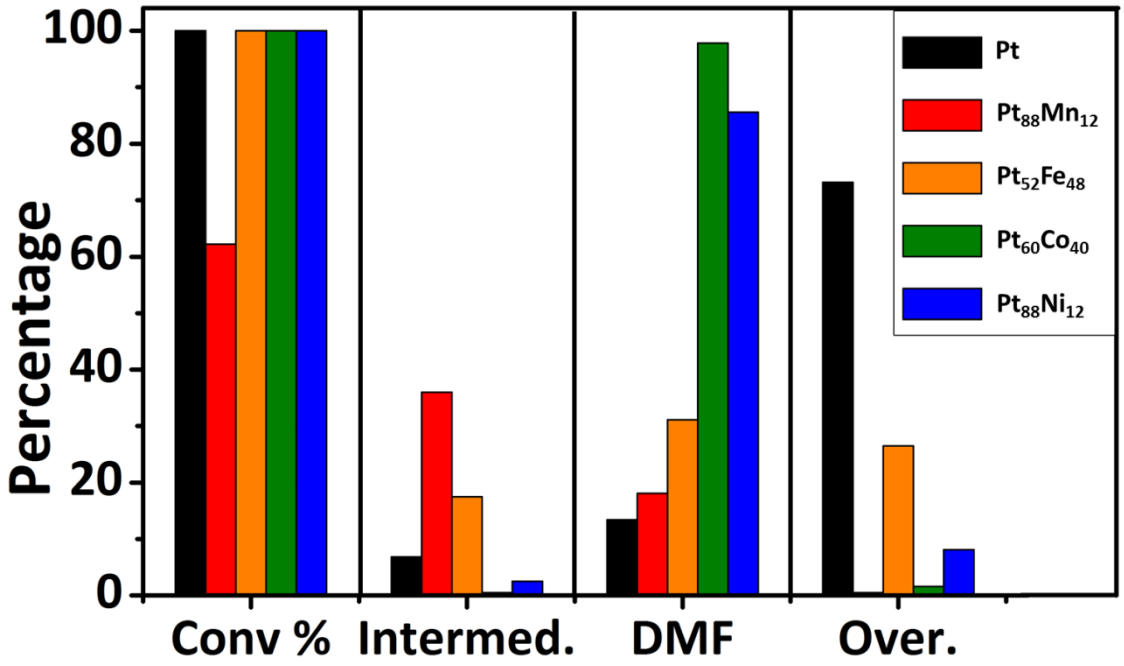

Figure 5.10. The HDO reaction of HMF into DMF results from Pt (black), $Pt_{88}Mn_{12}$ (red), $Pt_{52}Fe_{48}$ (orange), $Pt_{60}Co_{40}$ (green), and $Pt_{88}Ni_{12}$ (blue). "Intermed." and "Over." refer intermediates and over-reacted products, respectively. The reaction with Pt NC catalyst is performed at 120 °C.

The HDO activities of these catalysts are summarized in Figure 5.10 and Table 3.3. For comparison, Pt NC and $Pt_{60}Co_{40}$ NC catalyst data are also included. Please note that the reaction with 10 wt % Pt NCs/C is performed at 120 °C instead of 160 °C due to the deactivation of Pt NCs at 160 °C. From the

experiments, clear dependence of HDO activity on the metal composition is observed. In terms of the conversion ratio, all NCs show 100 % conversion except $Pt_{88}Mn_{12}$ NCs with 62.2 %. The presence of 12 % of Mn in the NCs dropped more than 1/3 of the catalytic activity compared to Pt NCs. This low catalytic activity of $Pt_{88}Mn_{12}$ is found again in the selectivity for the intermediate products of the reaction. The low catalytic activity of platinum manganese leaves many products in the intermediate stage (36 %) and these could not turned into the desired product (DMF) and the selectivity for DMF is only 18.1 %. The fact that the overhydrogenated/ring-opened product is detected only less than 0.5 % is in agreement with the low activity of $Pt_{88}Mn_{12}$ as well.

In case of $Pt_{52}Fe_{48}$ NCs, they possess higher selectivity for DMF than Pt and $Pt_{88}Mn_{12}$ NCs with 31.1 %, but the value is significantly smaller than that of $Pt_{60}Co_{40}$ or $Pt_{88}Ni_{12}$ NCs. The amount of intermediate is ~11 % higher than that of Pt NCs, but the overhydrogenation and ring-opening processes are suppressed, leading to its higher selectivity for DMF than Pt. However, the amount of intermediate products and over-reacted products are still much higher than those of $Pt_{60}Co_{40}$ and $Pt_{88}Ni_{12}$. $Pt_{88}Ni_{12}$ NCs show the highest selectivity (85.6 %) for DMF except $Pt_{60}Co_{40}$ NCs. Just like the catalytic activity of $Pt_{60}Co_{40}$ NCs discussed previously, $Pt_{88}Ni_{12}$ NCs have a high catalytic activity which can be proven by the 100 % conversion ratio and small amount (2.5 %) of intermediate products. It is worth noting, that even though the composition ratios

are not the same, that the selectivity has a clear trend:as the atomic number increases from Mn to Ni, the selectivity reaches its maximum with cobalt and then start decreasing.

Table 5.3. HDO reaction of HMF into DMF catalyzed by NC catalyst.

Catalyst	Conv%	Intermed.	DMF	Over.
$Pt_{60}Co_{40}$	100	<0.5	97.8	1.6
$Pt_{88}Ni_{12}$	100	2.5	85.6	8.1
$Pt_{52}Fe_{48}$	100	17.5	31.1	26.5
$Pt_{88}Mn_{12}$	62.2	36.0	18.1	<0.5
Pt*	100	6.8	13.4	73.2

*the reaction was performed at 120 °C

To analyze the overhydrogenation/ring-opening processes of each NC catalyst, the composition ratio of the over-reacted products are summarized in Figure 5.11 and Table 5.4. The composition ratio of over-reacted products indicates apparent differences from one catalyst to another. For example, $Pt_{52}Fe_{48}$ NCs yield the largest amount of side product 2-hexanol with 16.6 %, whereas $Pt_{88}Ni_{12}$ NCs produce the largest amount of 2,5-hexanedione with 4.4%. However, in the case of $Pt_{88}Ni_{12}$, considering the fact that 2,5-dipropoxy hexane should be come from 2,5-hexadione, Pt NCs should have produced more amount of 2,5-hexanedione. As mentioned, $Pt_{88}Mn_{12}$ NCs do not show over-reacted products due to their low catalytic conversion. It is observed that the ring opening process is suppressed in all the bimetallic NCs, resulting in less DMTHF

formation than Pt NCs. In $Pt_{52}Fe_{48}$ NCs, more ring-opened products are observed than PtNi and PtCo, suggesting the role of Fe, Co, and Ni in this catalytic reaction. Even though the composition ratio between the 3d element and Pt in these bimetallic NCs are not controlled so that the direct comparison is not easy, this work suggests that there is an opportunity to further increase/improve the catalytic behavior of colloidal NCs by understanding the catalytic role of 3d elements. For this, further investigation on the HDO activity of bimetallic NCs with more precisely controlled size and composition is necessary.

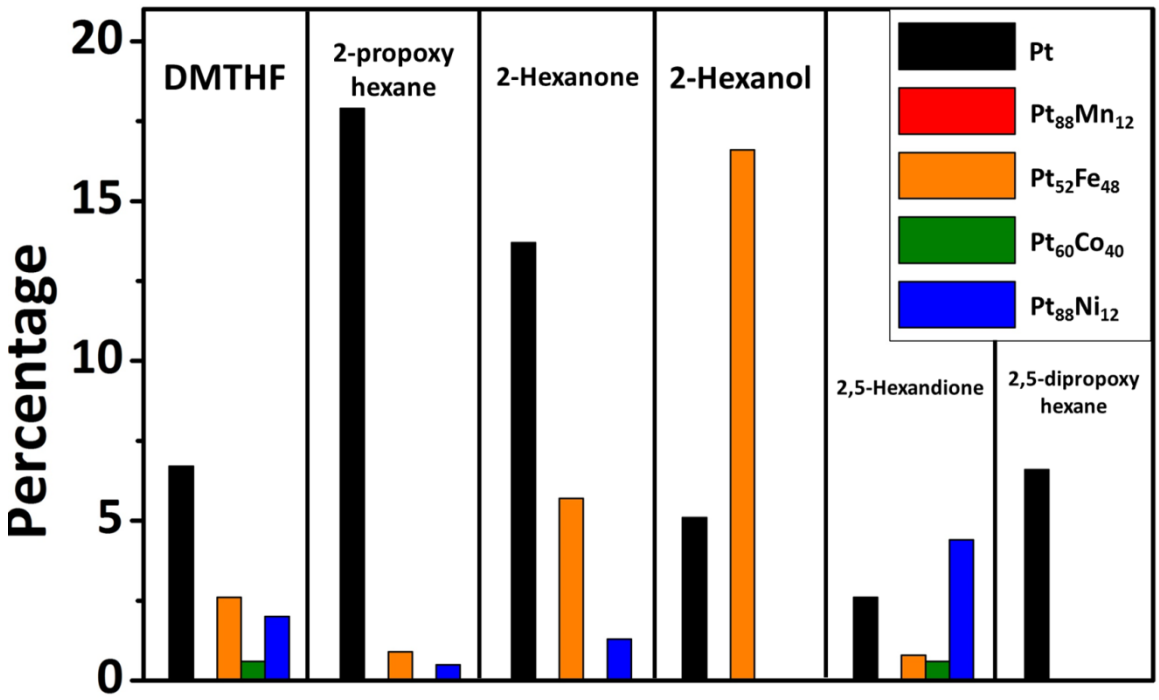

Figure 5.11. The composition of the overhydrogenated/ring-opened products from Pt (black), $Pt_{88}Mn_{12}$ (red), $Pt_{52}Fe_{48}$ (orange), $Pt_{60}Co_{40}$ (green), and $Pt_{88}Ni_{12}$ (blue). The reaction with Pt NC catalyst is performed at 120 °C.

Table 5.4. The composition of the overhydrogenated/ring-opened products

Catalyst	DMTHF	2-propoxy hexane	2-hexanone	2-hexanol	2,5-hexandione	2,5-dipropoxy hexane
$Pt_{60}Co_{40}$	0.6	0	0	0	0.6	0
$Pt_{88}Ni_{12}$	2.0	<0.5	1.3	0	4.4	0
$Pt_{52}Fe_{48}$	2.6	0.9	5.7	16.6	0.8	0
$Pt_{88}Mn_{12}$	0	0	0	0	0	0
Pt*	6.7	17.9	13.7	5.1	2.6	6.6

*the reaction was performed at 120 °C

5.5 Conclusion

High selectivity of DMF from liquid-phase HDO of HMF with H_2 can be achieved over a well-controlled PtCo NCs/C catalyst. The fundamental principle for the superior performance of PtCo is that bimetallic alloy has higher energy barrier for over-hydrogenation of DMF to secondary by-products. Particularly, with Pt_3Co_2 NC catalyst, 98% of DMF yield was obtained with the optimized reaction temperature and space time. Recognizing the sequential nature of the HMF HDO reaction is the key for catalyst-development strategies. The HDO study on the other bimetallic NCs such as PtMn, PtFe, and PtNi suggest that the reaction route can be varied depending on the choice of 3d metal element incorporated into the Pt NCs. Further optimization on the reaction condition and the material properties will provide better understanding on the HDO reaction *via* colloidal NCs.

5.6 Experimental Section

5.6.1. Metallic NC synthesis and catalyst preparation. Pt NCs are synthesized by modifying a previously reported method.[29] To prepare 2.5 nm Pt NCs, 314 mg of platinum acetylacetonate (Acros, 98%) is dissolved in 40 mL of trioctylamine (Sigma-Aldrich, 97 %), 10.9 mL of oleylamine (Sigma-Aldrich, 70 %), 2.6 mL of oleic acid (Sigma-Aldrich, 90 %), and 0.9 mL of trioctylphosphine (Acros

Organics, 97 %). The reaction mixture is kept under vacuum at 80 °C for 30 minutes and then heated up to 300 °C at a rate of 10 °C/min. After 30 minutes, the reaction mixture cools down to room temperature. Into the reaction mixture, 40 mL of toluene is added. The mixture is divided into 6 centrifuge tubes (50 mL) and 30 mL of isopropanol and 5 mL of ethanol are added. After 2 minutes of centrifugation at 6000 rpm, the supernatant is removed and the precipitate is able to be re-dispersed in hexane or toluene. After washing the excess amount of oleic acid, oleylamine, and trioctylamine by isopropanol, the NCs are dispersed in toluene.

To synthesize 3.2 nm Pt_3Co NCs, I scaled up a method reported by Shevchenko *et al*.[2] 264 mg of platinum acetylacetonate is dissolved in 32 g of hexadecylamine (Acros Organics, 90 %) and 16 mL of diphenyl ether (Sigma-Aldrich, 99 %) in the presence of 672 mg of 1-adamantane carboxylic acid (Acros, 99 %) and 1.04 g of 1,2-hexadecanediol (HDD, Sigma-Aldrich). The reaction mixture is put under vacuum at 80 °C for 30 minutes and then heated at a rate of 10 °C/min. When the temperature reaches to 170 °C, 334 mg of $Co_2(CO)_8$ (Acros, 95 %) dissolved in 3.2 mL of 1,2-dichlorobenzene is injected. The reaction mixture is heated further to 230 °C and kept for 40 minutes. After then, the reaction mixture is allowed to cool down and 50 mL of toluene is injected at 200 °C. When the temperature is cooled down to 90 °C, the reaction mixture is divided into 6 centrifuge tubes (50 mL) and 30 mL of isopropanol,

which is prepared to be warm (~ 50 C°), is added to each centrifuge tube. After 2 minutes of centrifugation at 6000 rpm, the supernatant is removed and the precipitate is easily dispersible in non-polar solvent such as hexane and toluene. After washing the colloid with isopropanol 2-3 times, the NCs are kept in hexane.

For 3.7 nm Pt_3Co_2 NCs, I modifed the reaction method for Pt_3Co NCs. 32 g of hexadecylamine is replaced by 41 mL of oleylamine, 16 mL of diphenyl ether by 16 mL of 1-octadecene (Acros, 90 %), and HDD is not added. After vacuum at 80 °C for 30 minutes, the reaction mixture is heated to 300 °C. At 170 °C, the same amount of $Co_2(CO)_8$ is injected. After 30 minutes at 300 °C, the reaction mixture cools down to room temperature and 50 mL of hexane is added. The other washing process is same as described in the reaction for Pt_3Co NCs.

To prepare NC catalyst, NCs in 20 mL of hexane are mixed with carbon powder (Cabot, Vulcan XC72R) in a 50 mL centrifuge tube by sonication. The metal loading is 10 wt %. After 15 minutes of sonication, the solution is centrifuged at 6000 rpm for 1 minute. The supernatant should be transparent and removed. Then, the powder is washed with 20 mL of isopropanol and centrifuged again. Then, the powder is dried in a vacuum oven for overnight at 50 °C. To increase catalytic activity of NCs, the powder goes through surface cleaning processes. For this purpose, the dry powder is treated with O_2 plasma for 15 minutes. After then, the powder is put into a furnace at 500 °C and taken out after 1 minute.[198] The resulting powder is tested for all the HDO reactions.

5.6.2. Liquid-phase HDO with H_2 in flow reactor. The three-phase reactions are carried out in a continuous flow reactor that has been described in detail elsewhere [ref]. The reactor is a stainless-steel tube, 20-cm long, with a 4.6-mm ID. In most cases, 0.05 g of catalyst is packed into the middle portion of the tube and held in place by glass wool. An inert glass tube is placed in the stainless-steel tube, downstream from the catalyst, in order to reduce the empty volume of the reactor and to prevent the catalyst bed from being pushed out of the heated zone by the reactant flow. The liquid feed, either a mixture of 1.0 g HMF (99%, Sigma-Aldrich) or 0.76 g DMF (99%, Sigma-Aldrich) in 100 mL of 1-propanol (Fisher Scientific), is introduced into the reactor by an HPLC pump (Series I+, Scientific Systems Inc.), which is also used to measure the total pressure in the reactor. (The reaction of DMF is performed with 0.76 g of DMF in 100 ml of 1-propanol to maintain the same molar concentration as that used in the HMF rate measurements.) The H_2 (UHP grade, Airgas) flow to the reactor is controlled by varying the pressure drop across 8 feet of 0.002-inch ID capillary tubing (Valco Instruments, Inc.). A bubble meter at the reactor exit is used periodically to check that the H_2 flow rates. The liquid flow rates could be varied from 0.02 to 0.2 ml/min, while the H_2 flow rates are 2 to 20 mL/min (STP). In order to vary the space velocity in the reactor at fixed experimental conditions, the ratio of liquid and gas flow rates is kept constant. The pressure within the reactor is controlled by a back-pressure regulator (KPB series, Swagelok) placed at the reactor exit.

Prior to rate measurements, the catalyst is pretreated at 250ºC in 1 bar of flowing H_2 for 30 min. Because the products left the reactor at room temperature, product analysis is carried out using a syringe to inject the liquid effluent into a GC-MS (QP-5000, Shimadzu), equipped with a capillary column (HP-Innowax, Agilent Technologies). The gas-phase products are also examined but, under the conditions of these experiments, are found to consist of only H_2 and solvent vapor. Product selectivities are quantified using standard solutions with known concentrations of HMF, DMF, dimethyl-tetrahydrofuran (DMTHF), 2-hexanone, 2-hexanol, and 2,5-hexandione (all purchased from Sigma Aldrich). For quantification of other furan-based, intermediate products, the GC sensitivity is assumed to be the same as that for HMF. For open-ring, ether products, the GC sensitivity is assumed to be the same as 2-hexanone or 2,5-hexandione. The carbon balance from GC analysis is always better than 95%.

The typical time for an experiment is 4 h. For each sample injection, the GC analysis requires 30 min. Most of the data reported here are chosen from the second or third measurement (40 to 60 min after starting the reaction). Under the conditions of this study, no reaction is observed in the absence of a catalyst in the flow reactor.

CHAPTER 6. References

(1) Sun, S.; Murray, C. B.; Weller, D.; Folks, L.; Moser, A. **2000**, *287*, 1989.

(2) Shevchenko, E. V; Talapin, D. V; Rogach, A. L.; Kornowski, A.; Haase, M.; Weller, H. *J. Am. Chem. Soc.* **2002**, *124*, 11480.

(3) Park, J.; An, K.; Hwang, Y.; Park, J.-G.; Noh, H.-J.; Kim, J.-Y.; Park, J.-H.; Hwang, N.-M.; Hyeon, T. *Nat. Mater.* **2004**, *3*, 891.

(4) Tang, L.; Han, B.; Persson, K.; Friesen, C.; He, T.; Sieradzki, K.; Ceder, G. *J. Am. Chem. Soc.* **2010**, *132*, 596.

(5) Yu, Y.; Yang, W.; Sun, X.; Zhu, W.; Sellmyer, D. J.; Sun, S. *Nano Lett.* **2014**, *14*, 2778.

(6) Luo, J.; Arroyo-ram, L.; Gorte, R. J. *Am. Inst. Chem. Eng. J.* **2014**, *00*, 1.

(7) Wang, G.-H.; Hilgert, J.; Richter, F. H.; Wang, F.; Bongard, H.; Spliethoff, B.; Weidenthaler, C.; Schüth, F. *Nat. Mater.* **2014**, *13*, 293.

(8) Puthussery, J.; Seefeld, S.; Berry, N.; Gibbs, M.; Law, M. *J. Am. Chem. Soc.* **2011**, *133*, 716.

(9) Peng, B.; Li, Z.; Mutlugun, E.; Hernández Martínez, P. L.; Li, D.; Zhang, Q.; Gao, Y.; Demir, H. V.; Xiong, Q. *Nanoscale* **2014**, *6*, 5592.

(10) Kuskovsky, I. L.; Andelman, T.; Zhu, Y.; Neumark, G. F.; Brien, S. O. *J. Am. Chem. Soc.* **2004**, *126*, 6206.

(11) Lee, J.-H.; Jang, J.-T.; Choi, J.-S.; Moon, S. H.; Noh, S.-H.; Kim, J.-W.; Kim, J.-G.; Kim, I.-S.; Park, K. I.; Cheon, J. *Nat. Nanotechnol.* **2011**, *6*, 418.

(12) Tromsdorf, U. I.; Bigall, N. C.; Kaul, M. G.; Bruns, O. T.; Nikolic, M. S.; Mollwitz, B.; Sperling, R. a; Reimer, R.; Hohenberg, H.; Parak, W. J.; Förster, S.; Beisiegel, U.; Adam, G.; Weller, H. *Nano Lett.* **2007**, *7*, 2422.

(13) Park, M.; Lee, N.; Choi, S. H.; An, K.; Yu, S.; Kim, J. H.; Kwon, S.; Kim, D.; Kim, H.; Baek, S.; Ahn, T.; Park, O. K.; Son, J. S.; Sung, Y.; Kim, Y.; Wang, Z.; Pinna, N.; Hyeon, T. *Chem. Mater.* **2011**, *23*, 3318.

(14) Lee, N.; Choi, Y.; Lee, Y.; Park, M.; Moon, W. K.; Choi, S. H.; Hyeon, T. *Nano Lett.* **2012**, *12*, 3127.

(15) Bean, C. P.; Livingston, J. D. *J. Appl. Phys.* **1959**, *30*, S120.

(16) Majetich, S. a.; Wen, T.; Mefford, O. T. *MRS Bull.* **2013**, *38*, 899.

(17) Sugimoto, T.; Zhou, X.; Muramatsu, A. *J. Colloid Interface Sci.* **2003**, *259*, 43.

(18) Song, W.; Poyraz, A. S.; Meng, Y.; Ren, Z.; Chen, S. Y.; Suib, S. L. *Chem. Mater.* **2014**, *26*, 4629.

(19) An, K.; Park, M.; Yu, J. H.; Na, H. Bin; Lee, N.; Park, J.; Choi, S. H.; Song, I. C.; Moon, W. K.; Hyeon, T. *Eur. J. Inorg. Chem.* **2012**, *2012*, 2148.

(20) Song, Q.; Ding, Y.; Wang, Z. L.; Zhang, Z. J. *Chem. Mater.* **2007**, *19*, 4633.

(21) Kwon, S. G.; Piao, Y.; Park, J.; Angappane, S.; Jo, Y.; Hwang, N.-M.; Park, J.-G.; Hyeon, T. *J. Am. Chem. Soc.* **2007**, *129*, 12571.

(22) Sun, S.; Zeng, H.; Robinson, D. B.; Raoux, S.; Rice, P. M.; Wang, S. X.; Li, G. *J. Am. Chem. Soc.* **2004**, *4*, 126.

(23) Shan, S.; Petkov, V.; Yang, L.; Luo, J.; Joseph, P.; Mayzel, D.; Prasai, B.; Wang, L.; Engelhard, M.; Zhong, C. *J. Am. Chem. Soc.* **2014**, *136*, 7140.

(24) Johnston-peck, A. C.; Wang, J.; Tracy, J. B. *ACS Nano* **2009**, *3*, 1077.

(25) Haase, M.; Schäfer, H. *Angew. Chemie - Int. Ed.* **2011**, *50*, 5808.

(26) Yun, H.; Liu, X.; Paik, T.; Palanisamy, D.; Kim, J.; Vogel, W. D.; Viescas, A. J.; Chen, J.; Papaefthymiou, G. C.; Kikkawa, J. M.; Allen, M. G.; Murray, C. B. *ACS Nano* **2014**, *8*, 12323.

(27) Degueldre, C.; Kuri, G.; Borca, C. N.; Grolimund, D. *Corros. Sci.* **2009**, *51*, 1690.

(28) Snelling, E. C.; Giles, A. D. *Ferrites for Inductors and Transformers*; Research Studies Press/Wiley: Letchworth Herts./New York, 1983.

(29) Cargnello, M.; Doan-Nguyen, V. V. T.; Gordon, T. R.; Diaz, R. E.; Stach, E. a; Gorte, R. J.; Fornasiero, P.; Murray, C. B. *Science* **2013**, *341*, 771.

(30) Noh, S.-H.; Na, W.; Jang, J.-T.; Lee, J.-H.; Lee, E. J.; Moon, S. H.; Lim, Y.; Shin, J.-S.; Cheon, J. *Nano Lett.* **2012**, *12*, 3716.

(31) Murray, C. B.; Norris, D. J.; Bawendi, M. G. *J. Am. Chem. Soc.* **1993**, *115*, 8706.

(32) Murray, C. B.; Kagan, C. R.; Bawendi, M. G. *Annu. Rev. Mater. Sci.* **2000**, *30*, 545.

(33) Choi, S.; Xie, S.; Shao, M.; Odell, J. H.; Lu, N.; Peng, H. C.; Protsailo, L.; Guerrero, S.; Park, J.; Xia, X.; Wang, J.; Kim, M. J.; Xia, Y. *Nano Lett.* **2013**, *13*, 3420.

(34) Liu, Q.; Yan, Z.; Henderson, N. L.; Bauer, J. C.; Goodman, D. W.; Batteas, J. D.; Schaak, R. E. *J. Am. Chem. Soc.* **2009**, *131*, 5720.

(35) Zhang, S.; Hao, Y.; Su, D.; Doan-nguyen, V. V. T.; Wu, Y.; Li, J.; Sun, S.; Murray, C. B. *J. Am. Chem. Soc.* **2014**, *136*, 15921.

(36) Borgna, A.; Borgna, A.; Anderson, B. G.; Anderson, B. G.; Saib, A. M.; Saib, A. M.; Bluhm, H.; Bluhm, H.; Ha, M.; Ha, M.; Knop-gericke, A.; Knop-gericke, A.; Tamminga, Y.; Tamminga, Y. *J. Phys. Chem. B* **2004**, *108*, 17905.

(37) Murray, C. B.; Sun, S.; Doyle, H.; Betley, T. *MRS Bull.* **2001**, *26*, 985.

(38) Gordon, T. R.; Cargnello, M.; Paik, T.; Mangolini, F.; Weber, R. T.; Fornasiero, P.; Murray, C. B. *J. Am. Chem. Soc.* **2012**, *134*, 6751.

(39) Roca, A. G.; Marco, J. F.; Morales, P.; Serna, C. J. *J. Phys. Chem. C* **2007**, *111*, 18577.

(40) Dong, A.; Chen, J.; Ye, X.; Kikkawa, J. M.; Murray, C. B. *J. Am. Chem. Soc.* **2011**, *133*, 13296.

(41) Spaldin, N. A. *Magnetic Materials: Fundamentals and Applications*; 2nd ed.; Cambridge University Press, 2011.

(42) Brown. *Phys. Rev.* **1963**, *130*, 1677.

(43) Hergt, R.; Andr, W.; Ambly, C. G.; Hilger, I.; Kaiser, W. A.; Richter, U.; Schmidt, H. *IEEE Trans. Magn.* **1998**, *34*, 3745.

(44) Guardia, P.; Corato, R. Di; Lartigue, L.; Wilhelm, C.; Espinosa, A.; Garcia-hernandez, M.; Gazeau, F.; Manna, L.; Pellegrino, T. *ACS Nano* **2012**, *6*, 3080.

(45) Riedinger, A.; Guardia, P.; Curcio, A.; Garcia, M. A.; Cingolani, R.; Manna, L.; Pellegrino, T. *Nano Lett.* **2013**, *13*, 2399.

(46) Rosensweig, R. E. *J. Magn. Magn. Mater.* **2002**, *252*, 370.

(47) Chu, K. F.; Dupuy, D. E. *Nat. Rev. Cancer* **2014**, *14*, 199.

(48) Jordan, A.; Scholz, R.; Wust, P.; Fähling, H.; Roland Felix. *J. Magn. Magn. Mater.* **1999**, *201*, 413.

(49) Yao, D.; Levey, C. G.; Tian, R.; Sullivan, C. R. *IEEE Trans. Power Electron.* **2013**, *28*, 4384.

(50) Dashtban, M.; Gilbert, A.; Fatehi, P. *RSC Adv.* **2014**, *4*, 2037.

(51) Wang, T.; Nolte, M. W.; Shanks, B. H. *Green Chem.* **2014**, *16*, 548.

(52) Torres, A. I.; Daoutidis, P.; Tsapatsis, M. *Energy Environ. Sci.* **2010**, *3*, 1560.

(53) Román-Leshkov, Y.; Barrett, C. J.; Liu, Z. Y.; Dumesic, J. a. *Nature* **2007**, *447*, 982.

(54) Chidambaram, M.; Bell, A. T. *Green Chem.* **2010**, *12*, 1253.

(55) Thananatthanachon, T.; Rauchfuss, T. B. *Angew. Chemie - Int. Ed.* **2010**, *49*, 6616.

(56) Jae, J.; Zheng, W.; Karim, A. M.; Guo, W.; Lobo, R. F.; Vlachos, D. G. *ChemCatChem* **2014**, *6*, 848.

(57) Nishimura, S.; Ikeda, N.; Ebitani, K. *Catal. Today* **2014**, *232*, 89.

(58) Kang, Y.; Ye, X.; Chen, J.; Qi, L.; Diaz, R. E.; Doan-nguyen, V.; Xing, G.; Kagan, C. R.; Li, J.; Gorte, R. J.; Stach, E. A.; Murray, C. B. *J. Am. Chem. Soc.* **2013**, *135*, 1499.

(59) Chua, Y. P. G.; Gunasooriya, G. T. K. K.; Saeys, M.; Seebauer, E. G. *J. Catal.* **2014**, *311*, 306.

(60) Cargnello, M.; Jaen, J. J. D.; Garrido, J. C. H.; Bakhmutsky, K.; Montini, T.; Gamez, J. J. C.; Gorte, R. J.; Fornasiero, P. *Science (80-.).* **2012**, *337*, 713.

(61) Cao, A.; Veser, G. *Nat. Mater.* **2010**, *9*, 75.

(62) Gonc, R. H.; Lima, B. H. R.; Leite, E. R. *J. Am. Chem. Soc.* **2011**, *133*, 6012.

(63) Kang, Y.; Murray, C. B. *J. Am. Chem. Soc.* **2010**, *132*, 7568.

(64) Desvaux, C.; Amiens, C.; Fejes, P.; Renaud, P.; Respaud, M.; Lecante, P.; Snoeck, E.; Chaudret, B. *Nat. Mater.* **2005**, *4*, 750.

(65) Desvaux, C.; Dumestre, F.; Amiens, C.; Respaud, M.; Lecante, P.; Snoeck, E.; Fejes, P.; Renaud, P.; Chaudret, B. *J. Mater. Chem.* **2009**, *19*, 3268.

(66) Sun, S.; Murray, C. B.; Weller, D.; Folks, L.; Moser, A. *Science (80-.).* **2000**, *287*, 1989.

(67) Brosseau, C.; Talbot, P. *J. Appl. Phys.* **2005**, *97*, 104325.

(68) Song, N.-N.; Yang, H.-T.; Liu, H.-L.; Ren, X.; Ding, H.-F.; Zhang, X.-Q.; Cheng, Z.-H. *Sci. Rep.* **2013**, *3*, 3161.

(69) Kura, H.; Ogawa, T.; Tate, R.; Hata, K.; Takahashi, M. *J. Appl. Phys.* **2012**, *111*, 07B517.

(70) Paik, T.; Gordon, T. R.; Prantner, A. M.; Yun, H.; Murray, C. B. *ACS Nano* **2013**, *7*, 2850.

(71) Issadore, D.; Chung, J.; Shao, H.; Liong, M.; Ghazani, A. a; Castro, C. M.; Weissleder, R.; Lee, H. *Sci. Transl. Med.* **2012**, *4*, 141ra92.

(72) Fortin, J. P.; Wilhelm, C.; Servais, J.; Ménager, C.; Bacri, J. C.; Gazeau, F. *J. Am. Chem. Soc.* **2007**, *129*, 2628.

(73) Ruan, S.; Xu, B.; Suo, H.; Wu, F.; Xiang, S.; Zhao, M. *J. Magn. Magn. Mater.* **2000**, *212*, 175.

(74) Li, Y.; Zhang, J.; Liu, Z.; Liu, M.; Lin, H.; Che, R. *J. Mater. Chem. C* **2014**, *2*, 5216.

(75) Pan, G.; Zhu, J.; Ma, S.; Sun, G.; Yang, X. *ACS Appl. Mater. Interfaces* **2013**, *5*, 12716.

(76) Qiu, J.; Member, S.; Sullivan, C. R.; Member, S. *IEEE Trans. Power Electron.* **2012**, *27*, 4965.

(77) Kim, J.; Ni, W.; Lee, C.; Kan, E. C.; Hosein, I. D.; Song, Y.; Liddell, C. *J. Appl. Phys.* **2006**, *99*, 08R903.

(78) Huang, W.; Yu, X.; Froeter, P.; Xu, R.; Ferreira, P.; Li, X. *Nano Lett.* **2012**, *12*, 6283.

(79) Choi, C.; Yoo, H. S.; Oh, J. M. *Curr. Appl. Phys.* **2008**, *8*, 710.

(80) Guan, W.; Jin, M.; Fan, Y.; Chen, J.; Xin, P.; Li, Y.; Dai, K.; Zhang, H.; Huang, T.; Ruan, J. *IEEE Trans. Magn.* **2014**, *50*, 253.

(81) Miao, J.; Dong, M.; Ren, M.; Wu, X.; Shen, L.; Wang, H. *J. Appl. Phys.* **2013**, *113*, 204103.

(82) Bosch-Jimenez, P.; Yu, Y.; Lira-Cantu, M.; Domingo, C.; Ayllón, J. a. *J. Colloid Interface Sci.* **2014**, *416*, 112.

(83) Cozzoli, P. D.; Kornowski, A.; Weller, H. *J. Am.* **2003**, *125*, 14539.

(84) Panthani, M. G.; Akhavan, V.; Goodfellow, B.; Schmidtke, J. P.; Dunn, L.; Dodabalapur, A.; Barbara, P. F.; Korgel, B. A. *J. Am. Chem. Soc.* **2008**, *130*, 16770.

(85) Sun, Q.; Wang, Y. A.; Li, L. S.; Wang, D.; Zhu, T.; Xu, J.; Yang, C.; Li, Y. *Nat. Photonics* **2007**, *1*, 717.

(86) Sun, S.; Murray, C. B. *J. Appl. Phys.* **1999**, *85*, 4325.

(87) Araghchini, M.; Chen, J.; Doan-nguyen, V.; Harburg, D. V; Jin, D.; Kim, J.; Kim, M. S.; Lim, S.; Lu, B.; Piedra, D.; Qiu, J.; Ranson, J.; Sun, M.; Yu, X.; Yun, H.; Allen, M. G.; Alamo, A.; Desgroseilliers, G.; Herrault, F.; Lang, J. H.; Levey, C. G.; Murray, C. B.; Otten, D.; Perreault, D. J.; Sullivan, C. R. *IEEE Trans. Power Electron.* **2013**, *28*, 4182.

(88) Park, J. Y.; Allen, M. G. *IEEE Trans. Adv. Packag.* **1999**, *22*, 207.

(89) Korenivski, V. *J. Magn. Magn. Mater.* **2000**, *216*, 800.

(90) Zhang, X.; Ekiert, T.; Unruh, K. M.; Xiao, J. Q.; Golt, M.; Wu, R. *J. Appl. Phys.* **2006**, *99*, 08M914.

(91) Sullivan, C. R.; Harburg, D. V; Qiu, J.; Levey, C. G.; Yao, D. *IEEE Trans. Power Electron.* **2013**, *28*, 4342.

(92) Jiles, D. C.; Atherton, D. L. *J. Appl. Phys.* **1984**, *55*, 2115.

(93) Cullity, B. D. *Introduction to Magnetic Materials*; 2nd ed.; Hoboken, N.J. : Wiley ; Piscataway, NJ : IEEE Press, 2009.

(94) Dutz, S.; Hergt, R.; Mürbe, J.; Müller, R.; Zeisberger, M.; Andrä, W.; Töpfer, J.; Bellemann, M. E. *J. Magn. Magn. Mater.* **2007**, *308*, 305.

(95) Sun, S.; Murray, C. B. *J. Appl. Phys.* **1999**, *85*, 4325.

(96) Park, J.; Kang, E.; Son, S. U.; Park, H. M.; Lee, M. K.; Kim, J.; Kim, K. W.; Noh, H.-J.; Park, J.-H.; Bae, C. J.; Park, J.-G.; Hyeon, T. *Adv. Mater.* **2005**, *17*, 429.

(97) Kang, S.; Miao, G. X.; Shi, S.; Jia, Z.; Nikles, D. E.; Harrell, J. W. **2006**, 1042.

(98) Gilbert, B.; Katz, J. E.; Denlinger, J. D.; Yin, Y.; Falcone, R.; Waychunas, G. A. *J. Phys. Chem. C* **2010**, *114*, 21994.

(99) Rebodos, R. L.; Vikesland, P. J. *Langmuir* **2010**, *26*, 16745.

(100) Chen, J.; Ye, X.; Oh, S. J.; Kikkawa, J. M.; Kagan, C. R.; Murray, C. B. *ACS Nano* **2013**, 1478.

(101) Gordon, T. R.; Diroll, B. T.; Paik, T.; Doan-Nguyen, V. V. T.; Gaulding, E. A.; Murray, C. B. *Chem. Mater.* **2015**, 150319105434007.

(102) Papaefthymiou, G. C. *MRS Proc.* **1994**, *332*, 261.

(103) Greenwood, N. N.; Gibb, T. C. *Mossbauer Spectroscopy*; Chapman and Hall: London, 1971.

(104) Mørup, S.; Topsøe, H. *Appl. Phys.* **1976**, *11*, 63.

(105) Papaefthymiou, G.; Devlin, E.; Simopoulos, A.; Yi, D.; Riduan, S.; Lee, S.; Ying, J. *Phys. Rev. B* **2009**, *80*, 024406.

(106) Verwey, E. J. W. *Nature* **1939**.

(107) Doriguetto, A. C.; Fernandes, N. G.; Persiano, A. I. C.; Nunes Filho, E.; Greneche, J.-M.; Fabris, J. D. *Phys. Chem. Miner.* **2003**, *30*, 249.

(108) Dézsi, I.; Szűcs, I.; Fetzer, C. *J. Appl. Phys.* **2008**, *104*, 034904.

(109) Redl, F. X.; Black, C. T.; Papaefthymiou, G. C.; Sandstrom, R. L.; Yin, M.; Zeng, H.; Murray, C. B.; Brien, S. P. O. *J. Am. Chem. Soc.* **2004**, *126*, 14583.

(110) Lak, A.; Kraken, M.; Ludwig, F.; Kornowski, A.; Eberbeck, D.; Sievers, S.; Litterst, F. J.; Weller, H.; Schilling, M. *Nanoscale* **2013**, *5*, 12286.

(111) Gorski, C. a.; Scherer, M. M. *Am. Mineral.* **2010**, *95*, 1017.

(112) Nunes, W.; Folly, W.; Sinnecker, J.; Novak, M. *Phys. Rev. B* **2004**, *70*, 014419.

(113) Makhlouf, S. A.; Parker, F. T.; Berkowitz, A. E. *Phys. Rev. B* **1997**, *55*, 717.

(114) Knobel, M.; Nunes, W. C.; Winnischofer, H.; Rocha, T. C. R.; Socolovsky, L. M.; Mayorga, C. L.; Zanchet, D. *J. Non. Cryst. Solids* **2007**, *353*, 743.

(115) Mørup, S.; Hansen, M. F.; Frandsen, C. *Beilstein J. Nanotechnol.* **2010**, *1*, 182.

(116) Huang, D. J.; Chang, C. F.; Jeng, H.-T.; Guo, G. Y.; Lin, H.-J.; Wu, W. B.; Ku, H. C.; Fujimori, a.; Takahashi, Y.; Chen, C. T. *Phys. Rev. Lett.* **2004**, *93*, 077204.

(117) O'Handley, R. C. *Modern Magnetic Materials, Principles and Applications*; John Wiley & Son, Inc., 2000.

(118) Papaefthymiou, G. C. *Nano Today* **2009**, *4*, 438.

(119) Bødker, F.; Mørup, S.; Lideroth, S. *Phys. Rev. Lett.* **1994**, *72*, 8.

(120) Walz, F. *J. Phys. Condens. Matter* **2002**, *14*, R285.

(121) Yang, J. B.; Zhou, X. D.; Yelon, W. B.; James, W. J.; Cai, Q.; Gopalakrishnan, K. V.; Malik, S. K.; Sun, X. C.; Nikles, D. E. *J. Appl. Phys.* **2004**, *95*, 7540.

(122) Daou, T. J.; Pourroy, G.; Begin-Colin, S.; Greneche, J.-M.; Ulhaq-Bouillet, C.; Legare, P.; Bernhardt, P.; Leuvrey, C.; Rogez, G. *Chem. Mater.* **2006**, *18*, 4399.

(123) Nikiforov, V. N.; Koksharov, Y. A.; Polyakov, S. N.; Malakho, a. P.; Volkov, a. V.; Moskvina, M. a.; Khomutov, G. B.; Irkhin, V. Y. *J. Alloys Compd.* **2013**, *569*, 58.

(124) Aragon, R. *Phys. Rev. B* **1992**, *46*, 5334.

(125) Goya, G. F.; Berquó, T. S.; Fonseca, F. C.; Morales, M. P. *J. Appl. Phys.* **2003**, *94*, 3520.

(126) Lucchini, M. a.; Riani, P.; Canepa, F. *J. Nanoparticle Res.* **2013**, *15*, 1601.

(127) Shenhui, J.; Member, S.; Quanxing, J. *IEEE Trans. Electromagn. Compat.* **2005**, *47*, 651.

(128) Tronc, E.; Ezzir, A.; Cherkaoui, R.; Chane, C.; Kachkachi, H.; Fiorani, D.; Testa, A. M.; Grene, J. M.; Jolivet, J. P. *J. Magn. Magn. Mater.* **2000**, *221*, 63.

(129) Iida, H.; Takayanagi, K.; Nakanishi, T.; Osaka, T. *J. Colloid Interface Sci.* **2007**, *314*, 274.

(130) Huang, C.-C.; Chuang, K.-Y.; Chou, C.-P.; Wu, M.-T.; Sheu, H.-S.; Shieh, D.-B.; Tsai, C.-Y.; Su, C.-H.; Lei, H.-Y.; Yeh, C.-S. *J. Mater. Chem.* **2011**, *21*, 7472.

(131) Demortière, A.; Panissod, P.; Pichon, B. P.; Pourroy, G.; Guillon, D.; Donnio, B.; Bégin-Colin, S. *Nanoscale* **2011**, *3*, 225.

(132) Diehl, M. R.; Yu, J. Y.; Heath, J. R.; Held, G. a.; Doyle, H.; Sun, S.; Murray, C. B. *J. Phys. Chem. B* **2001**, *105*, 7913.

(133) Sato, T.; Iijima, T.; Seki, M.; Inagaki, N. *J. Magn. Magn. Mater.* **1987**, *65*, 252.

(134) Burnham, P.; Dollahon, N.; Li, C. H.; Viescas, a. J.; Papaefthymiou, G. C. *J. Nanoparticles* **2013**, *2013*, 1.

(135) Sun, S.; Zeng, H. *J. Am. Chem. Soc.* **2002**, *124*, 8204.

(136) Riahi-kashani, M. M.; Elshabini-riad, A. *IEEE Trans. Instrum. Meas.* **1992**, *41*, 1036.

(137) Markondeya Raj, P.; Sharma, H.; Samtani, S.; Mishra, D.; Nair, V.; Tummala, R. *J. Mater. Sci. Mater. Electron.* **2013**, *24*, 3448.

(138) Raj, P. M.; Sharma, H.; Reddy, G. P.; Reid, D.; Altunyurt, N. *Electron. Components Technol. Conf.* **2011**, 1244.

(139) Bedair, S. S.; Meyer, C. D.; Morgan, B. *J. Appl. Phys.* **2011**, *109*, 07E702.

(140) Dong, A.; Ye, X.; Chen, J.; Kang, Y.; Gordon, T.; Kikkawa, J. M.; Murray, C. B. *J. Am. Chem. Soc.* **2011**, *133*, 998.

(141) Pardavi-Horvath, M. *J. Magn. Magn. Mater.* **2000**, *215*, 171.

(142) Adam, J. D.; Davis, L. E.; Dionne, G. F.; Schloemann, E. F.; Stitzer, S. N. *IEEE Trans. Microw. Theory Tech.* **2002**, *50*, 721.

(143) Yoo, D.; Lee, J. H.; Shin, T. H.; Cheon, J. *Acc. Chem. Res.* **2011**, *44*, 863.

(144) Kumar, C. S. S. R.; Mohammad, F. *Adv. Drug Deliv. Rev.* **2011**, *63*, 789.

(145) Deatsch, A. E.; Evans, B. a. *J. Magn. Magn. Mater.* **2014**, *354*, 163.

(146) Yu, Y.; Mendoza-Garcia, A.; Ning, B.; Sun, S. *Adv. Mater.* **2013**, *25*, 3090.

(147) Nlebedim, I. C.; Snyder, J. E.; Moses, a. J.; Jiles, D. C. *IEEE Trans. Magn.* **2012**, *48*, 3084.

(148) Calero-DdelC, V. L.; Rinaldi, C. *J. Magn. Magn. Mater.* **2007**, *314*, 60.

(149) Doaga, a.; Cojocariu, a. M.; Amin, W.; Heib, F.; Bender, P.; Hempelmann, R.; Caltun, O. F. *Mater. Chem. Phys.* **2013**, *143*, 305.

(150) Tachiki, M. *Prog. Theor. Phys.* **1960**, *23*, 1055.

(151) Bao, N.; Shen, L.; Padhan, P.; Gupta, A. *Appl. Phys. Lett.* **2008**, *92*, 2.

(152) Song, Q.; Zhang, Z. J. *J. Am. Chem. Soc.* **2004**, *126*, 6164.

(153) Vázquez-Vázquez, C.; López-Quintela, M. a.; Buján-Núñez, M. C.; Rivas, J. *J. Nanoparticle Res.* **2011**, *13*, 1663.

(154) Rajendran, M.; Pullar, R. C.; Bhattacharya, A. K.; Das, D.; Chintalapudi, S. N.; Majumdar, C. K. *J. Magn. Magn. Mater.* **2001**, *232*, 71.

(155) Peddis, D.; Orru, F.; Ardu, A.; Cannas, C.; Musinu, A.; Piccaluga, G. *Chem. Mater.* **2012**, *24*, 1062.

(156) Kagan, C. R.; Mitzi, D. B.; Dimitrakopoulos, C. D. *Science (80-.).* **1999**, *286*, 945.

(157) Lee, C. Y.; Lin, M. Y.; Wu, W. H.; Wang, J. Y.; Chou, Y.; Su, W. F.; Chen, Y. F.; Lin, C. F. *Semicond. Sci. Technol.* **2010**, *25*, 105008.

(158) Li, L.; Coates, N.; Moses, D. *J. Am. Chem. Soc.* **2010**, *132*, 22.

(159) Yang, Y.; Liu, X.; Yang, Y.; Xiao, W.; Li, Z.; Xue, D.; Li, F.; Ding, J. *J. Mater. Chem. C* **2013**, *1*, 2875.

(160) Yao, C.; Zeng, Q.; Goya, G. F.; Torres, T.; Liu, J.; Wu, H.; Ge, M.; Zeng, Y.; Wang, Y.; Jiang, J. Z. *J. Phys. Chem. C* **2007**, *111*, 12274.

(161) Birajdar, a. a.; Shirsath, S. E.; Kadam, R. H.; Mane, M. L.; Mane, D. R.; Shitre, a. R. *J. Appl. Phys.* **2012**, *112*, 053908.

(162) Sun, X.; Peng, X.; Zheng, Y.; Li, X.; Zhang, H. A.; Member, S. *IEEE J. MICROELECTROMECHANICAL Syst.* **2014**, *23*, 888.

(163) Chen, P. J.; Saati, S.; Varma, R.; Humayun, M. S.; Tai, Y. C. *J. Microelectromechanical Syst.* **2010**, *19*, 721.

(164) Waffenschmidt, E.; Ackermann, B.; Wille, M. *IEEE 36th Conf. Power Electron. Spec. 2005.* **2005**, 1528.

(165) Dong, H.; Liu, F.; Wong, C. P.; Song, Q.; Zhang, Z. J. *9th Int. Symp. Adv. Packag. Mater.* **2004**, 171.

(166) Ho, S. L.; Wang, J.; Fu, W. N.; Sun, M. *IEEE Trans. Magn.* **2011**, *47*, 1522.

(167) Cheong, J. H.; Chan, K. L.; Khannur, B.; Tiew, K. T.; Je, M. *IEEE Trans. Circuits Syst.* **2011**, *58*, 407.

(168) Zhong, W. X.; Liu, X.; Hui, S. Y. R. *IEEE Trans. Ind. Electron.* **2011**, *58*, 4136.

(169) Horton, B. E.; Schweitzer, S.; DeRouin, A. J.; Ong, K. G. *IEEE Sens. J.* **2011**, *11*, 1061.

(170) Kim, J.; Kim, J.-K.; Kim, M.; Herrault, F.; Allen, M. G. *J. Micromechanics Microengineering* **2013**, *23*, 114006.

(171) Arshak, K. I.; Ajina, a.; Egan, D. *Microelectronics J.* **2001**, *32*, 113.

(172) Hochepied, J. F.; Bonville, P.; Pileni, M. P. *J. Phys. Chem. B* **2000**, *104*, 905.

(173) Mathew, D. S.; Juang, R. S. *Chem. Eng. J.* **2007**, *129*, 51.

(174) Caizer, C.; Stefanescu, M. *J. Phys. D. Appl. Phys.* **2002**, *35*, 3035.

(175) Snoek, J. L. Gyromagnetic resonance in ferrites. *Nature*, 1947, *159*, 90.

(176) Chand, J.; Kumar, G.; Kumar, P.; Sharma, S. K.; Knobel, M.; Singh, M. *J. Alloys Compd.* **2011**, *509*, 9638.

(177) Yang, H. T.; Hasegawa, D.; Takahashi, M.; Ogawa, T. *Appl. Phys. Lett.* **2009**, *94*, 2.

(178) Hassinen, A.; Moreels, I.; De Nolf, K.; Smet, P. F.; Martins, J. C.; Hens, Z. *J. Am. Chem. Soc.* **2012**, *134*, 20705.

(179) Weidman, M. C.; Beck, M. E.; Hoffman, R. S.; Prins, F.; Tisdale, W. A. *ACS Nano* **2014**, 6363.

(180) Cademartiri, L.; Bertolotti, J.; Sapienza, R.; Wiersma, D. S.; von Freymann, G.; Ozin, G. a. *J. Phys. Chem. B* **2006**, *110*, 671.

(181) Rayleigh, L. *Proc. R. Soc. A Math. Phys. Eng. Sci.* **1914**, *90*, 219.

(182) Li, X.; Chen, G.; Po-Lock, Y.; Kutal, C. *J. Mater. Sci. Lett.* **2002**, *21*, 1881.

(183) Lee, J.-H.; Huh, Y.-M.; Jun, Y.; Seo, J.; Jang, J.; Song, H.-T.; Kim, S.; Cho, E.-J.; Yoon, H.-G.; Suh, J.-S.; Cheon, J. *Nat. Med.* **2007**, *13*, 95.

(184) Gorter, E. W. *Nature* **1950**, *165*, 798.

(185) Zuo, X.; Yang, A.; Yoon, S.-D.; Christodoulides, J. a.; Harris, V. G.; Vittoria, C. *J. Appl. Phys.* **2005**, *97*, 10G103.

(186) Jishkariani, D.; Diroll, B. T.; Cargnello, M.; Klein, D. R.; Hough, L. a.; Murray, C. B.; Donnio, B. *J. Am. Chem. Soc.* **2015**, *137*, 10728.

(187) Kang, K.; Li, L.; Zouhdi, S.; Shi, J.; Yin, W. *Proc. 1st Eur. Microw. Integr. Circuits Conf.* **2006**, *7*, 13.

(188) Nikbin, N.; Do, P. T.; Caratzoulas, S.; Lobo, R. F.; Dauenhauer, P. J.; Vlachos, D. G. *J. Catal.* **2013**, *297*, 35.

(189) Xiong, R.; Sandler, S. I.; Vlachos, D. G.; Dauenhauer, P. J. *Green Chem.* **2014**, *16*, 4086.

(190) Mironenko, A. V.; Gilkey, M. J.; Panagiotopoulou, P.; Facas, G.; Vlachos, D. G.; Xu, B. *J. Phys. Chem. C* **2015**, *119*, 6075.

(191) Kwon, S. G.; Krylova, G.; Sumer, A.; Schwartz, M. M.; Bunel, E. E.; Marshall, C. L.; Chattopadhyay, S.; Lee, B.; Jellinek, J.; Shevchenko, E. V. *Nano Lett.* **2012**, *12*, 5382.

(192) He, B.; Meng, X.; Tang, Q. *ACS Appl. Mater. Interfaces* **2014**, *6*, 4812.

(193) Park, J. I.; Kim, M. G.; Jun, Y. W.; Lee, J. S.; Lee, W. R.; Cheon, J. *J. Am. Chem. Soc.* **2004**, *126*, 9072.

(194) Vasquez, Y.; Sra, A. K.; Schaak, R. E. *J. Am. Chem. Soc.* **2010**, *127*, 12504.

(195) Fievet, F.; Lagier, J.; Blin, B.; Beaudoin, B.; Figlarz, M. *Solid State Ionics* **1989**, *32-33*, 198.

(196) Yu, Y.; Yang, W.; Sun, X.; Zhu, W.; Li, X. Z.; Sellmyer, D. J.; Sun, S. *Nano Lett.* **2014**, *14*, 2778.

(197) Wang, D.; Xin, H. L.; Hovden, R.; Wang, H.; Yu, Y.; Muller, D. a.; DiSalvo, F. J.; Abruña, H. D. *Nat. Mater.* **2012**, *12*, 81.

(198) Cargnello, M.; Chen, C.; Diroll, B. T.; Doan-Nguyen, V. V. T.; Gorte, R. J.; Murray, C. B. *J. Am. Chem. Soc.* **2015**, 150511134938005.